

MECHANICS OF THE URINARY BLADDER IN HEALTH AND DISEASE

By

Tyler Glenn Tuttle

A DISSERTATION

Submitted to
Michigan State University
in partial fulfillment of the requirements
for the degree of

Mechanical Engineering – Doctor of Philosophy

2021

ABSTRACT

MECHANICS OF THE URINARY BLADDER IN HEALTH AND DISEASE

By

Tyler Glenn Tuttle

The urinary bladder stores and voids urine through relaxation and contraction. The ability of the bladder to drastically increase in size while maintaining minimal pressure is key to proper organ function, making the study of bladder tissue mechanical characteristics crucial. Several diseases and disabilities that lead to bladder dysfunction are accompanied by pathological remodeling of the bladder wall that can dramatically impact its mechanical behavior. Before we can understand pathological changes, we must understand the healthy characteristics of the bladder. To this end, we must identify the relevancy of different animals as models of human bladder mechanics.

Several studies exist that characterize either the human bladder or pig bladder. However, differences in mechanical testing protocols between studies leads to high variation in observed mechanical properties within the same species. This makes it difficult to infer the utility of the pig bladder as an effective model for human bladder mechanics. The first goal of this dissertation is to directly compare the mechanics of the human and pig bladder tested under identical conditions. To do this we have employed constitutive modeling of uniaxial tensile data from human and pig bladder specimens, and shown anisotropic behavior and comparable mechanical behavior between pig and human bladders.

The second goal of this dissertation is to assess the viscoelastic properties of the porcine bladder wall, and how they are affected by anatomical location and osmotic swelling. In certain pathological conditions degradation of the urothelium can expose the bladder wall to osmotic challenge from urine, changing the hydration level, and consequently, viscoelastic behavior of the

tissue. Through osmotic swelling of pig bladder tissue, stress-relaxation testing, and viscoelastic constitutive modeling we have shown that high levels of urine osmolarity may lead to increased relaxation times that could increase the stress state of the bladder wall and be a driving factor in pathological remodeling.

The final goal of this dissertation is to identify how a pathological condition, i.e., spinal cord injury, can affect bladder extracellular matrix morphology and compliance in the long-term. Prior studies on rat bladder mechanics after spinal cord injury have shown increased capacity and compliance of the bladder post-injury in the short-term. Through imaging, histological analysis, mechanical testing, and constitutive modeling of the long-term spinal cord injured rat bladder extracellular matrix, we have shown profound remodeling of collagen in the bladder wall after spinal cord injury, leading to an increase in capacity, and compliance. It is likely that increase in compliance is a result of the increase in fiber waviness that is seen in our histological analysis, which was predicted by our structural fiber-recruitment constitutive model.

TABLE OF CONTENTS

LIST OF TABLES	vii
LIST OF FIGURES	viii
CHAPTER 1 - LITERATURE REVIEW	1
1.1. Background	1
1.1.1. Anatomy & physiology	1
1.1.2. Mechanical properties	2
1.1.2.1 Viscoelasticity	3
1.1.2.2 Hyperelasticity	4
1.1.2.2 Fiber reinforced composite.....	5
1.1.3. Neurogenic bladder	6
1.2. Experimental studies.....	8
1.2.1 <i>In vivo</i> studies.....	9
1.2.2. <i>Ex vivo</i> studies.....	10
1.2.2.1. <i>Ex vivo</i> small-animal studies	10
1.2.2.2. <i>Ex vivo</i> large-animal studies	12
1.2.2.3. <i>Ex vivo</i> animal studies of the bladder extracellular matrix	14
1.2.2.4. <i>Ex vivo</i> human studies.....	16
1.3. Viscoelastic modeling.....	17
1.3.1. Animal models of health and disease	18
1.3.1.1. Models informed by data collected <i>in vivo</i>	18
1.3.1.2. Models informed by data collected <i>in vitro</i>	19
1.3.1.3. Models informed by data collected both <i>in vivo</i> & <i>in vitro</i>	20
1.3.2. Human models of health and disease	21
1.3.2.1. Models informed by data collected <i>in vitro</i>	21
1.3.2.2. Models informed by data collected both <i>in vivo</i> and <i>in vitro</i>	22
1.4. Hyperelastic modeling	22
1.4.1. Continuum/exponential models	23
1.4.2. Fiber recruitment models	26
1.4.2.1. Quantification of fiber waviness.....	27
1.4.2.2. Fiber recruitment model structural theory.....	27
1.4.2.3. Fiber recruitment models of the bladder	28
1.5 Objectives of this dissertation	28
CHAPTER 2 - DIRECT COMPARISON OF HEALTHY HUMAN AND PIG BLADDER TISSUE MECHANICAL PROPERTIES	30
2.1. Overview	30
2.2. Methods.....	31
2.2.1. Tissue preparation	31
2.2.2. Mechanical testing.....	33
2.2.2.1. Uniaxial testing.....	33

2.2.2.2. Compression testing.....	35
2.2.3. Constitutive modeling	35
2.2.3.1. Fiber recruitment (M1).....	35
2.2.3.2. Continuum model (M2).....	37
2.2.3.3. Material parameter estimation	39
2.2.4. Statistical analysis	41
2.3. Results.....	42
2.3.1. Collagen recruitment model (M1).....	42
2.3.2. Continuum model (M2).....	43
2.3.3. Modeling of compression tests	47
2.4. Discussion	48
2.4.1. Validation of model M2 using compression data	48
2.4.2. High stress, orthotropic contribution to mechanical behavior	49
2.4.3. Species-specific mechanical behavior	50
2.4.4. Porcine tissue anisotropy	50
2.4.5. Limitations	52
2.5 Acknowledgements.....	54
APPENDIX.....	55

CHAPTER 3 - EFFECTS OF SWELLING ON THE VISCOELASTIC BEHAVIOR OF THE PORCINE URINARY BLADDER WALL	58
3.1. Overview	58
3.2. Methods.....	60
3.2.1. Tissue procurement	60
3.2.2. Experimental protocols.....	60
3.2.2.1. Tissue swelling	60
3.2.2.2. Stress-relaxation.....	63
3.2.3. Data analysis	65
3.2.3.1. Tissue swelling	65
3.2.3.2. Stress-relaxation.....	66
3.2.4 Modeling.....	67
3.2.4.1 Modified Maxwell-Wiechert model	67
3.2.4.2 Parameter estimation.....	69
3.2.5 Statistical analysis	69
3.3. Results.....	70
3.3.1. Tissue swelling.....	70
3.3.2. Stress relaxation experimental data.....	71
3.3.3. Modeling results.....	74
3.4. Discussion	77
3.4.1. Tissue swelling.....	77
3.4.2. Stress-relaxation	78
3.4.3. Modeling.....	79
3.4.4. Limitations	81
3.5 Conclusions	82
APPENDIX.....	84

CHAPTER 4 - CHANGES IN MORPHOLOGY AND COMPLIANCE IN THE LONG-TERM SPINAL CORD INJURED RAT BLADDER EXTRACELLULAR MATRIX.....	86
4.1. Overview	86
4.2. Methods.....	87
4.2.1. Animal groups and tissue preparation	87
4.2.2. Geometry estimation	88
4.2.3. Histology.....	88
4.2.4. Mechanical testing.....	89
4.2.4. Constitutive modeling	91
4.2.5.1. Fiber recruitment model.....	91
4.2.5.2. Exponential model	94
4.2.6. Statistical analysis	94
4.3. Results.....	95
4.3.1. Ring circumference	95
4.3.2. Histology.....	95
4.3.3. Mechanical testing.....	99
4.3.4. Constitutive modeling	100
4.4. Discussion	102
4.5 Limitations	107
4.6 Conclusions	108
APPENDIX.....	110
 CHAPTER 5 - CONCLUSIONS AND FUTURE WORK.....	 112
5.1 Conclusions	112
5.2 Future work.....	113
 BIBLIOGRAPHY.....	 114

LIST OF TABLES

Table 2.1 Donor demographic information: age, sex, and cause of death	33
Table 2.2 Parameter estimates for M1, NRMSE for each supraphysiologic loading fit, and λ_{toe} representing stretch for 5% collagen recruitment for each group.....	42
Table 4.1 Parameter estimates for the fiber recruitment and exponential continuum models for all samples	111

LIST OF FIGURES

Figure 1.1 Anatomy of the human bladder [6].	2
Figure 1.2 (a) Schematic of the bladder in the sagittal plane, and (b) image of a cut open porcine bladder with anatomical regions labeled [7].....	3
Figure 1.3 Uniaxial stress-relaxation curves for porcine bladder strips in the longitudinal and circumferential directions for strains of (a) 0.2, (b) 0.5, (c) 1.0, and (d) 2.0 [16]	4
Figure 1.4 Stress-strain curves from uniaxial tensile tests if bladder from (a) dorsal, (b) ventral, (c) lateral, (d) lower body, and (e) trigone regions, showing consistently stiffer behavior in the apex-to-base direction [7].....	5
Figure 1.5 Multiphoton images of collagen in the bladder during loading in the (a) toe regime and (b) transition regime [9].....	6
Figure 1.6 Histological images of normal (A, C) and spinal cord injured (B, D) rat bladders. The top images show increased thickness in the SCI bladder compared to controls. In the bottom images, more elastin fibers are present in the SCI bladder than the control [21].	8
Figure 1.7 Depiction of cystometric test and resulting pressure/volume relationships for filling and voiding [23].....	9
Figure 1.8 (a) Maximum stretches and (b) maximum areal strains obtained from stress mediated biaxial tensile tests for healthy and SCI rat bladders with different durations of SCI [31].	12
Figure 1.9 Maxwell-Wiechert viscoelastic model with two Maxwell elements [56].	18
Figure 1.10 Pressure-volume cystometric data from dogs, along with pressure-volume predictions for (a) prolate, and (b) oblate spheroidal bladder models with varying eccentricities [76].	26
Figure 2.1 <i>Sample orientation schematic and uniaxial sample preparation.</i> a) The trigone is removed from whole bladder and a steel die produce dumbbell specimens (inset). Also shown are the transverse and longitudinal directions, as well as schematics of orientations of specimens. b) Pictured is a representative tissue specimen mounted in the uniaxial tester.	33
Figure 2.2 <i>Testing protocol for tissue specimens and representative data - model prediction results.</i> a) Stretch versus time graph showing three load-unload cycles and the timing of those cycles, and b) stress versus stretch graph showing loading data (symbols) of a single specimen and its corresponding model prediction curves (lines) for Pulls 1, 2, and 3.	34
Figure 2.3 <i>Schematic diagram of collagen recruitment model.</i> Gradual engagement of collagen fibers (top row) are modeled by spring elements (bottom row). As the model/tissue is stretched	

(left to right), the hooks engaging the bar is mirrored by the straightening of the collagen fibers, and the stretching of the springs represents the stretching of the individual collagen fibers.36

Figure 2.4 *Multi-step parameter estimation approach.* a) Representative plot demonstrates the regions used for parameter estimation of the isotropic and orthotropic strain energy functions W^{am} and W^f , respectively, as well as representative sample data and M2 model output. b) Collagen fiber recruitment model, M1, used to estimate fiber recruitment distribution. c) Representative suprathysiologic data ($\lambda \in [1,2.6]$) and M1 model output after parameter estimation. d) Plot of fiber recruitment distribution that shows λ_{toe} is calculated as the stretch at which 5% of collagen fibers are recruited. λ_{toe} is used as the cutoff point for the stretch range used for parameter estimation of W^{am}41

Figure 2.5 *Normalized root mean square error (NRMSE) and standardized residuals for all data.* Histograms of (a) NRMSE for all fitted curves, where nc represents number of fitted curves, and (b) standardized residuals for all data points included in the fitting process, where nr represents number of residuals.45

Figure 2.6 *Human and porcine fitted curves under different treatment conditions.* M2 model output using median parameter values (lines) and interquartile range of experimental data (shaded) for a) untreated (un) and oxybutynin treated (ox) specimens in humans, and b) untreated (un), oxybutynin treated (ox), and untreated transverse (un) specimens in pigs. Plot titles represent treatment, with superscript denoting direction ($f = 1$ for longitudinal, $f = 2$ for transverse), and subscript denoting number of samples. Only groups containing 4 or more samples are shown.45

Figure 2.7 *Parameter Estimates.* Estimated values for cam (a), $c1f$ (b), $c2f$ (c) are displayed in box plots (median line, box first quartile - third quartile, error bar 0th and fourth quartiles). The results shown include parameter values estimated for both humans (left) and pigs (right). Only groups containing 4 or more samples are shown, all parameter estimates can be found in an open source online repository.46

Figure 2.8 *Calculated values of stress at λ_{toe} .* Box plots representing the experimentally recorded stress values at λ_{toe} for humans (left) and pigs (right). Only groups containing 4 or more samples are shown.47

Figure 2.9 *Comparison of compressive behavior experimentally measured and predicted by model M2.* Symbols represent the experimental data from compression tests in untreated pig samples (testing data-set). The line represent the model prediction for a compression test calculated using median parameter values estimated from uniaxial experiments for untreated pig tissue (training data-set).47

Figure 2.10 *Fiber orientation assessment.* a) Photomicrographs of Verhoff Van Gieson (VVG) stained regions human and pig, tested and untested specimens at 400x (scale bar 100 μ m). In VVG stain, elastin and cell nuclei are dark blue/black, collagen is red/magenta, and other tissue elements are light brown/yellow. b) Bladder specimens were sectioned at 5 μ m along the axis of pull to maximize fiber orientation analysis. Fibrous regions were selected within specimens (shaded, center) and fiber orientation determined within selections (right, n=4 selections per

specimen). Hue corresponds to the fiber angle (right, inset). c) Fiber orientation distributions (averaged over section) relative to the pulled direction in longitudinal pig and human specimens.57

Figure 3.1 Representative bladder after being dissected and flattened. Schematic representations of the locations and number of samples taken from each bladder for (a) the swelling study (9mm diameter punch samples), (b) the anatomical location and (c) the variable-solution osmolarity stress-relaxation experiments. The rectangular punch measured 10mm × 30mm for the samples shown in both (b) and (c).....62

Figure 3.2 Side view (a) and top view (b) of representative 9mm diameter punch sample for the swelling experiment, before (left) and after (right) manual thresholding. Top view (c) and side view (d) of representative 10mm × 30mm rectangular punch sample for the stress-relaxation experiments, before (left) and after (right) manual thresholding. Binary images (left column) show a schematic of all relevant geometric definitions for the evaluation of volume and cross-sectional area, see Equations (3.1)-(3.3).62

Figure 3.3 Stress-relaxation protocol for a representative sample. Applied strain (top) and recorded force (bottom) data, as a function of test time. This protocol was employed in all stress-relaxation experiments (i.e., anatomical location and variable solution osmolarity).64

Figure 3.4 Schematic of the modified Maxwell-Wiechert model. The standalone spring’s stiffness increases exponentially with strain (\hat{k}_i^0), while the springs in the three Maxwell elements have stiffnesses that increase linearly with strain (k_{ij}). The dashpots are standard linear dampers (η_j).69

Figure 3.5 Relative mass (m , top) and relative volume (V , bottom) for the different solution osmolarities and anatomical locations, namely dorsal (D), ventral (V), lateral (L), lower body (LB), and trigone (T). Each bar represents the mean and standard deviation from 5 bladders. For 100 mOsm/L, all samples have a $m > 1$ and almost all samples (24 of 25, 96%) have $V > 1$. For 300 mOsm/L, all samples have $m > 1$, D and V samples all have $V > 1$, but some L (1 of 5), LB (2 of 5), and T (1 of 5) samples have $V < 1$. For 600 mOsm/L some D (2 of 5) and L (1 of 5) samples have $m < 1$ and about half of all samples show $V < 1$ (13 of 25, 52%). For 900 mOsm/L some D (2 of 5), V (2 of 5), and L (1 of 5) samples have $m < 1$ and over half of all samples show $V < 1$ (16 of 25, 64%).71

Figure 3.6 Stress-relaxation curves as a function of time relative to the start of each loading step for a representative sample. The same data is shown for a linear timescale (top) and logarithmic timescale (bottom). The number of data points in each curve is 200 and have been identified by using a customized logarithmic-like spacing. A grey-scale color gradient has been employed to represent the different values of applied strain, from the lightest representing the smallest strain in the protocol ($\hat{\epsilon}_1 = 0.25$) to the darkest representing the largest strain in the protocol ($\hat{\epsilon}_5 = 2.0$).73

Figure 3.7 Stress-relaxation results for all samples showing peak stresses ($\hat{\sigma}_i^p$, left) and relaxed stresses ($\hat{\sigma}_i^r$, right) for different anatomical locations (top) and osmolarities (bottom). Open symbols are used to identify the anatomical location experiments and closed symbols to identify

the varying solution osmolarity experiments. A grey-scale color gradient has been employed to represent the different values of applied strain, from the lightest representing the smallest strain in the protocol ($\hat{\epsilon}_1 = 0.25$) to the darkest representing the largest strain in the protocol ($\hat{\epsilon}_5 = 2.0$). An asterisk represents a statistically significant difference ($p < 0.05$) and the relevant comparison is represented by an arrow.74

Figure 3.8 Estimated values of the parameters for the modified Maxwell-Wiechert model when considering the anatomic location experiment. Open symbols are used to identify the different anatomical locations (as specified in the legend). An asterisk represents a statistically significant difference ($p < 0.05$) and the relevant comparison is represented by an arrow.....76

Figure 3.9 Estimated values of the parameters for the modified Maxwell-Wiechert model when considering the variable solution osmolarity experiment. Closed symbols are used to identify the different solution osmolarities (as specified in the legend). An asterisk represents a statistically significant difference ($p < 0.05$) and the relevant comparison is represented by an arrow.77

Figure 3.10 Model description for a representative dataset. All plots show the same experimental data (solid circles) and model description (solid line), each with a different timescale representation. The top represented the consecutive loading steps as a function of testing time. The bottom figures represent the loading steps as a function of time relative to the start of each loading step shown for a linear timescale (left) and logarithmic timescale (right). The normalized root mean squared error (NRMSE) averaged between all samples is 0.0222 for the exponential spring parameter estimation step and 0.0377 for the entire stress-relaxation curve.....85

Figure 4.1 Visual representation of the fiber recruitment model. As deformation is applied, springs engage, increasing the stiffness of the response.93

Figure 4.2 Representative stress-stretch data with model fit from the fiber-recruitment model (top) and exponential continuum model (bottom). For the fiber-recruitment model, E_0 is initial slope, E_1 is final slope, and λ_m is the mean recruitment stretch defined by the intersection of the initial and final slope lines.....93

Figure 4.3 (a) Ring images before and after decellularization and traced edges, and (b) mean \pm standard deviation for ring circumference before and after decellularization for control, sham, and paraplegic groups.....95

Figure 4.4 PSR (left two columns) and VVG (right two columns) stained bladders in the plane normal to the longitudinal direction from control (left) and paraplegic (right) rats in the lamina propria (top), detrusor (middle), and adventitia (bottom)97

Figure 4.5 Regions of interest from a 14-week paraplegic rat bladder showing an area of high collagen density (PSR, left) and high amounts of elastin (VVG, right)97

Figure 4.6 Planar images from control (left) and 1-week paraplegic (right) rat bladders in the lamina propria (top) and detrusor (bottom)98

Figure 4.7 Mean fiber orientation distributions for control and 1-week paraplegic rat bladders in the lamina propria (top) and detrusor (bottom) with different local fiber angle weighting.

Coherency weighting (left) give high weight to formerly muscular regions as well as collagenous regions. Weighting by the product of energy and intensity (right) gives lower weighting to previously muscular areas, while keeping high weighting in collagenous regions.98

Figure 4.8 Stress-stretch curves (mean \pm standard deviation) from control, sham, and paraplegic groups. Stretch values at different levels of stress are significantly higher in the paraplegic group when compared to the sham group (arrow) and the sham and control groups combined (bracket).99

Figure 4.9 Mean \pm standard deviation of stretch values at 100 kPa stress for control, sham, and paraplegic groups. The paraplegic group shows significantly higher stretch than the sham group (arrow) and the sham and control groups combined (bracket). 100

Figure 4.10 Opening angle images at (a) 0 minutes and (b) 90 minutes post-cut, and (c) mean \pm standard deviation of opening angle vs time from control and paraplegic groups 100

Figure 4.11 Mean \pm standard deviation parameter values for the fiber-recruitment model (E_0 , E_1 , λ_m , λ_{sd} , α , β), and exponential continuum model (c_1 , c_2) 101

CHAPTER 1 - LITERATURE REVIEW

1.1. Background

1.1.1. Anatomy & physiology

The lower urinary tract is composed of the urinary bladder, internal and external urethral sphincters, and urethra. **Figure 1.1** shows a diagram of the basic anatomy of the bladder, as well as the structure of the bladder wall. The bladder wall has multiple layers. The inner layers, consisting of the transitional epithelium, lamina propria, and submucosa, act as a barrier between urine and the middle layer, which consists of muscle. The muscle of the bladder is the detrusor. The outermost layer is the adventitia, which is a layer of fibrous connective tissue surrounding the organ. The bladder wall consists of **smooth muscle cells (SMCs)** and **extracellular matrix (ECM)**. The ECM, which is comprised of proteins, proteoglycans, and glycosaminoglycans, acts as a support structure that gives strength and compliance to the bladder. Collagen I and III make up the majority of the ECM, and accounts for approximately 30% of intact bladder dry-weight in humans [1–3]. Elastin in the bladder is thought to allow the tissue to recover to its original configuration after being stretched [4].

The lower urinary tract functions in two stages: storage, and voiding. During storage, a healthy bladder maintains a low, relatively constant, pressure. This is achieved through relaxation of the bladder wall as the organ fills. During voiding, contraction of the detrusor and relaxation of the urethral sphincters must occur simultaneously. This is accomplished through a combination of somatic and autonomic innervation. The detrusor and internal urinary sphincter contain SMCs and are under involuntary control (autonomic innervation), whereas the external urinary sphincter is composed of skeletal muscle and is under voluntary control (somatic innervation) [5].

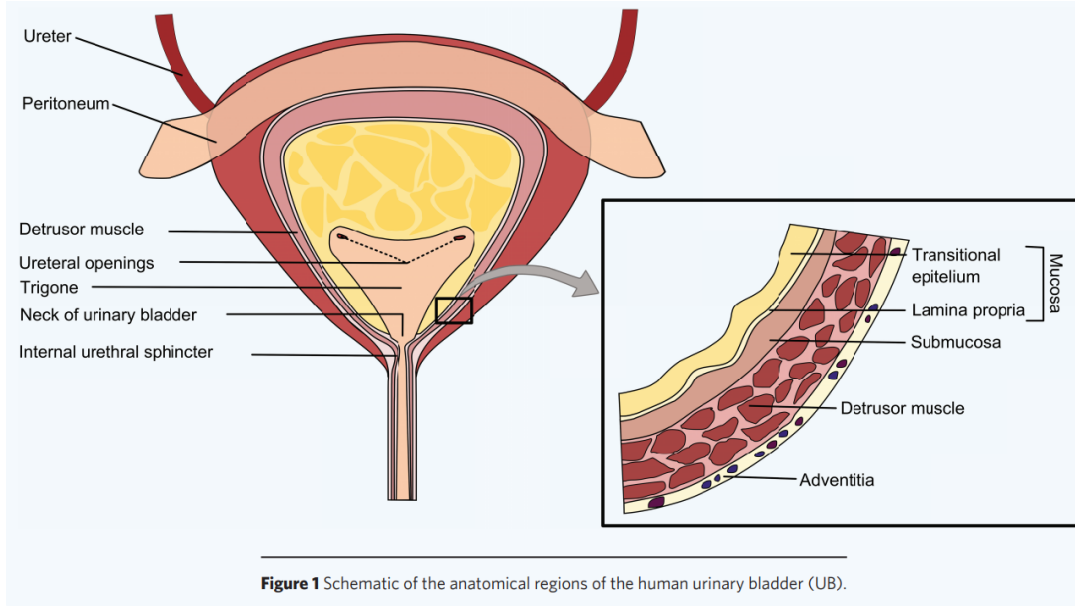


Figure 1.1 Anatomy of the human bladder [6].

1.1.2. Mechanical properties

The bladder is one of the most physically dynamics structures in the body. The ability to drastically increase in size while maintaining low pressure makes the mechanical properties of the bladder wall an interesting research topic. Because of the prevalence of lower urinary tract pathologies that correlate with tissue mechanical dysfunction, it is important to understand the mechanical characteristics of the bladder wall, both in healthy and pathological conditions. The mechanical behavior of the bladder wall can be described as viscoelastic, however hyperelastic models have been successfully used to describe the preconditioned behavior of the bladder wall. The mechanical characteristics of the bladder differ between different anatomical locations (i.e., dorsal, ventral, lateral, lower-body, trigone) [7,8] and orientations (i.e., longitudinal/apex-to-base and circumferential/transverse) [7–15]. **Figure 1.2** shows anatomical regions of the bladder that have been studied previously [7].

An effective way of analyzing mechanical behavior is through the use of constitutive models. Constitutive models, which can be either phenomenological or microstructurally

motivated, can give insight into mechanical behavior that is not possible to observe from purely experimental data. Three types of constitutive models are of interest: viscoelastic, hyperelastic, and fiber recruitment models, which are a particular type of hyperelastic model.

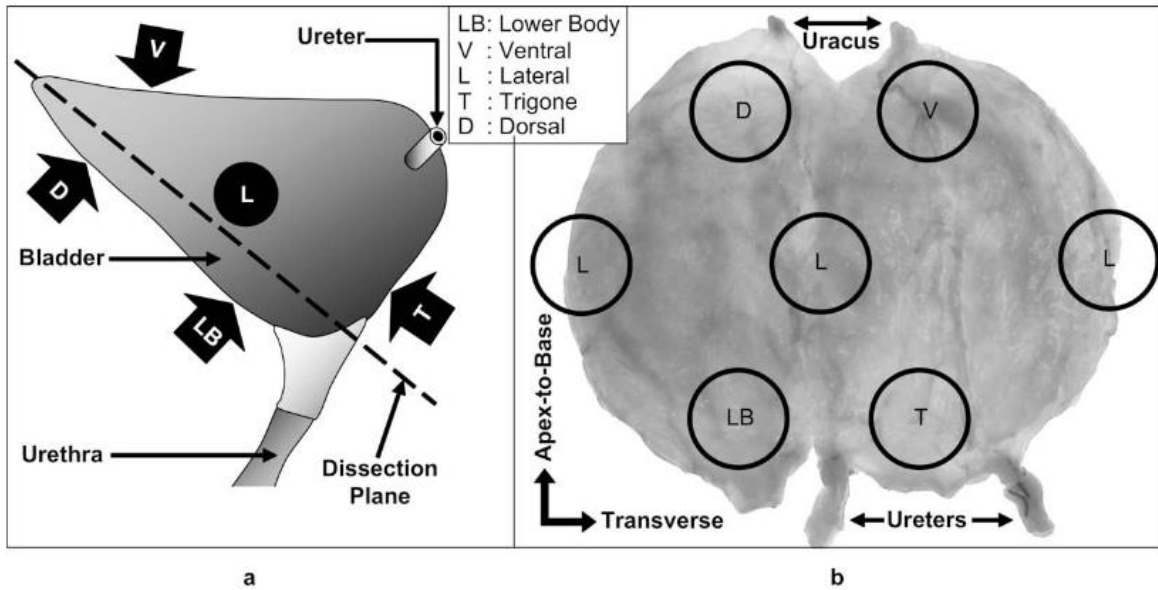


Figure 1.2 (a) Schematic of the bladder in the sagittal plane, and (b) image of a cut open porcine bladder with anatomical regions labeled [7].

1.1.2.1 Viscoelasticity

When a material behaves in both a viscous and an elastic manner, it is termed viscoelastic. When a viscoelastic material undergoes deformation, the resultant stress depends on both the amount of strain and the strain rate (or more generally, the strain history as a whole). Viscoelastic behavior of materials is commonly modeled using spring-damper models, where springs and dampers represent the elastic and viscous behavior, respectively. Common experiments used to measure viscoelastic behavior include stress-relaxation, creep tests, and **dynamic mechanical analysis (DMA)**. A stress-relaxation test involves rapidly deforming a sample and measuring the resulting stress over time at a constant level of stretch. **Figure 1.3** shows sample stress-relaxation data for porcine bladder strips at various levels of stretch [16]. Creep tests involve rapidly deforming a sample to a specified level of stress, and continuously deforming the sample to maintain that level

of stress. DMA involves applying a sinusoidal stress in order to estimate a storage modulus and loss modulus that describe the elastic and viscous behavior of the material, respectively.

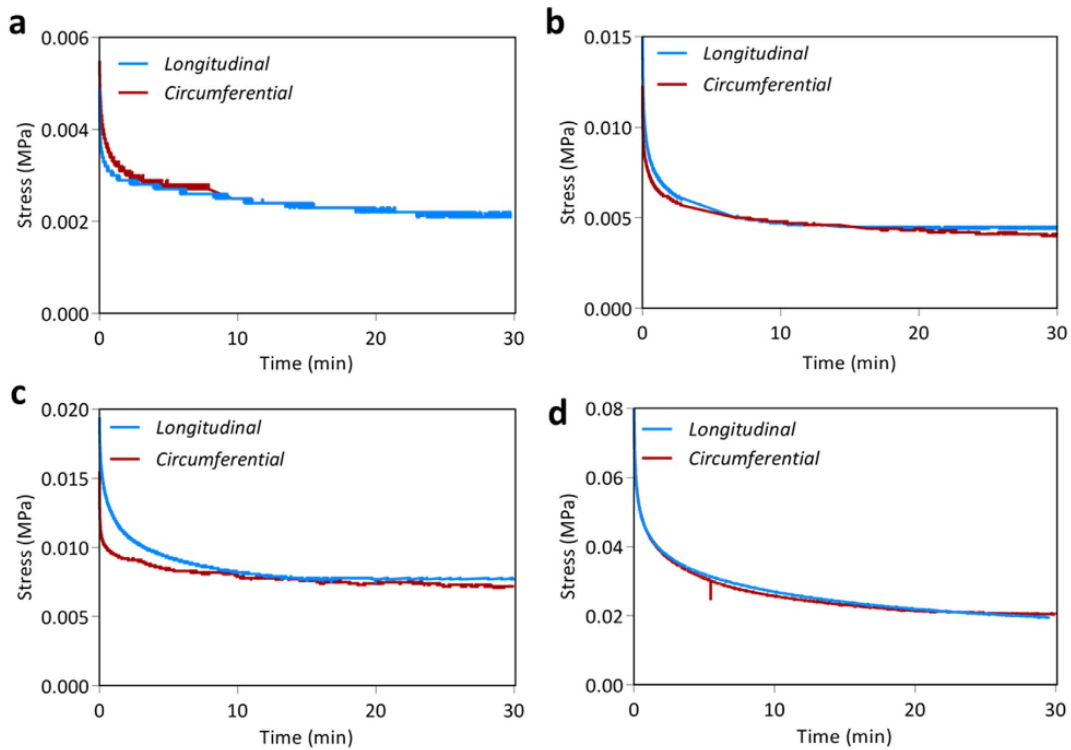


Figure 1.3 Uniaxial stress-relaxation curves for porcine bladder strips in the longitudinal and circumferential directions for strains of (a) 0.2, (b) 0.5, (c) 1.0, and (d) 2.0 [16]

1.1.2.2 Hyperelasticity

For a material to be considered hyperelastic, its stress-strain curve must be repeatable and independent of strain rate. Hyperelastic material models are derived from strain energy functions, and are generally used when linear elastic models do not accurately describe the material behavior. For biological tissues, hyperelastic models are used when tissue is deformed at rates low enough that viscous effects are negligible. The most common experiments used to estimate material parameters within hyperelastic models are uniaxial and biaxial tensile tests with multiple loading and unloading cycles, applied at a constant strain rate. **Figure 1.4** shows stress-strain curves for one loading cycle of uniaxial tensile tests on porcine bladder strips.

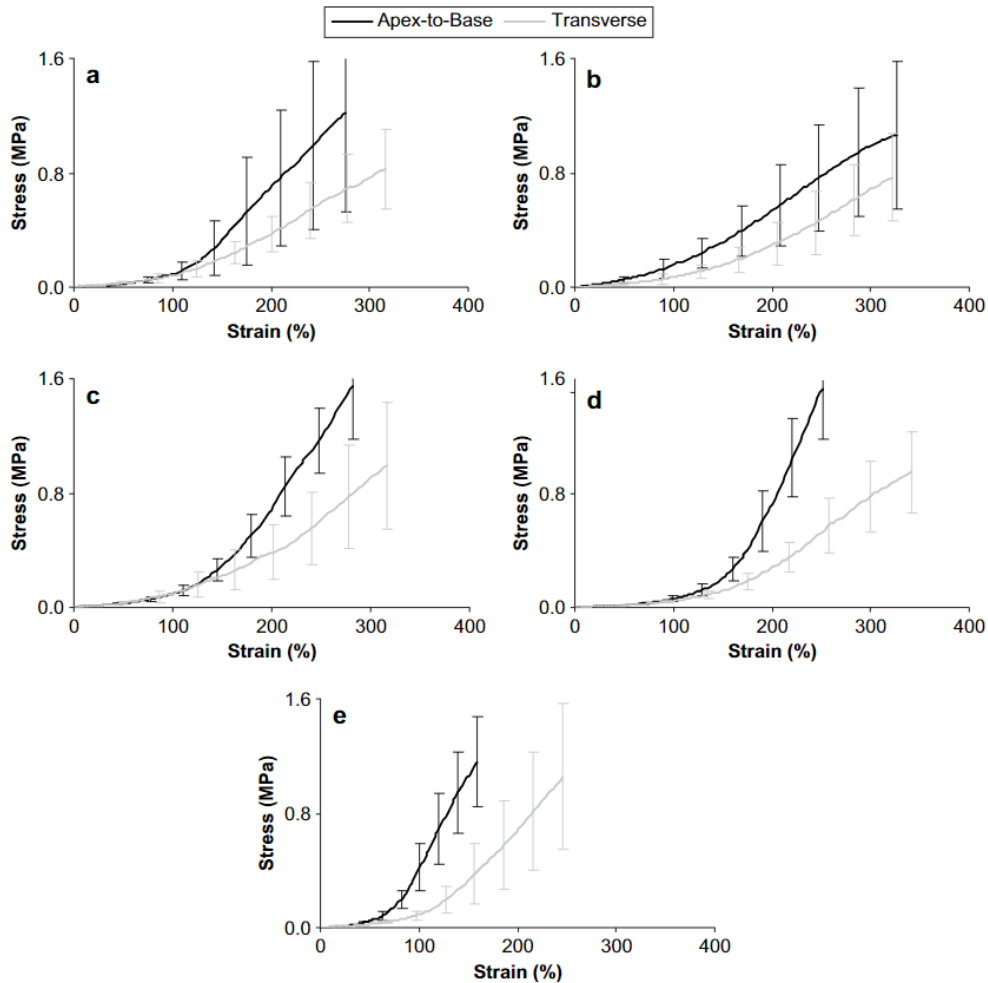


Figure 1.4 Stress-strain curves from uniaxial tensile tests of bladder from (a) dorsal, (b) ventral, (c) lateral, (d) lower body, and (e) trigone regions, showing consistently stiffer behavior in the apex-to-base direction [7].

1.1.2.2 Fiber reinforced composite

Soft tissues that contain collagen and elastin fibers, which are generally coiled or wavy, can be considered as fiber reinforced composites. When a tissue within this category undergoes deformation, the fibers begin to straighten and cause the tissue stiffness to increase. **Figure 1.5** shows multiphoton images of rat bladder at different levels of stretch, clearly showing the recruitment of collagen fibers with increased stretch. This type of material can be described using a fiber recruitment model, which is a subcategory of hyperelastic models that takes this phenomenon into account. In a fiber recruitment model, it is assumed that there are a large number

of wavy collagen fibers. When the tissue is stretched, the fibers begin to straighten and engage. If one assumes that fibers have a distribution of waviness values that can be described by a probability density function, and each individual fiber is linearly elastic after it has straightened, then the resulting stress-stretch curve will have a nonlinear quality to it. The resulting shape matches what has been observed in many soft collagenous tissues.

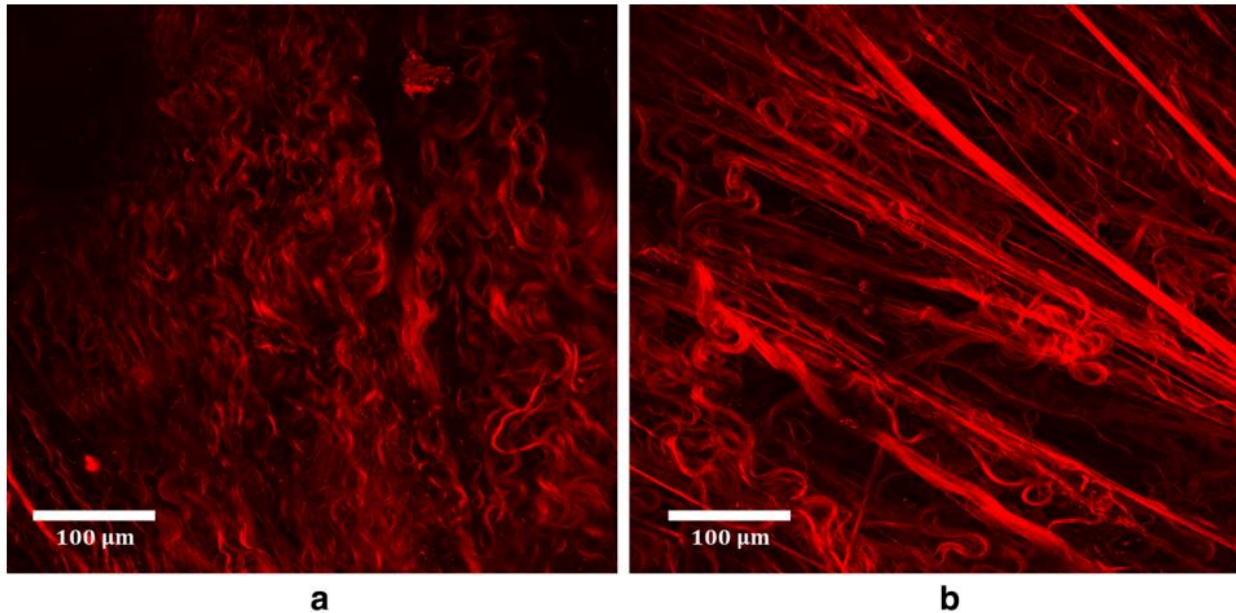


Figure 1.5 Multiphoton images of collagen in the bladder during loading in the (a) toe regime and (b) transition regime [9].

1.1.3. Neurogenic bladder

Because the function of the bladder relies heavily on neurological pathways, loss of neurological connection can be detrimental to the bladder and lower urinary tract as a whole. A bladder with decreased or absent neurological connection to the brain is termed a “neurogenic bladder”. A neurogenic bladder can lead to many lower urinary tract symptoms, as well as hydronephrosis, renal damage, **urinary tract infections (UTIs)**, calculus disease, bladder cancer, and sexual dysfunction [17]. Neurogenic bladders are seen in a high percentage of individuals with various neurological conditions. Voiding dysfunction is seen in 80% of persons with multiple sclerosis [18], and 70-84% with **spinal cord injury (SCI)** [19]. Manack et al. showed over the course of 1

year (data collected in a group of 46,271 patients with a neurogenic bladder), patients averaged 16 office visits and 0.5 emergency room visits, 39% of patients visited a urologist, and UTI diagnosis comprised over 20% of the recorded hospitalizations [19].

Neurogenic bladder pathology can present itself in different forms, based on several factors including specific neurological disorder and location of neurologic lesion [20]. Neurogenic bladder behavior can include healthy, spastic, or flaccid behavior of the detrusor and/or the urethral sphincters, leading to high/low storage volumes and storage pressures. Furthermore, a pathological change in storage volume and storage pressure in the bladder is associated with a change in the stress/stretch experienced by the bladder wall. Subsequently, as seen in many load bearing biological tissues, deviation from the homeostatic stress/stretch state of a tissue for an extended period of time results in remodeling, and thus a change in material properties of that tissue. **Figure 1.6** shows histological images of healthy and SCI rat bladder wall [21]. It is clear that remodeling of the SCI bladder has led to increased wall thickness and increased concentration of smooth muscle and elastin fibers. It has been shown that in the SCI rat bladder, SMCs are oriented both longitudinally and circumferentially, whereas healthy rat bladders show SMC orientation predominantly in the longitudinal direction, which validates the more isotropic mechanical behavior seen in the SCI rat bladder [22].

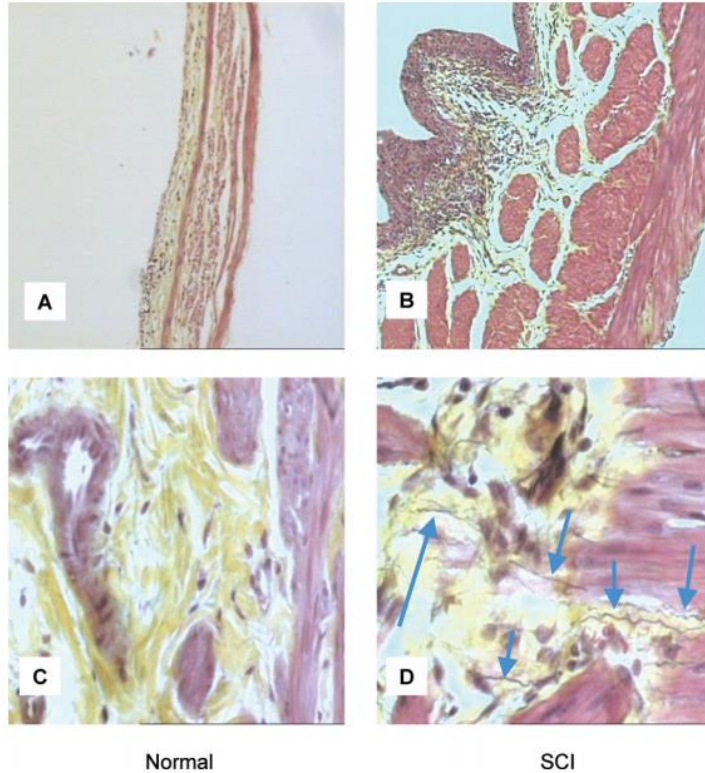


Figure 1.6 Histological images of normal (A, C) and spinal cord injured (B, D) rat bladders. The top images show increased thickness in the SCI bladder compared to controls. In the bottom images, more elastin fibers are present in the SCI bladder than the control [21].

1.2. Experimental studies

Experimental studies are essential for understanding how the bladder wall mechanics change in response to pathological conditions. Experimental data generally allows for both qualitative and quantitative observations of the behavior of healthy and pathological tissue. In addition to the types of *in vitro* experiments that were previously mentioned, *in vivo* and *in vitro* cystometric tests are also common in the bladder. Cystometry involves filling the bladder and recording pressure-volume data. **Figure 1.7** shows a diagram of a cystometric experiment for filling and voiding along with sample data [23]. These tests can be stepwise cystometry (viscoelastic) or slow and constant fill rate (hyperelastic). Some studies incorporate a combination of experiments and constitutive modeling. The following sub-sections will describe *in vivo* and *in vitro* studies that are purely

experimental in nature, while studies with a combination of experiments and modeling will be discussed in later Sections (1.3-1.4).

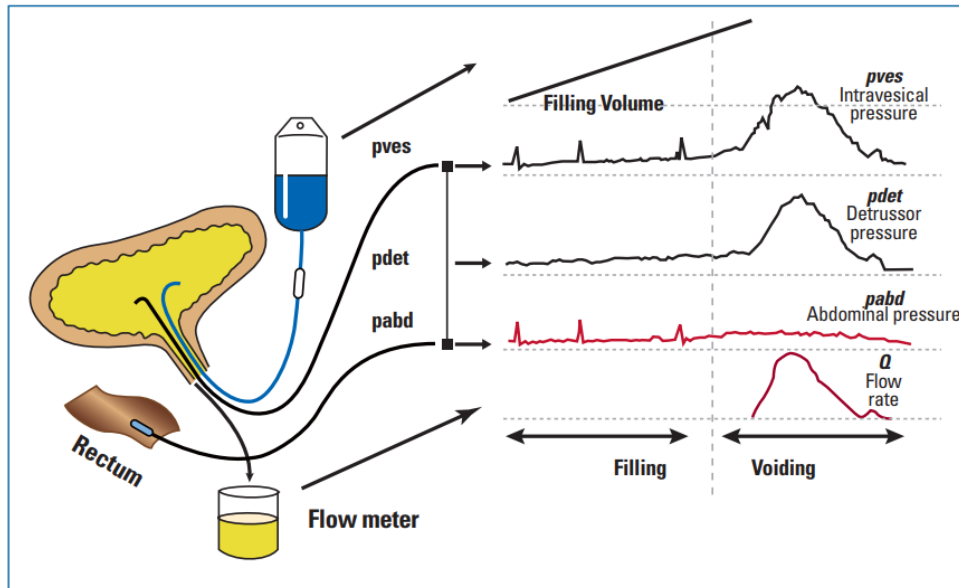


Figure 1.7 Depiction of cystometric test and resulting pressure/volume relationships for filling and voiding [23].

1.2.1 *In vivo* studies

Cystometry is the most common *in vivo* mechanical test for the bladder. Cystometric studies are used clinically as diagnostic tests [23] and are a way to assess bladder compliance and capacity in humans. Therefore, it is useful to run cystometric studies on animals to compare compliance and capacity between species. This information can provide insight into the utility of different animal models as models for humans. Using medium fill cystometry, Wyndaele showed strong correlation between desire to void and bladder volume and pressure in healthy young humans [24]. Klevmark showed that bladder pressure during filling is more dependent on rate of filling than on volume. These results were shown in both cats and humans [25,26]. Wang et al. ran *in vivo* cystometric experiments and *in vitro* biaxial tensile tests on diuretic rat bladders; they found increased weight, capacity, and compliance in the diuretic rat bladder compared to controls. The purpose of this study was to isolate the diuretic effects on the bladder from the neuropathic effects induced by

diabetes [27]. Watanabe et al. used cystometry to evaluate the effect of oxybutynin on rat bladder wall stiffness and found significant decrease in bladder stiffness and increase in compliance with oxybutynin compared to controls [28].

1.2.2. *Ex vivo* studies

When compared to *in vivo* studies, *in vitro* studies have an advantage in terms of performing more precisely controlled mechanical manipulations, allowing for quantification of isotropy and homogeneity of mechanical properties. Additionally, *in vitro* testing aids in the understanding of what is happening microstructurally, which would not be possible with whole organ *in vivo* testing. Most *in vitro* experimental studies on the bladder focus on animal models. Studies that focused on human tissues are few, due to difficulties of obtaining tissue. *Ex vivo* animal studies are generally conducted on either small animals (i.e., rats, guinea pigs, rabbits), or large animals (i.e., dogs, pigs, cows).

1.2.2.1. *Ex vivo* small-animal studies

Small animals are attractive biological models to use due to the availability, lower cost of caring, and the ability to study mutations, diseases, and injuries more easily than in large animals. Some experimental studies on small animal bladders are described in this section. Passive mechanical behavior will be discussed first, followed by active mechanical behavior.

Finkbeiner et al. showed the passive mechanical response of rat and guinea pig bladder strips at various strain rates using uniaxial tensile tests with strain rates ranging from 0.5 cm/hr to 3 cm/hr, and found no difference in response of the tension-length curves [29]. These results suggest that at low stretch rates, viscoelastic effects are minimal. This is an important finding that supports the use of hyperelastic models for mechanical testing of rodent bladders. Gloeckner et al. employed biaxial tensile tests to measure the increase in compliance in bladders of rats 10 and 14

days after SCI from [30]. Toosi et al. measured changes in compliance of the bladder of rats 3, 6, and 10 weeks post SCI using biaxial tensile tests, and found that compliance increases from 3 to 6 weeks but returns close to healthy compliance 10 weeks after the injury. Compliance was determined based on the maximum stretch and maximum areal strain reached during stress-mediated equibiaxial tensile tests. Areal strain was defined as,

$$Areal\ strain = \lambda_{long}\lambda_{circ} - 1 \quad (1.1)$$

where λ_{long} and λ_{circ} are the longitudinal and circumferential stretches, respectively. **Figure 1.8** shows the maximum strains and maximum areal stretches at time points after induced SCI. The authors suggest that compliance may decrease further for remodeling times longer than 10 weeks post-injury [31]. Parekh et al. ran *in vitro* pressure-volume tests on rat bladders while measuring wall strain by tracking positions of surface markers. Results showed the bladder to be stiffer in the circumferential direction than the longitudinal direction [32]. Eika et al. ran tensile tests and chemical processes to extract collagen content on diabetic rat bladder strips and showed a decrease in collagen content and an increase in compliance of the bladder in diabetic rats, which was not observed in rats treated with insulin [33].

Mattiasson et al. ran active and passive uniaxial tensile tests on feline bladder strips subjected to 12 weeks of parasympathetic sacral decentralization, and found hypertrophy of the detrusor, decreased force production, but no change in active length-tension relations [34]. Ghoniem et al. evaluated the effect of moderate and severe urethral outlet obstruction on the active and passive properties of the rabbit bladder wall and found decreased contractility and increased stiffness in obstructed groups [35]. Levin et al. performed *in vitro* cystometric experiments on whole rabbit bladders to determine the effect of hypoxia, alterations of calcium concentration, and muscarinic agonists and antagonists on bladder capacity and compliance. Results showed increase

in bladder capacity and compliance with hypoxia and calcium concentration, and a decrease in in capacity and compliance with carbachol. Overall conclusions are that alterations in smooth muscle tone in the bladder can have a significant impact on its mechanical behavior [36].

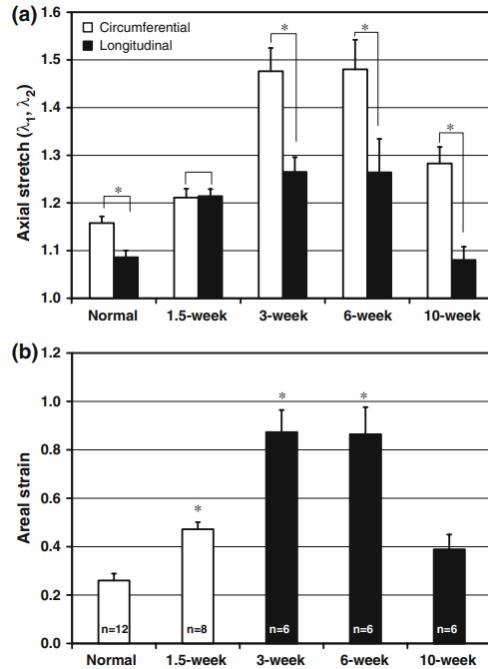


Figure 1.8 (a) Maximum stretches and (b) maximum areal strains obtained from stress mediated biaxial tensile tests for healthy and SCI rat bladders with different durations of SCI [31].

1.2.2.2. *Ex vivo* large-animal studies

Large animals are closer to size and anatomical structure to humans but present higher cost for caring and less availability, particularly for animals with mutations, diseases, or injuries. Some experimental studies on the mechanics of large animal bladders are described in this section. Viscoelastic behavior will be discussed first, followed by passive, and finally active mechanical behavior.

Barnes et al. used DMA to analyze the viscoelastic response of pig urinary bladder strips and loops and found storage modulus (i.e., elastic response) to be markedly greater than loss modulus (i.e., viscous response) [37].

Jokandan et al. provided extensive experimental results for uniaxial tensile, ball-burst, and DMA tests in the porcine bladder. They found the porcine bladder to be stiffer longitudinally than circumferentially at high levels of strain (>200%), and storage modulus to be higher than loss modulus, showing the highly elastic behavior of the bladder [16], agreeing with the findings of Barnes et al. ball-burst tests [37], which more closely mimic physiological loading conditions, showed ultimate stresses ~5 times higher than with uniaxial tensile tests, but with similar rupture strains. Korossis et al. ran uniaxial tensile tests on porcine bladder strips to look for differences in mechanical behavior based on anatomical region and direction. Results showed that region differences were only evident in apex-to-base direction, with dorsal and ventral samples being more distensible than lower-body and trigone regions. Directional differences were seen in all regions, but most notably in lower-body and trigone. Trends showed higher stiffness in the apex-to-base direction than transverse direction [7]. Baskin et al. ran biaxial pressure driven mechanical tests on fetal bovine bladder tissue and found that elastic modulus decreases with gestational age, and increased in adult bovine bladders compared to newborn [38].

Dean et al. ran uniaxial mechanical tests on fetal bovine bladders and found passive compliance to be greatest in younger fetal bladders, which decreased with fetal age, and active compliance to be lowest in younger fetal bladders, which increased with fetal age [39]. Griffiths et al. looked at the active and passive properties of pig bladder strips and found that active isometric force increases linearly with extension until it reaches a maximum where it is similar in size to the passive force [40]. Coplen et al. performed a cystometric study of *in vitro* bovine fetal bladders and found increase in compliance with elimination of active smooth muscle tension and surgical removal of the detrusor muscle [41].

1.2.2.3. *Ex vivo* animal studies of the bladder extracellular matrix

In addition to smooth muscle tone, **extracellular matrix (ECM)** plays an important role in the compliance of the bladder. The bladder ECM is of interest not only for its contribution to mechanical response, but also for its potential in tissue engineering. Tissue engineering is the use of several branches of science including materials science, biochemistry, and biomechanics, to form new tissue that can be used to replace dysfunctional tissues or organs in the body. Organ specific ECM is an attractive material which has been studied for use as a scaffold for growing new functional tissue. ECM is attractive because of its biocompatibility and mechanical properties that are close to that of the tissue they are being used to replace. The bladder's ECM is a frequently studied grafting material because of its unique distensibility, which is difficult to mimic with manufactured materials, and the frequent necessity of partial or whole bladder replacement due to pathological conditions. Some experimental studies of bladder's ECM are as follows.

Freytes et al. looked at the effect of different storage conditions [42], lyophilization [43], and sterilization methods [44] on the mechanical response of porcine bladder ECM through uniaxial tensile and ball-burst tests. Storage of lyophilized porcine bladder ECM for one year in both room temperature and refrigerated conditions resulted in alterations of material properties. No changes in ball-burst strength were observed, but maximum tangential stiffness increased in room temperature samples, while maximum elongation increased in refrigerated samples [42]. When comparing hydrated and lyophilized pig bladder ECM, lyophilized ECM showed irreversible microstructural damage, but little change in observed mechanical properties. Interestingly, lyophilized ECM showed more cells present than hydrated ECM seven days after seeding with NIH 3T3 cells [43]. Freytes et al. showed different sterilization methods, including ethylene oxide, gamma irradiation, and electron beam irradiation, all had effects on the observed

structural properties of the pig bladder ECM. Ethylene oxide had the least effect on properties, while gamma and electron beam irradiation decreased uniaxial and biaxial strength, maximum tangential stiffness, and energy dissipation [44]. Rosario et al. decellularized and sterilized pig bladders for uniaxial mechanical testing and found sterilization with ethylene oxide resulted in stiffening of the ECM [45]. Bolland et al. ran uniaxial tensile tests on decellularized porcine bladder strips and found no decrease in ultimate tensile strength, but a decrease in extensibility compared to native tissue [46]. Farhat et al. compared the mechanical properties of decellularized and intact porcine bladder and found no difference in stiffness (i.e., force vs strain), but a significant increase in elastic modulus (i.e., stress vs strain) for the decellularized tissue. They concluded that the increase in elastic modulus is due to the decrease in the cross-sectional area of the samples after decellularization, and not a change in mechanical response of the tissue [47]. Dahms et al. developed bladder ECM grafts for rats, pigs, and humans, which were tested in tension and compared to native tissue. Results showed that the bladder ECM grafts behaved similarly mechanically to the native tissue, and that pig and human tissue showed higher levels of type III collagen and elastin, whereas rats showed higher levels of type I collagen [48]. Gilbert et al. looked at fiber alignment and biaxial mechanical behavior of pig bladder ECM layers. The submucosa was scraped in either longitudinal or circumferential direction, and observed fiber alignment was skewed towards direction of scraping. Longer toe-regions and lower modulus were present in the submucosa, and samples were generally stiffer longitudinally than in the transverse direction [13]. Liu et al. tested tissue ECM from pig small intestine, urinary bladder, skin, gallbladder, and pericardium. The bladder ECM showed better water uptake, anti-biodegradation, antimicrobial activity, and stem cell attachment when compared to the ECMs of other tissues, and showed high levels of both elasticity and strength [49].

Some studies have assessed tissue engineered bladder grafts after surgical implementation. Brown et al. performed anterior bladder cystectomy and bladder reconstruction on pigs using pig bladder ECM allografts. Results showed extensive cellular repopulation, but lack of smooth muscle bundles and urothelium. Collagen amount and organization was different in the graft region, as well as the rupture strain and elastic modulus from uniaxial tensile tests of the graft region compared to the native tissue region [50]. Oberpenning et al. created bladder neo-organs from dog urothelial and smooth muscle cells seeded onto bladder-shaped polymers. Dog bladders were removed and replaced with the neo-organs, and showed normal capacity, elastic properties, and histological architecture after 11 months [51].

1.2.2.4. *Ex vivo* human studies

As previously stated, human data is hard to come by, largely due to the difficulty of obtaining tissue. However, several studies have been conducted where mechanical testing of human bladder tissue was performed. Rubod et al. performed uniaxial tensile tests on the bladder, vagina, and rectum obtained from human cadavers and found the bladder to be the least rigid tissue, and saw a Mullins effect as a result of straining the tissue [52]. Mullins effect is the dependence of the stress-strain curve on the previous maximum strain when performing cyclical tests with increasing strain. Chantereau et al. ran uniaxial tensile tests on pelvic floor ligaments and organs from young and old human cadavers and found the bladder to be more compliant than the rectum, vagina, and ligaments. Additionally, bladders from the old group were stiffer in the low stress range than the young group [53]. As described in the previous section, Dahms et al. compared rat human and pig intact bladder and bladder ECM and found bladder ECM to behave similarly to native bladder tissue, and human tissue to have the highest levels of elastin and type III collagen [48]. Ewalt et al. used immunohistochemistry to image collagen and elastin in normal-compliance (patients with

vesicoureteral reflux, or obstructive megaureter) and noncompliant (patients with myelodysplasia, neurogenic bladder, or extrophy) human bladders and found no change in fiber content in the lamina propria, but large increase in collagen and elastin in the detrusor with noncompliant bladders, suggesting that stiffening of the detrusor prevents unfolding of the lamina propria, and thus prevents the usual high compliance seen in healthy bladders [54]. Finally, Martins et al. ran uniaxial tensile tests on female human bladders and found bladder stiffness to decrease with age, but neither stiffness nor maximum stress was correlated with body mass index nor menopausal status [55].

1.3. Viscoelastic modeling

Generally speaking, viscoelastic constitutive models of the bladder are presented along with experimental data. The most common constitutive model that will be seen in the following sections is the Maxwell-Wiechert model. This model incorporates a linear spring in parallel with Maxwell elements, represented by a series combination of a linear spring and a damper. **Figure 1.9** shows a Maxwell-Wiechert model with two Maxwell elements. For n number of Maxwell elements, the relaxation function, $G(t)$, takes the following form,

$$G(t) = E_0 + \sum_{i=1}^n E_i e^{-\tau_i t} \quad (1.2)$$

where G has dimensions of stress and is a function of time t , E_0 is the spring constant of the standalone spring, E_i is the spring constant for the i -th Maxwell element, τ_i is the time constant of the i -th Maxwell element, defined by E_i/η_i , where η_i is the viscous damper constant, and n is the total number of Maxwell elements. The Maxwell-Wiechert model can be generalized for an effectively infinite number of Maxwell elements, where E_i is a function of γ_i , defined by a chosen

probability density function (PDF). This type of model will be described in greater detail in a later Section.

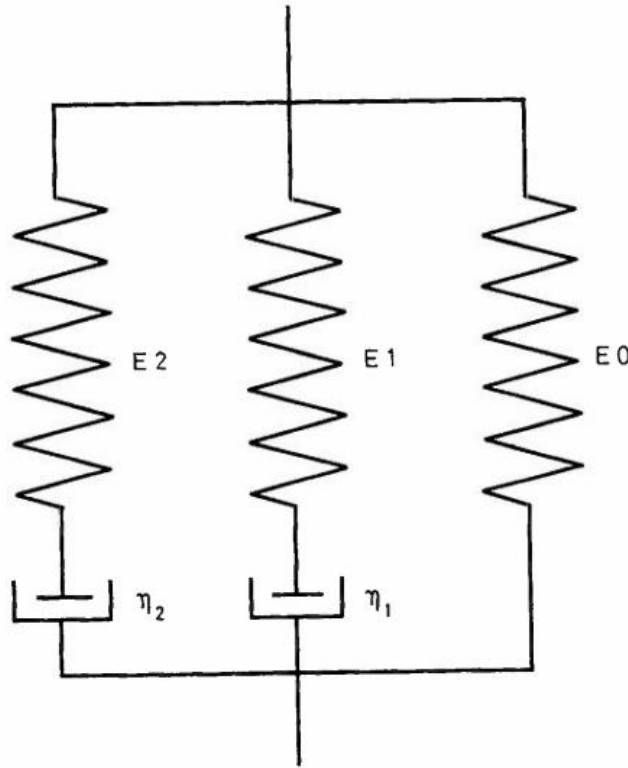


Figure 1.9 Maxwell-Wiechert viscoelastic model with two Maxwell elements [56].

1.3.1. Animal models of health and disease

1.3.1.1. Models informed by data collected *in vivo*

In this section, *in vivo* viscoelastic constitutive modeling studies based on data collected from bladder tissue from animal models are described. Coolsaet et al. used *in vivo* stepwise cystometry of dogs' bladder to quantify the tissue's viscoelastic response. A Maxwell-Wiechert model with 2 Maxwell elements was fit to the pressure-time data. Results showed that clinical cystometry fill rates are too rapid to accurately measure the relaxed response of the bladder [56]. Venegas used small-amplitude oscillatory perturbations to measure the *in vivo* active and passive viscoelastic properties of dog bladders. These experiments are similar to DMA, but use cystometric volume

and pressure, as opposed to tensile strain and stress. Three configurations of singular spring-damper-mass systems, where spring and damper constants increase linearly with force, were used. The only model configuration that correctly described the observed tissue behavior was elastic and viscous components in series, with mass in parallel [57,58].

1.3.1.2. Models informed by data collected *in vitro*

In this section, *in vitro* viscoelastic constitutive modeling studies based on data collected from bladder tissue from animal models are described. Glerum et al. ran uniaxial stress-relaxation tests, consisting of multiple approximately step-wise elongations, on single pig detrusor cells. The peak forces (i.e., immediately following step-wise elongations) appeared to be linearly dependent on the applied elongation. While being held at constant elongation, an exponential decay of force (i.e., relaxation) with respect to time was seen. An exponential function, identical to the output from a Maxwell-Wiechert model with one Maxwell element, was fit to the data. Elastic modulus and relaxation times were found to be different between isolated SMCs and intact tissue [59]. These results could support the idea that, for a Maxwell-Wiechert model with multiple Maxwell elements, each element could correspond to the relaxation times of specific tissue constituents. Mastrigt & Nagtegaal ran stress-relaxation experiments at different strain rates on pig bladder strips. A Maxwell-Wiechert model with 3 Maxwell elements, consisting of nonlinear spring and dashpot elements, was used to fit the data. Parameters were found to depend on strain rate. Authors developed a relation to predict the change in stress-time response based on applied strain rate [60]. This relation could prove useful when comparing stress-relaxation data from experiments with different protocols. Alexander ran creep experiments on rat bladders and found time constants ranging from 186 seconds to 6 hours. *Ex vivo* cystometric experiments were then performed on rat bladders at fill rates slow enough to assume negligible viscoelasticity based on the observed time

constants from previous experiments. Significant hysteresis is seen at all of the tested fill rates, suggesting that visco-plastic models are better suited for modeling the mechanical response of the bladder than viscoelastic models [61]. Nagatomi et al. used a quasi-linear viscoelastic (QLV) reduced relaxation function to fit biaxial stress-relaxation data from SCI rat bladders. The reduced relaxation function, $G(t)$, is as follows,

$$G(t) = \frac{1 + c \left[E\left(\frac{t}{\tau_2}\right) - E\left(\frac{t}{\tau_1}\right) \right]}{1 + c \ln\left(\frac{\tau_2}{\tau_1}\right)}, \quad (1.3)$$

where c is the index for overall relaxation, τ_1 and τ_2 are the beginning and end of the linear portion of the relaxation spectrum, and E is the exponential integral function. Results showed slower relaxation in SCI bladders when compared to controls, and biochemical assays showed decreased collagen content and increased elastin content in SCI bladders compared to controls [21]. Nagatomi et al. used a QLV reduced relaxation function defined by a continuous relaxation spectrum of the following form

$$G(t) = \frac{1 + \int_0^\infty S(\tau) e^{-\frac{t}{\tau}} d\tau}{1 + \int_0^\infty S(\tau) d\tau}, \quad (1.4)$$

where $S(\tau)$ is the continuous relaxation spectrum defined as a bimodal log-scale normal distribution for the ECM, and inversely proportional to τ for smooth muscle cells. Fitting this equation to normal and SCI rat bladder biaxial stress-relaxation data at different initial stress values showed the initial stress level had no impact on the relaxation response, and that SCI rat bladders showed significantly less relaxation than controls [62].

1.3.1.3. Models informed by data collected both *in vivo* & *in vitro*

In this section, we describe viscoelastic constitutive modeling studies based on data collected both *in vivo* and *in vitro* from tissues for animal models. Mastriigt et al. present a model that incorporates

a viscoelastic portion (Maxwell-Weichert model with 3 Maxwell elements), a hyperelastic portion (exponential function), and a plastic element. The model provided good fits to pseudostatic cystometric data from pigs and dogs [11]. Kondo & Susset ran whole organ *in vivo* and *in vitro* stress relaxation experiments on dog bladders using intermittent cystometry. A modified Maxwell-Wiechert model with 3 Maxwell elements (2 with delayed engagement) was fit to the stress relaxation data. Results showed that the elastic behavior of the bladder is much more prominent during *in vitro* experiments when compared to *in vivo* [63]. Coolsaet et al. ran step-wise cystometry experiments on mongrel dogs *in vivo* under anesthesia, and dog cadavers, as well as *in vitro* with intact bladders and bladder strips. Viscoelastic response was fit with a Maxwell-Weichert model with 2 Maxwell elements. Time constants (i.e., ratio of model parameters) appeared to be independent injected bladder volume, but model parameters varied depending on injected bladder volume, suggesting a nonlinear viscoelastic model is likely needed to fully capture tissue behavior [64]. Alexander ran pressure mediated cystometric tests *in vivo* on cat bladders, and *in vitro* on rat, rabbit and kitten whole bladders, as well as uniaxial stress-relaxation tests on rat bladder strips. Using observations on tissue behavior from experimental data, a model was developed that incorporated viscoelastic, plasto-elastic, and irreversible creep elements. *In vivo* experiments showed that while keeping the bladder at high levels of pressure for extended periods of time, irreversible creep of bladder circumference was seen, even after allowing for an 8 hour recovery period at low pressure for the animal [65].

1.3.2. Human models of health and disease

1.3.2.1. Models informed by data collected *in vitro*

In this section, *in vitro* viscoelastic constitutive modeling studies based on data collected from human tissue are described. Susset & Reignier separated the mucosa from the detrusor in human

bladder tissue and conducted stress-relaxation experiments. A Maxwell-Weichert model with 3 Maxwell elements in series with a plastic element was used to model the viscoelastic behavior of the samples. Results showed that the viscoelastic coefficients of the mucosa were markedly higher than that of the detrusor [66]. Van Duyl proposed a viscoelastic/plastic model for both passive and active bladder wall mechanics which includes elastic springs and viscous dampers along with plastic and contractile elements. Two model configurations are proposed. The first is a Maxwell-Weichert model in series with a plastic/contractile element, and the second is a Maxwell-Weichert model with a plastic/contractile element in series with the standalone spring but in parallel with the Maxwell elements. The models are not fit to data and thus no prediction of which model more accurately depict tissue behavior is made [67].

1.3.2.2. Models informed by data collected both *in vivo* and *in vitro*

In this section, viscoelastic constitutive modeling studies based on data collected from human tissue both *in vivo* and *in vitro* are described. Mastriqt et al. evaluated the viscoelastic response of human bladder tissue using *in vivo* stepwise cystometry in living patients, and *in vitro* stress-relaxation of bladder strips obtained from children when the bladder needed to be “opened.” Data was fit with the Maxwell representation of the standard linear solid model, as well as a Maxwell-Weichert model with 3 Maxwell elements [68]. When compared to previously published data [11], human bladders were found to be stiffer than pig bladders, but showed similar viscoelastic constants compared to pigs and dogs [68].

1.4. Hyperelastic modeling

Hyperelastic constitutive models are useful to describe the behavior of the bladder wall when the loading can be considered slow enough to make viscoelastic effects negligible. Many studies that

use hyperelastic models are interested in the mechanical behavior of the bladder at or near physiological fill rates. This can be done through cystometry, or approximating a strain rate that mimics physiological fill rates.

1.4.1. Continuum/exponential models

In this section, we describe hyperelastic continuum constitutive models employed to describe the mechanics of the bladder. Mastrigt and Griffiths looked at active mechanical properties of complete pig bladders and modeled the active response with a classical hill equation and the passive response as depending exponentially on tissue extension [69]. Mastrigt evaluated active and passive mechanical response of pig bladder strips and fit the force-velocity response with a hyperbolic hill equation. Results showed that active bladder pressure decreased with increasing exit flow rate [70]. Reignier et al. used *in vivo* cystometry and *in vitro* uniaxial tensile tests in dog bladders to evaluate the mechanical response of the bladder during filling. The following strain energy function, W , was derived from finite strain theory for hollow spherical structures and used to fit the experimental data

$$W(\lambda, \lambda, \lambda^{-2}) = \int_1^\lambda (\lambda^3 - 1) \frac{dP(\lambda)}{d\lambda} d\lambda, \quad (1.5)$$

$$P(\lambda) = P_0 e^{a(\lambda-1)}, \quad (1.6)$$

$$W = \frac{3P_0(a^2 - 2a + 2)}{a^3} + P_0 \left(\lambda^3 - \frac{3\lambda^2}{a} + \frac{6\lambda}{a^2} - \frac{6}{a^3} - 1 \right) e^{a(\lambda-1)}, \quad (1.7)$$

where λ is the spherical stretch, P_0 is the initial intravesical pressure and a is the rate of exponential increase in pressure during bladder filling. Results showed that the bladder behaves markedly different than rubber balloons [71]. Cheng et al. modeled the loading curves for biaxial tensile testing of rat bladders by assuming an incompressible, isotropic, hyperelastic material with the following Cauchy stress tensor \mathbf{T} .

$$\mathbf{T} = -p\mathbf{I} + \mu e^{\gamma(I_1-3)}\mathbf{B} \quad (1.8)$$

Where p is the Lagrange multiplier used to enforce incompressibility, $I_1 = \text{tr}(\mathbf{B})$ is the first invariant of the left Cauchy-Green deformation tensor $\mathbf{B} = \mathbf{F}\mathbf{F}^T$ and \mathbf{F} is the deformation gradient, μ is the shear modulus, and γ controls the exponential dependence on I_1 . Model fitting in conjunction with imaging led to the conclusions that large bladder distensibility is due to folds in the wall, and distensibility decreases with age due to premature recruitment of fibers on the outer wall [9]. Damaser proposed two models for analyzing the effect of increased bladder mass as a result of urethral outlet obstruction. The first model assumes no change in the zero-pressure capacity of the bladder, and is given by the following equation,

$$\sigma = A\lambda^\alpha + B\lambda^\beta + Q(\rho) \quad (1.9)$$

where A , B , α , and β are constitutive parameters, and $Q(\rho)$ represents the change in wall stress that depends on radial position, ρ , within the bladder wall. The second model assumes that mass and zero-pressure capacity increase proportionally, and is given by the following equation,

$$\sigma = A_1(\lambda^{a_1} - \lambda^{-2a_1}) + A_2(\lambda^{a_2} - \lambda^{-2a_2}) \quad (1.10)$$

where A_1 , A_2 , a_1 , and a_2 are constitutive parameters. The first model predicts increased pressure and decreased compliance, consistent with experiments on animals with mild urethral outlet obstruction. The second model predicts unchanged pressures, but increased compliance and capacity, consistent with experiments on animals with severe urethral outlet obstruction [72]. Watanabe et al. applied the following hyperelastic strain energy function, previously used for rubber, to uniaxially deformed dog bladder and modeled bladder filling as a thin walled sphere,

$$W = w(\lambda_1) + w(\lambda_2) + w\left(\frac{1}{\lambda_1\lambda_2}\right) \quad (1.11)$$

$$w(\lambda_i) = Kn|\lambda - 1|^n \quad (1.12)$$

where K and n are material parameters. Model results show a relatively constant pressure while wall stress increases. This suggests that the ability of the bladder to maintain low pressures during filling is due to geometry and material properties, rather than reflex inhibitory relaxation [73]. Habteyes et al. used the Watanabe and Ogden hyperelastic models to fit uniaxial tensile data from rabbit bladders. Results indicated that acute changes in bladder elasticity could change wall tension and lead to urgency [74].

Korkmaz and Rogg used a model for predicting the stress-stretch response of the bladder without the need for a material model by assuming the shape to be a sphere, and using previously published data to make assumptions on the volume, radius, and pressure differential between the inner and outer wall [75]. A similar approach was previously used by Damaser and Lehman to determine the effect of bladder shape on filling mechanics. Results showed that an oblate spheroid is more compliant than a sphere or prolate spheroid. **Figure 1.10** shows cystometric pressure-volume data, along with model fit to the data for prolate and oblate spheroids with varying eccentricities [76].

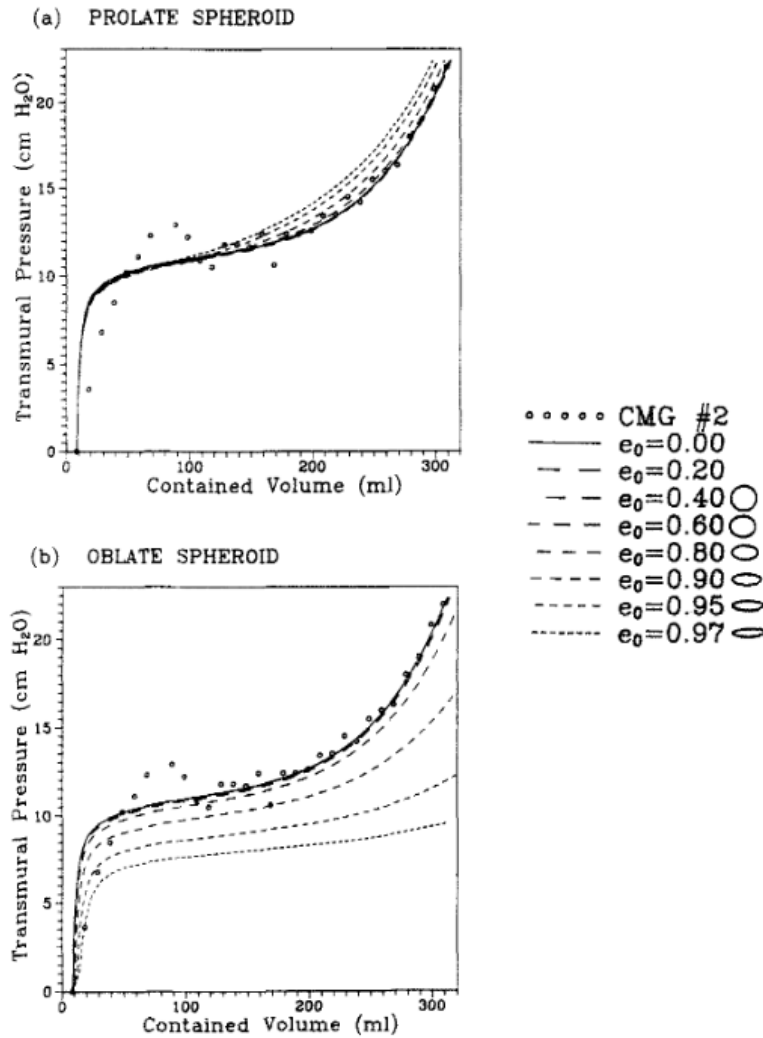


Figure 1.10 Pressure-volume cystometric data from dogs, along with pressure-volume predictions for (a) prolate, and (b) oblate spheroidal bladder models with varying eccentricities [76].

1.4.2. Fiber recruitment models

It is commonly accepted that collagen fibers in tissues, including the bladder, are highly wavy, or coiled, and the compliance of a tissue is heavily influence by the degree of waviness of these fibers. Therefore, it is important to be able to directly view and measure the waviness of fibers, and to create structurally motivated constitutive models that take this waviness into account. The following sections will describe the quantification of collagen fiber waviness and the constitutive modeling of fiber recruitment.

1.4.2.1. Quantification of fiber waviness

Collagen fiber waviness and/or recruitment during tissue loading has been studied in various tissues including rat tail tendon [77], rabbit achilles tendons [78,79], human skin [80], human vena cava [81], pig coronary adventitia [82], rabbit carotid arteries [83,84], and pig thoracic aortas [85]. Chang et al. used immunohistochemistry and confocal microscopy to image fetal bovine bladders and found that the high compliance in the bladder is due to tightly coiled collagen fibers [86]. Cheng et al. was able to measure collagen fiber waviness at different amounts of strain by tracing fibers from images taken from a custom biaxial tensile testing setup that is compatible with a multiphoton microscope. As previously stated, results of this work showed that distensibility was decreased in samples that showed premature recruitment of fibers on the outer wall of the bladder, which seemed to be correlated with aging.

1.4.2.2. Fiber recruitment model structural theory

Lanir developed the structural theory for fiber recruitment and orientation distributions for fibrous tissues [87,88] and later incorporated fiber recruitment in a growth and remodeling model [89]. For tissues with low density of cross-links and wavy collagen fibers, an abbreviated structural theory of fiber recruitment models is as follows. It is assumed that individual elastin and collagen fibers are linearly elastic in tension, and are oriented with angular distributions, $R_e(\theta)$ and $R_c(\theta)$. Elastin fibers are assumed be straight in the unloaded configuration, while collagen fibers are wavy. Collagen fiber waviness follows a probability density function, $P(\lambda_s)$, where λ_s is the stretch it takes to straighten a given fiber. The force as a function of stretch for elastin and collagen fibers are, respectively,

$$F_e(\theta) = K_1[\lambda(\theta) - 1] \quad (1.13)$$

$$F_c(\theta) = K_2 \int_1^{\lambda(\theta)} \frac{P(x)[\lambda(\theta) - x]}{x} dx \quad (1.14)$$

where K_1 and K_2 are the elastin and collagen fiber elastic constants, and $\lambda(\theta)$ is the stretch of a fiber based on applied deformation and fiber orientation, θ . The strain energy function for this material is therefore,

$$W(\lambda, \theta) = \frac{K_1 R_e(\theta)[\lambda(\theta) - 1]}{\lambda(\theta)} + \frac{K_2 R_c(\theta)}{\lambda(\theta)} \int_1^{\lambda(\theta)} \frac{P(x)[\lambda(\theta) - x]}{x} dx \quad (1.15)$$

Since this formulation, collagen fiber recruitment models have been used for various tissues including, but not limited to, rat carotid arteries [90], rabbit carotid arteries [83], [91], rabbit skin [92], and sheep digital tendon [93,94].

1.4.2.3. Fiber recruitment models of the bladder

Collagen fiber recruitment has been quantified and modeled previously in the bladder. Robertson et al. was able to measure the recruitment of collagen fibers in various layers of the rat bladder at different levels of stretch using multiphoton microscopy [9]. Wognum et al. used a fiber recruitment model that assumed a bimodal beta distribution of collagen fiber recruitment during biaxial loading of rat bladders, and found evidence that *de novo* elastin fibers in the SCI rat bladder may play a role in crimping the collagen fiber network, thus changing the recruitment distribution and resulting mechanical properties [14].

1.5 Objectives of this dissertation

The information gathered from this literature review highlight areas in the field of bladder mechanics where further research is needed. Thus, the objectives of this dissertation are the following.

1. Understand the healthy mechanical behavior of the human bladder, and analyze the validity of the pig bladder as a model of the human bladder. This is done by comparing the response of human and pig bladder mechanical behavior tested under identical conditions. Due to high variability in tensile testing protocols and tissue conditions, no previous studies adequately compare the mechanical response of the bladder between humans and pigs.
2. Determine how pathological conditions can alter the stress in the bladder wall. This is accomplished by evaluating the changes in viscoelastic response of the porcine bladder at various states of swelling to gain insight into the effects of degradation of the urothelium and/or acute inflammation. Urothelial degradation and/or acute inflammation may lead to osmotic swelling of the bladder wall, and may alter the stress state of cells and act as a driving force behind remodeling.
3. Evaluate the remodeling of the bladder wall under long-term pathological conditions. This is facilitated by mechanical testing and imaging of the long-term SCI rat bladder ECM. It has been hypothesized that the mechanical response of the SCI rat bladder may return to normal levels of compliance or result in hypocompliance for recovery times greater than 10 weeks [31].

CHAPTER 2 - DIRECT COMPARISON OF HEALTHY HUMAN AND PIG BLADDER TISSUE MECHANICAL PROPERTIES

The results in this chapter are presented in [95].

2.1. Overview

Efforts to understand bladder mechanics in humans have been limited by access to human tissue [48,68,96,97] and restricted largely to in vivo measurements in awake humans, which limits the ability to apply controlled manipulations. Ex vivo studies on the mechanical properties of bladder tissue have been primarily performed on animals. Large discrepancies exist in the mechanical behavior of bladder tissue reported in literature, even within the same species. This is likely due to the differences in testing and tissue preparation protocols between different studies. These differences make it challenging to meaningfully compare mechanical behavior, across species and across pathologies. Additionally, there has not been a direct experimental comparison between pig and human fresh bladder tissue mechanical behavior to evaluate the appropriateness of the pig as a model for the human bladder. To date, the only study comparing human and non-human bladders tested under similar, but not identical, conditions suggests comparable mechanical behavior across pig, dog, and human samples, but the analysis of differences in stiffness was inconclusive [68]. Further, no structural foundation for the observed differences is explored.

Here we present the first direct comparison of healthy human and pig bladder tissue mechanically tested under identical conditions. Moreover, constitutive modeling is used to isolate the contribution of isotropic components (i.e., ground matrix, elastin, and low-stress response of smooth muscle cells) and orthotropic components (i.e., collagen fibers and high-stress response of smooth muscle cells) to the overall mechanical behavior of the tissue. We tested the effect of two

treatments on tissue mechanical properties. Namely, elastase to digest elastin fibers, and oxybutynin to reduce smooth muscle cell spasticity. We implemented two different material models to aid in the interpretation of the experimental results. We found that human tissue behaves similarly to pig tissue at high deformations (collagen-dominated behavior) while we detected differences between the species at low deformations (amorphous matrix-dominated behavior). Our results also suggest that elastin could play a role in determining the behavior of the fiber network. Finally, we confirmed the anisotropy of the tissue, which reached higher stresses in the transverse direction when compared to the longitudinal direction. This work establishes a framework for the development of future models to describe fibrotic/dysfunctional bladders as well as to aid in the development of tissue engineering solutions for this complex and remarkable organ.

2.2. Methods

All tissue preparation and mechanical testing was performed by Duncan Morhardt in Ellen Arruda's laboratory at the University of Michigan (Ann Arbor, Michigan). All constitutive modeling was performed by Tyler Tuttle in Sara Roccabianca's laboratory at Michigan State University (East Lansing, Michigan).

2.2.1. Tissue preparation

Bladders from six female Yorkshire pigs (6-9 months old) were harvested at the time of sacrifice and transported to the lab at 25-30°C in calcium-free and magnesium-free phosphate buffered saline (PBS) pH 7.4 (Gibco), based on [98]. Human bladders (n=4) were obtained at time of organ transplant procurement and transported similarly. Age, sex, and cause of death for human donors are provided in Table 2.1. Testing commenced within 12 hours of procurement. Tissue was kept at 37°C until specimen preparation. The bladder was divided just above the trigone leaving the

dome, and cut along the anterior surface and dome to allow flat preparation while maintaining the longitudinal and transverse orientations (see **Figure 2.1**). A stainless-steel die was used to create dumbbell-shaped specimens by cutting from the urothelium to the serosa. Samples were collected from both the longitudinal and transverse orientations (longitudinal samples identified with a superscript $f = 1$, and transverse samples with $f = 2$ moving forward). Most bladders provided 6-8 specimens, specifically we collected and tested 22 longitudinal tissue samples from pig and 13 from human, and 12 transverse tissue samples from pig and 3 from human. The individual specimens were transferred to separate wells and maintained at 37°C until testing.

A subset of samples was treated with elastase an enzyme that degrades elastin fibers (4 from pig and 3 from human tissue). Samples were treated with 200 units of elastase (Worthington, NJ) for three hours (following what was reported in [98]), but with this concentration the overall specimens' structure was compromised and mechanical testing was not possible. When treated with 50 units of elastase for the same treatment time, the samples maintained enough tissue consistency to withstand testing and elastin was significantly degraded (elastin loss was confirmed by histology). Another subset of samples was treated with oxybutynin, an anticholinergic drug that reduces spasticity in muscle cells (11 from pig and 5 from human tissue, in addition 3 samples from pig tissue where treated with both oxybutynin and elastase). We used a concentration of 150µM oxybutynin (Sigma-Aldrich, St Louis, MI), based on *in vitro* studies [99,100]. Samples were randomly allocated into each treatment.

Specimen dimensions were measured with calipers before testing, and were statistically unchanged after treatments. Due to a need to reduce potential contamination of reagents, we tested untreated tissue first, then oxybutynin treated tissue (pharmacologically diluted), and lastly elastase treated

tissue (enzymatic treatment, not dilutable). All tests from the same specimen were performed within three hours of each other.

The tissue procured and experiments performed were deemed exempt by the University of Michigan Institutional Review Board.

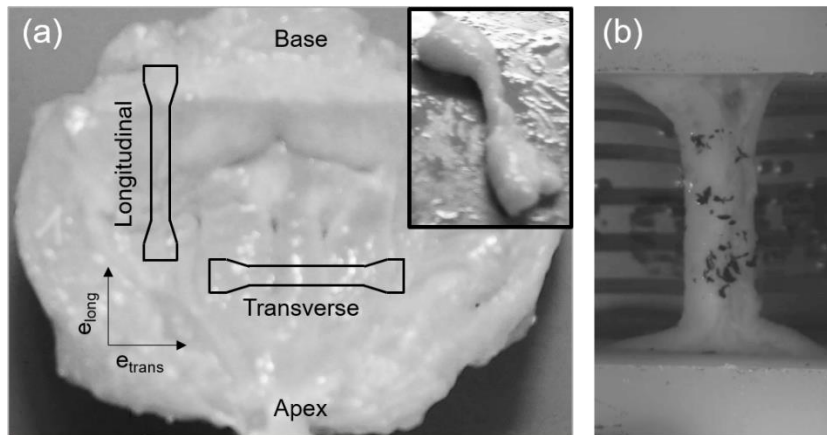


Figure 2.1 *Sample orientation schematic and uniaxial sample preparation.* a) The trigone is removed from whole bladder and a steel die produce dumbbell specimens (inset). Also shown are the transverse and longitudinal directions, as well as schematics of orientations of specimens. b) Pictured is a representative tissue specimen mounted in the uniaxial tester.

Table 2.1 Donor demographic information: age, sex, and cause of death

Donor	Age	Sex	Cause of death
A	25	Male	Head trauma
B	28	Male	Anoxia
C	44	Male	Anoxia
D	51	Female	Anoxia

2.2.2. Mechanical testing

2.2.2.1. Uniaxial testing

Individual specimens were tested on a custom uniaxial tensile loading/unloading device with screw in grips (**Figure 2.1b**). The force was determined with a voltage converting 100mN load cell (World Precision Instruments, Sarasota, FL). The testing bath was maintained at 37°C with a modified temperature controller (Harvard Apparatus, Cambridge, MA). Specimens were floated

into grips to minimize tare load. After placing in grips, the zero-load state was verified by advancing and retracting the grips (± 1 mm) while monitoring the load. The gage length for stretch (nominally 12mm) was determined by this positioning. Specimens were subjected to three load-unload cycles to a maximum stretch of 1.8 (Pull 1, Pull 2, Pull 3, without preconditioning prior) at a rate of 0.01 s^{-1} . The physiologic stretch level is approximated to be equal to 1.8, based on the average stretch experienced by a human bladder containing 400 milliliters of urine. **Figure 2.2** shows a plot of the physiologic loading strain history during testing. A fourth load-unload cycle (Pull 4) was performed on a subset of samples up to a maximum stretch of 2.6 (supraphysiologic loading test, same loading rate).

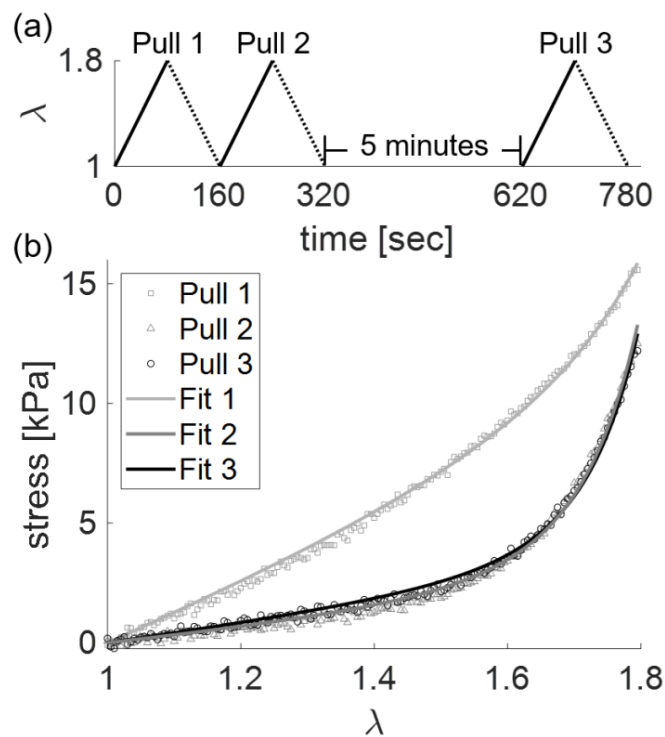


Figure 2.2 Testing protocol for tissue specimens and representative data - model prediction results. a) Stretch versus time graph showing three load-unload cycles and the timing of those cycles, and b) stress versus stretch graph showing loading data (symbols) of a single specimen and its corresponding model prediction curves (lines) for Pulls 1, 2, and 3.

2.2.2.2. Compression testing

Orthogonal tissue specimens were prepared using a six-millimeter biopsy punch and placed in 37°C PBS buffer in a clear chamber in a Dynamic Mechanical Analyzer (TA Instruments RSA-G2). After zeroing at contact, untreated pig samples (n=2) underwent compressive loading up to 0.99 kPa for one sample and 1.9 kPa for the other.

2.2.3. Constitutive modeling

2.2.3.1. Fiber recruitment (M1)

Collagen constitutes the largest extracellular matrix component in the human bladder at approximately 30% of the intact-tissue dry-weight [1–3]. The collagen fiber network significantly contributes to the mechanical behavior of soft tissues and has been previously modeled [101]. Collagen fibers are coiled in the unloaded configuration, but straighten and begin to bear load as the tissue is stretched (**Figure 2.3**). This peculiar behavior has been shown in rat tail tendon [77], rabbit Achilles tendon [78,79], human skin [80], human vena cava [81], pig coronary adventitia [82], rabbit carotid arteries [83,91], pig thoracic aortas [84], and rat bladder [85]. A collagen fiber recruitment model, describing the characteristic uncoiling of collagen fibers and its mechanical consequences, was first developed by Viidik [78], with the corresponding structural theory later described by Lanir [87]. These types of models have been used to describe several soft tissues, including rat carotid arteries [90], rabbit skin [92], rabbit carotid arteries [83,91], sheep digital tendon [93,94], and rat bladder [14].

Here, a fiber recruitment model was used to estimate the recruitment distribution of collagen fibers during uniaxial loading of pig bladder tissue (**Figure 2.4b-d**). For this model, the percentage of recruited collagen fibers is assumed to follow a normal cumulative distribution function (Φ_{cdf}),

$$\Phi_{cdf}(\lambda; \lambda_m, \lambda_{sd}) = \frac{1}{2} \left(\operatorname{erf} \left(\frac{\lambda - \lambda_m}{\sqrt{2}\lambda_{sd}} \right) + 1 \right), \quad (2.1)$$

where λ is the stretch, and λ_m and λ_{sd} are the mean and standard deviation of collagen fiber recruitment stretch, respectively. Individual collagen fibers are assumed to behave linearly in tension once straightened, as previously shown [102,103]. The recruitment distribution of linearly behaving fibers causes the global tissue response (i.e., stress-stretch curve) to behave in a nonlinear fashion. The following differential equation was used to describes uniaxial tensile behavior

$$\frac{d\sigma}{d\lambda} = E_1 \Phi_{cdf}(\lambda; \lambda_m, \lambda_{sd}), \quad (2.2)$$

where σ is stress and E_1 is the slope of the stress-stretch curve when 100% of the collagen fibers are recruited (linear portion of the stress-stretch curve). Limitations of this model are that it ignores the contribution of all tissue components except for collagen fibers, and that it uses the assumption that collagen fibers are only aligned in the direction of the stretch. This model was used as an estimation of fiber recruitment, and was not used as a constitutive description of the bulk of the mechanical data. This model was only applied to Pull 4 (supraphysiologic loading), which was performed on a selected few samples (see 2.2.3.3 *Material parameter estimation* for details).

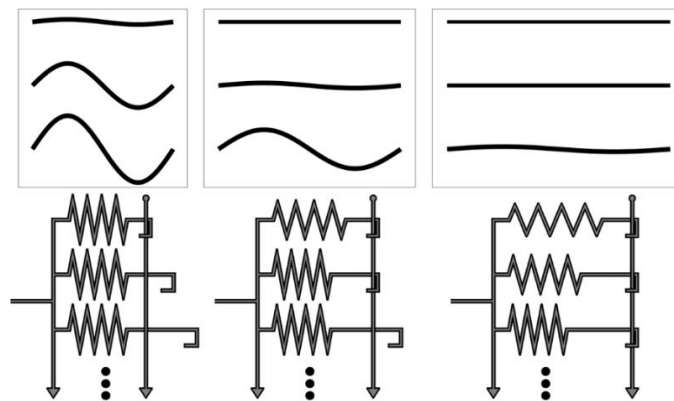


Figure 2.3 *Schematic diagram of collagen recruitment model.* Gradual engagement of collagen fibers (top row) are modeled by spring elements (bottom row). As the model/tissue is stretched (left to right), the hooks engaging the bar is mirrored by the straightening of the collagen fibers, and the stretching of the springs represents the stretching of the individual collagen fibers.

2.2.3.2. Continuum model (M2)

A 2-fiber family nonlinear elastic model (M2), similar to what has been previously described by Roccabianca et al. [104], was used in this study to describe the stress-stretch behavior of the human and pig bladder tissue (**Figure 2.4a**). Given the applied uniaxial stretch, λ , the deformation gradient tensor, \mathbf{F} , and right Cauchy-Green tensor, \mathbf{C} , are defined as follows,

$$\mathbf{F} = \begin{bmatrix} \lambda_1 & 0 & 0 \\ 0 & \lambda_2 & 0 \\ 0 & 0 & \lambda_3 \end{bmatrix}, \mathbf{C} = \mathbf{F}^T \mathbf{F}, \quad (2.3)$$

where $\lambda_1 = \lambda$, and $\lambda_2 = \lambda_3 = 1/\sqrt{\lambda}$ are the principal stretch directions. Using these finite deformation theory descriptions, the strain energy function, W , takes the following form,

$$W(\mathbf{C}) = W^{am}(\mathbf{C}) + \sum_{f=1}^2 W^f(\mathbf{C}), \quad (2.4)$$

where $W^{am}(\mathbf{C})$ is the strain energy function that describes the isotropic behavior of the tissue at low-stress, dominated by amorphous matrix, elastin fibers, and low-stress behavior of muscle cells, and $W^f(\mathbf{C})$ is the strain energy function that describes the orthotropic behavior of the tissue, dominated by collagen fibers but also including the high-stress behavior of smooth muscle cells. The orthotropic components of the tissue are considered to be morphologically organized in two families, defined by the superscript $f = 1, 2$. The isotropic strain energy function is defined as follows,

$$W^{am}(\mathbf{C}) = \frac{c^{am}}{2} (I_1 - 3) \quad (2.5)$$

where c^{am} is the material parameter with the dimension of stress, and $I_1 = tr(\mathbf{C})$ is the first invariant of the right Cauchy-Green deformation tensor. The orthotropic strain energy function is defined as follows,

$$W^f(\mathbf{C}) = \begin{cases} 0, & \lambda^f < 1 \\ \frac{c_1^f}{4c_2^f} \left\{ \exp \left[c_2^f (I_4^f(\mathbf{C}) - 1)^2 \right] - 1 \right\}, & \lambda^f \geq 1 \end{cases} \quad (2.6)$$

where c_1^f and c_2^f are the material parameters for f th fiber family, the first with the dimension of stress and the second dimensionless. The fibers are assumed to fold in compression and provide little to no resistance to deformation. Because the orthotropic behavior is assumed to be dominated by the collagen fiber response, we considered W^f to be zero in compression (i.e., $\lambda^f < 1$), an assumption made in relevant previously published models [105–108]. However, we acknowledge that in bladder tissue there is likely some orthotropic contribution from smooth muscle cell bundles when compressed, which could influence the value of Lagrange multiplier and that may not be captured by the neo-Hookean component. For this reason, the assumption of $W^f = 0$ in compression, while reasonable, represents a limitation of the model. The first and second fiber families are separated by 90° and oriented in the longitudinal and transverse tissue directions, respectively. $I_4^f(\mathbf{C}) = \text{tr}(\mathbf{C}\mathbf{A}^f)$ is the fourth invariant of the right Cauchy-Green tensor, defined in the direction of the f -th fiber family. The undeformed orientation tensor is defined as $\mathbf{A}^f = \mathbf{N}^f \otimes \mathbf{N}^f$ where $\mathbf{N}^f = [\cos(\alpha_f), \sin(\alpha_f), 0]$ is the fiber direction in the undeformed configuration. Here, $\alpha_1 = 0^\circ$ describes the longitudinal fiber family ($f = 1$) and $\alpha_2 = 90^\circ$ describes the transverse fiber family ($f = 2$), as shown in [8]. From the strain energy function, the stress-stretch relationship is obtained as follows

$$\boldsymbol{\sigma} = -p\mathbf{I} + 2\mathbf{F} \frac{\partial W}{\partial \mathbf{C}} \mathbf{F}^T, \quad (2.7)$$

where $\boldsymbol{\sigma}$ is the Cauchy stress, \mathbf{I} is the identity matrix, and p is a Lagrange multiplier that enforces incompressibility. This model was applied to the physiologic loading test curves for every sample in both pigs and humans (see 2.3.3 *Material parameter estimation* for details).

2.2.3.3. Material parameter estimation

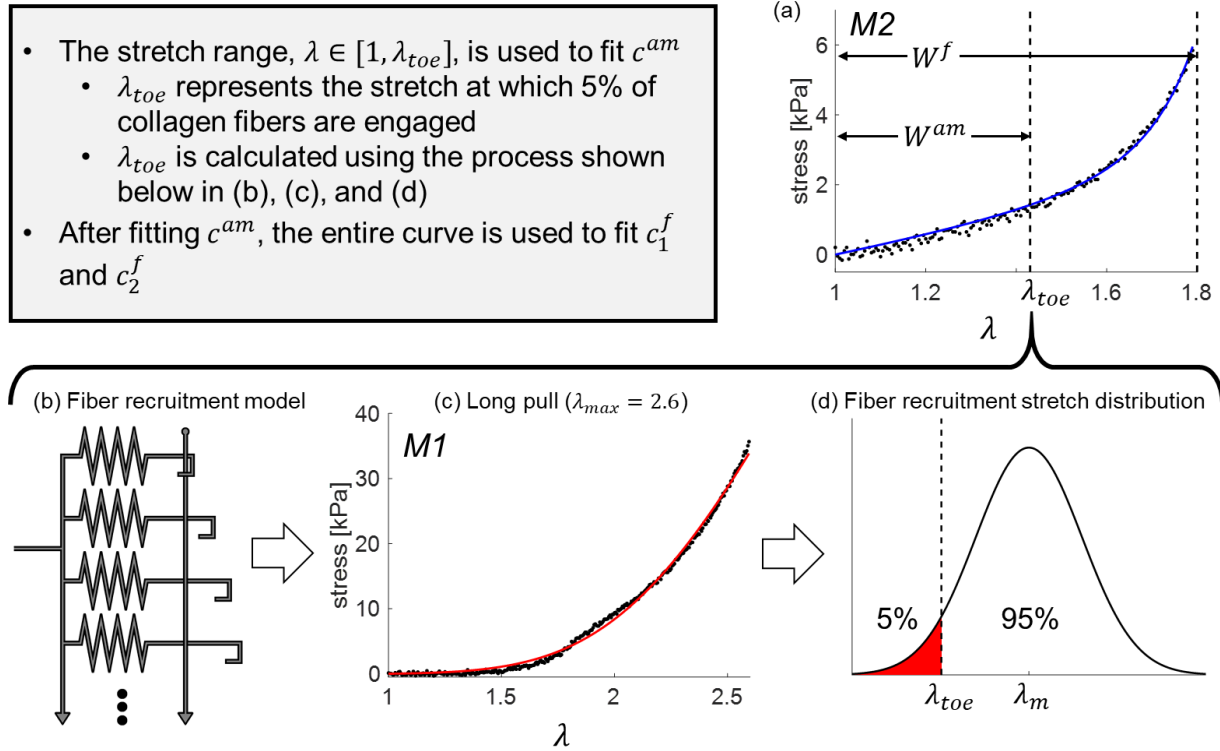
A key feature of the structural model M1 is that the stress-stretch curve will approach a linear relationship as the percentage of recruited fibers approaches 100%. It follows that, to estimate the material parameters with reasonable confidence, the experimental data used to inform model M1 must reach the high-stress, linear portion of the stress-stretch curve. If the stretch applied to the sample during the mechanical testing is not sufficiently large, then uncertainty in parameter estimates for M1 would be high. This prohibits the use of M1 to describe the data from the physiologic loading experiments ($\lambda \in [1, 1.8]$). For this reason, we employed the phenomenological model M2 to describe the physiologic loading data. On the other hand, to confidently estimate the parameter describing the isotropic region in M2, there is a need to define a toe-region of the stress-stretch curve ($\lambda \in [1, \lambda_{toe}]$). The toe-region is defined as the range of stretch where collagen fibers provide negligible resistance and the mechanical behavior is isotropic, dominated by amorphous matrix, elastin, and behavior of smooth muscle cell at low-stress. The model M1 is introduced to calculate a value for λ_{toe} that has structural relevance, as opposed to being arbitrarily chosen. The following paragraphs describe the entire two-steps parameter estimation process in greater detail, starting with (1) using M1 to estimate λ_{toe} , and (2) using λ_{toe} in the parameter estimation process for M2. **Figure 2.4** represents a schematic of the overall parameter estimation process.

The result of the parameter estimation for the model M1 is a cumulative distribution, Φ_{cdf} (Equation 2.1), which represents an estimate of the percentage of fibers that are recruited at a given stretch (supraphysiologic loading data used). Using the cumulative distribution from M1, the toe-region ($\lambda \in [1, \lambda_{toe}]$) was calculated, with λ_{toe} defined as the value of stretch needed to reach 5% of fibers recruited. This method was implemented for data from oxybutynin treated samples (n=2),

elastase treated samples (n=2), and one sample treated with both oxybutynin and elastase (n=1), all of which were from pig tissue in the longitudinal direction. Due to the limited dataset available for the supraphysiologic loading, approximations were made in the definition of toe-region for some groups. Specifically, λ_{toe} calculated for oxybutynin was also used for untreated samples (under the assumption that oxybutynin has the least effect on the configuration of the collagen fiber matrix when compared to elastase), λ_{toe} calculated for pigs was also used for the corresponding treatment groups in humans, and λ_{toe} calculated for the longitudinal direction was also used for the transverse direction for all treatments. This is a limitation of this study.

The parameter estimation process for M2 was divided into two steps. This was done to reduce the number of parameters being calculated simultaneously, which lessens the impact of the correlation between sensitivities of the parameters describing the isotropic and orthotropic behavior. First, the isotropic portion of M2 was used to describe the toe-region of the stress-stretch curves ($\lambda \in [1, \lambda_{toe}]$), resulting in a value for c^{am} (Equation 2.5). Second, using the full form of the model M2 (Equation 2.4) and the estimated c^{am} parameter, the full stress-stretch physiologic loading curve ($\lambda \in [1, 1.8]$) was employed to calculate c_1^f and c_2^f . Specifically, for each sample, we estimated only the set of parameters describing the fibers in the direction of applied stretch. This was a direct result of two hypotheses made in the model: (1) the fiber directions in M2 were defined as parallel and perpendicular to the direction of applied stretch, and (2) the fibers were not contributing to the mechanical behavior in compression (i.e. as shown in Equation 2.6, the strain energy is zero if $\lambda^f < 1$).

In all steps, the nonlinear least squares solver *lsqnonlin* in MATLAB was used for parameter estimation. A sensitivity study was performed with λ_{toe} chosen at 2.5%, 5%, and 10% collagen recruitment. Observed statistical differences were generally conserved across all percentages.



2.2.4. Statistical analysis

Statistical analysis was performed with JMP 14Pro (Cary, NC). Estimated material parameters were compared among treatments, between species, and between tissue orientations. The unit of measurement was pull. Due to the different distributions among groups, Wilcoxon or Kruskal-Wallis were performed with a predetermined $p < 0.05$ to reach significance. The Steel-Dwass test, a nonparametric test for pair-wise comparisons, was employed to further examine differences

among subgroups when Kruskal-Wallis was <0.05 . We performed a MANOVA for repeated measures (with recommended corrections for sphericity) by pull under each condition, direction, and species but cautiously avoided stronger conclusions in these sub-analyses. With similar restrictions, we utilized a least squares model to examine pairwise differences of pulls among different conditions.

2.3. Results

2.3.1. Collagen recruitment model (M1)

We used the data collected for the supraphysiologic loading test protocols ($\lambda \in [1,2.6]$) to estimate the parameters of the M1 model. This resulted in three sets of approximate fibers recruitment distributions, namely $\Phi_{cdf}(\lambda; \lambda_m, \lambda_{sd})$ as defined in Equation 2.1, one for each treatment group. The distribution parameters within each group were averaged, if necessary, and the stretch corresponding to the recruitment of 5% of fibers, λ_{toe} , was estimated for each group to be used in M2 (see Section 2.2.3.3 *Material parameter estimation*). Table 2.2 shows the parameters for the model M1 and the normalized root-mean-square error (NRMSE) for each sample, as well as the value of λ_{toe} for each group. Because of the limited number of supraphysiologic loading protocol samples, no statistical analysis was performed on the M1 parameter values.

Table 2.2 Parameter estimates for M1, NRMSE for each supraphysiologic loading fit, and λ_{toe} representing stretch for 5% collagen recruitment for each group.

Treatment	E_1 [kPa]	λ_m	λ_{sd}	NRMSE	λ_{toe}
elastase	195.73	2.48	0.34	0.020	1.65
elastase	16.35	1.88	0.31	0.031	
oxybutynin	64.84	2.10	0.44	0.016	1.43
oxybutynin	54.76	2.26	0.47	0.016	
oxy/ela	205.55	2.05	0.22	0.006	1.68

2.3.2. Continuum model (M2)

Figure 2.2b shows a set of data for one representative pig sample (3 loading curves) represented by symbols, and the corresponding model estimation for each pull, represented by lines. The average NRMSE for all parameter estimations was 0.046. **Figure 2.5** shows a histogram of NRMSE and standardized concatenated residuals for all curves. Standardized residuals appeared to be normally distributed with a mean of -0.2015. A negative value was expected due to the nature of the additive 2-step parameter estimation process.

Figure 2.6 gives a representation of the stress-stretch response data and M2 model prediction for different pulls, treatments, and direction; data collected in both human (**Figure 2.6a**) and pig (**Figure 2.6b**) tissue. Only groups containing 4 or more samples are shown in the figure, however all estimated material parameters are available in an open source repository as described in the APPENDIX. The mechanical data suggest that, given equal deformation, the transverse direction tends to reach higher stresses than the longitudinal direction for all pulls (data shown only for pigs). The stress-stretch curve for Pull 1 is markedly different than that of both Pull 2 and Pull 3. No differences are observed between Pull 2 and 3, regardless of treatment or direction (supported by top level MANOVA). This suggests sufficient preconditioning after only one load-unload cycle. Similar behavior has been seen in biaxially tested rat bladder, where the second and 12th loading curves were nearly identical [109].

Figure 2.7 shows box plots of parameter estimates for the same groups shown in **Figure 2.6**. For both human and porcine tissue, c^{am} values were higher and $c_2^{1,2}$ values were lower for Pull 1 when compared to Pull 2 and Pull 3. Furthermore, statistical analysis showed c^{am} was not affected by tissue treatment, whereas $c_1^{1,2}$ and $c_2^{1,2}$ were affected by elastase (data available in the *Supplementary Materials*) but not by oxybutynin, for both human and pig tissue. This result was

also supported by the fact that peak stresses at each pull had higher consistency in oxybutynin treated specimens (coefficient of variation 0.09, 0.07, 0.16 for Pulls 1, 2, and 3, respectively) when compared to untreated specimens (coefficient of variation 0.42, 0.37, and 0.38 for Pulls 1, 2, and 3, respectively), in human. In addition, consistent with **Figure 2.6**, each transverse parameter exceeded its longitudinal counterpart. Finally, values for c^{am} tended to be higher in pigs than in humans, across treatments.

Statistical analysis confirmed the differences observed in **Figure 2.7**. Specifically, c^{am} differed little among treatments, whereas it differed significantly by direction ($p < 0.0001$) and by species ($p < 0.001$). Parameter c_1^f differed by direction ($p < 0.0001$) and between human and pig specimens ($p = 0.011$); parameter c_2^f was statistically different between transverse and longitudinal specimens ($p = 0.0043$), however it was similar across treatments and between species. Furthermore, the parameters $c_1^{1,2}$ and $c_2^{1,2}$ differed between oxybutynin and elastase treated specimens ($p < 0.0001$ for $c_1^{1,2}$, $p=0.008$ for $c_2^{1,2}$) and untreated and elastase treated specimens ($p < 0.0001$ for $c_1^{1,2}$, $p=0.005$ for $c_2^{1,2}$), but did not differ between oxybutynin and untreated samples. A strong pull effect was seen in c^{am} by direction ($p=0.0008$) but not by condition ($p=0.55$) or species ($p=0.49$). Similarly, a pull effect was seen in direction for $c_1^{1,2}$ ($p=0.035$) and $c_2^{1,2}$ ($p=0.003$). To aid in the interpretation of these observations, we examined the Cauchy stress at λ_{toe} for each group (**Figure 2.8**). When looking at Pull 1 in humans, oxybutynin treated samples showed higher stresses at λ_{toe} , whereas in pigs, untreated samples showed higher stresses at λ_{toe} ; pigs showed higher stresses at λ_{toe} than humans ($p=0.0028$); samples tested in the transverse direction showed higher stresses at λ_{toe} than those tested in the longitudinal direction ($p=0.0005$, data collected in pigs).

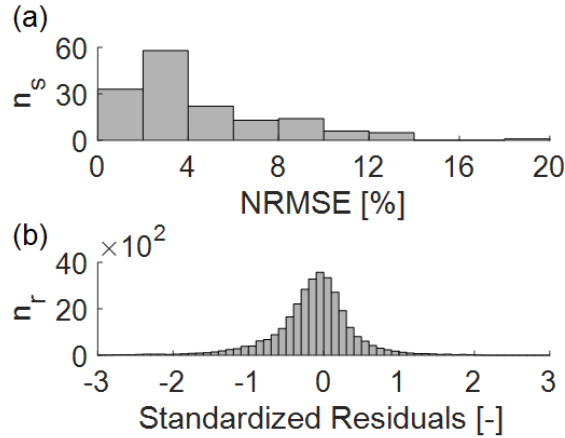


Figure 2.5 Normalized root mean square error (NRMSE) and standardized residuals for all data. Histograms of (a) NRMSE for all fitted curves, where n_c represents number of fitted curves, and (b) standardized residuals for all data points included in the fitting process, where n_r represents number of residuals.

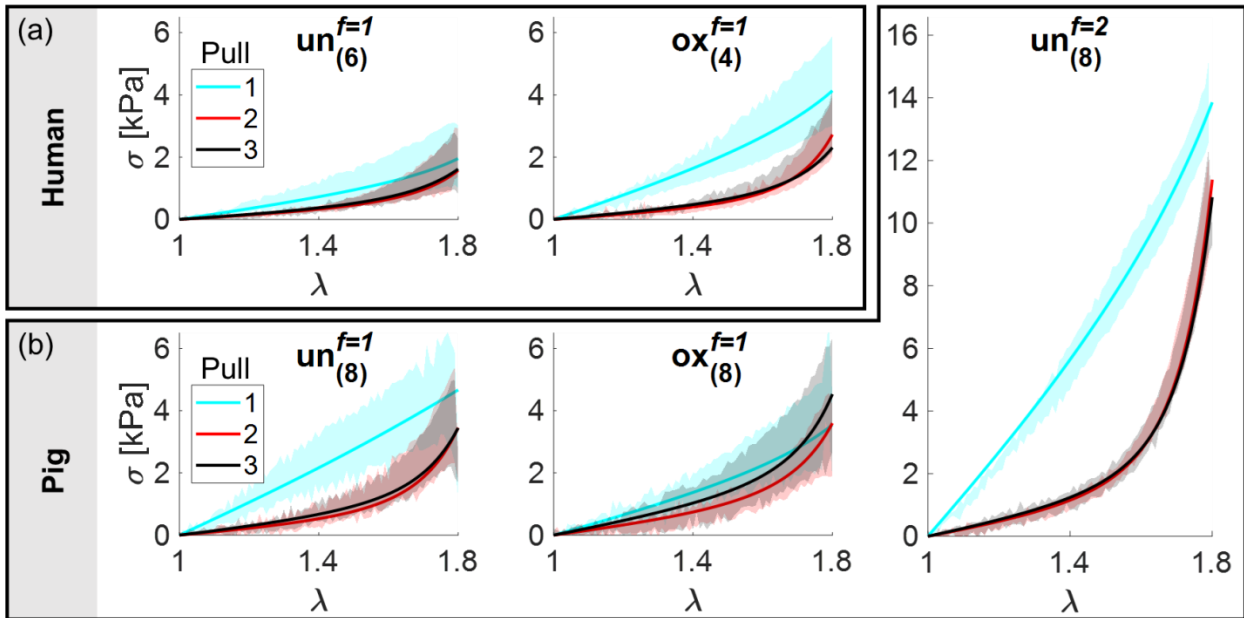


Figure 2.6 Human and porcine fitted curves under different treatment conditions. M2 model output using median parameter values (lines) and interquartile range of experimental data (shaded) for a) untreated (un) and oxybutynin treated (ox) specimens in humans, and b) untreated (un), oxybutynin treated (ox), and untreated transverse (un) specimens in pigs. Plot titles represent treatment, with superscript denoting direction ($f = 1$ for longitudinal, $f = 2$ for transverse), and subscript denoting number of samples. Only groups containing 4 or more samples are shown.

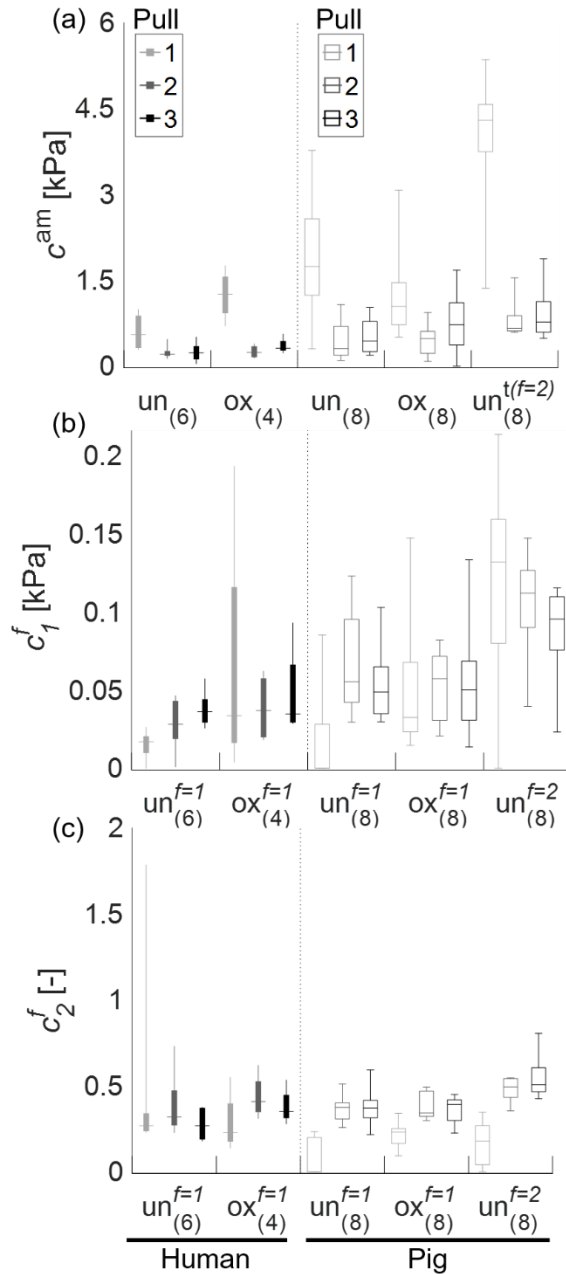


Figure 2.7 *Parameter Estimates*. Estimated values for c^{am} (a), c_1^f (b), c_2^f (c) are displayed in box plots (median line, box first quartile - third quartile, error bar 0th and fourth quartiles). The results shown include parameter values estimated for both humans (left) and pigs (right). Only groups containing 4 or more samples are shown, all parameter estimates can be found in an open source online repository.

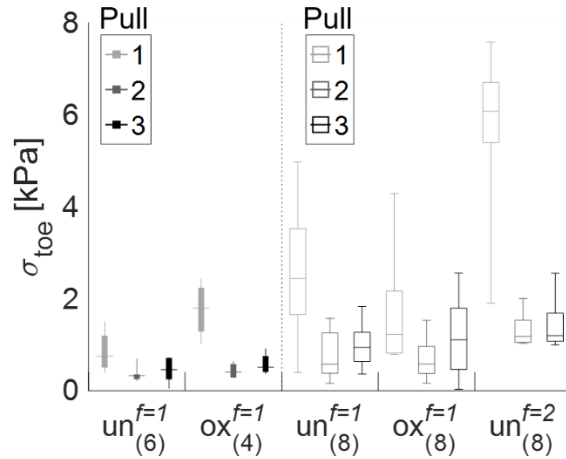


Figure 2.8 *Calculated values of stress at λ_{toe} .* Box plots representing the experimentally recorded stress values at λ_{toe} for humans (left) and pigs (right). Only groups containing 4 or more samples are shown.

2.3.3. Modeling of compression tests

We performed compression studies in the direction normal to the bladder surface in two untreated pig bladder specimens. **Figure 2.9** shows the experimental compression data (testing set) along with the model M2 prediction using median parameter values estimated employing uniaxial tests (training set).

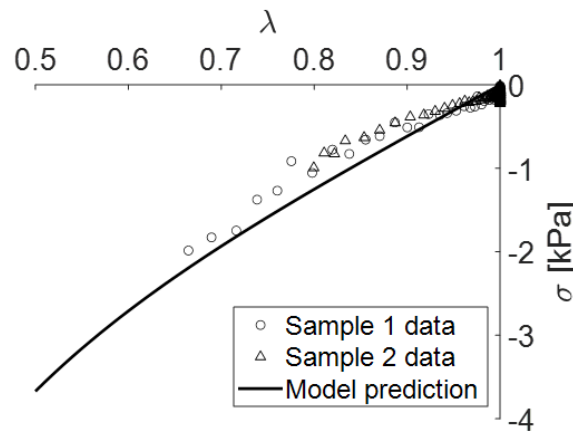


Figure 2.9 *Comparison of compressive behavior experimentally measured and predicted by model M2.* Symbols represent the experimental data from compression tests in untreated pig samples (testing data-set). The line represent the model prediction for a compression test calculated using median parameter values estimated from uniaxial experiments for untreated pig tissue (training data-set).

2.4. Discussion

Pig tissue has provided the standard for comparison with human tissue since [48] suggested that human bladder and pig bladder have the same mechanical properties. Pigs have also been extensively used as a large animal model in the fields of tissue engineering and disease models [110]. This study presents constitutive modeling of fresh human and porcine bladder tested under identical tensile-testing protocols. It includes species-specific mechanical behavior for the bladder wall, including the effect of elastase and oxybutynin treatment and testing direction. In our review, we found no studies that were designed with the purpose of comparing mechanical behavior of fresh human and pig bladder tissue tested under identical conditions or that have compared human and pig collagen microstructure in bladder histology. Thus, to our knowledge, this is the first study which can offer a direct comparison of mechanical parameters describing the fiber network between human and pig tissue. We have also performed a microscopic examination of a limited number of Van Geisen-stained human and porcine sectioned specimens that revealed similar structural elements of muscle, vessels, elastin, and fibrous matrix (**Figure 2.10a**, APPENDIX) supporting our choice of using a combination of fiber-based constitutive models. More in depth quantitative comparison of microstructure from a histological standpoint is necessary to better understand the similarities and differences in these tissues, and represents an important topic for future studies to address.

2.4.1. Validation of model M2 using compression data

To verify the predictive capabilities of the M2 model, stress values were generated for compression using median parameter estimates for Pull 1 from the untreated pig samples and compared to experimental data collected during compression test (**Figure 2.9**). Despite having been optimized with uniaxial tensile data (training data-set), the model predicts quite accurately the experimental

response of the tissue in compression (testing data-set), a deformation mode that is similar to biaxial tension. This gives us confidence in looking at the model parameters to draw conclusions about (1) the contribution of different constituents to the overall behavior of the tissue, and (2) identify possible differences between the different groups analyzed here.

2.4.2. High stress, orthotropic contribution to mechanical behavior

We first focused on isolating the orthotropic contribution to the overall tissue behavior, dominated by the collagen fiber network and by high-stress behavior of smooth muscle cells, by analyzing $c_1^{1,2}$ and $c_2^{1,2}$. We also aimed to interpret the effect of elastase and oxybutynin treatment on tissue behavior. First, there are no significant differences when comparing untreated to oxybutynin treated samples, where oxybutynin is a clinically relevant drug with pharmacological result of reducing spasticity and cholinergic drive [99]. This suggests that smooth muscle cells are engaged passively and have limited spontaneous contractions and residual muscle tone at high stresses, in both humans and pigs. Moreover, the differences we observed in $c_1^{1,2}$ and $c_2^{1,2}$ between elastase treated specimens and both oxybutynin treated and untreated specimens, suggest a change in the engagement of collagen fibers as a result of elastin loss, which is potentially independent of smooth muscle cell engagement on the extracellular matrix. Taken together, these results suggest that elastin could play a role in altering the mechanical response of the collagen fiber network by affecting its waviness and, ultimately, its recruitment. These conclusions support previous reports in the spinal cord injured rat bladder, where *de novo* elastin fibers were thought to increase crimp of the collagen fiber network and consequently increase compliance of the tissue [14]. Interestingly, we do observe differences between untreated and oxybutynin treated samples when comparing the Cauchy stress evaluated at λ_{toe} for Pull 1, which results in higher stresses for

oxybutynin treatment in humans compared to pigs. This result could have been affected, however, by the use of the same λ_{toe} values for both untreated and oxybutynin treated samples.

2.4.3. Species-specific mechanical behavior

We observed species-specific differences for the material parameter c^{am} , and for parameter c_1^1 (differences for c_1^1 had low statistical relevance), while c_2^1 was independent of the species. Furthermore, porcine samples seemed to reach higher stresses at λ_{toe} . These results suggest that the differences in mechanical behavior of the tissue between species stems primarily from dissimilarities in the elements contributing to the low-stress, isotropic behavior, such as elastin, amorphous matrix, and low-stress behavior of smooth muscle cells. The lack of differences in collagen network parameters supports the use of porcine bladder extracellular matrix as a viable scaffold material for tissue engineering of the human bladder, as suggested in previous studies [45,46,111].

2.4.4. Porcine tissue anisotropy

A difference in both the material parameter c^{am} and the stress at λ_{toe} based on direction, especially in Pull 1, suggests that elements contributing to the low-stress behavior, such elastin fibers and smooth muscle cells, may have preferential orientation in the transverse direction. Higher values for the parameters c_1^2 and c_2^2 in the transverse direction ($f = 2$) observed here could be interpreted as a dominant orthotropic behavior dictated by collagen fiber orientation or high-stress behavior of muscle cells. Previous studies have found preferential orientation in the longitudinal direction for collagen fibers in decellularized matrix [13] (confirmed by our findings) and preferential orientation in the transverse direction for elastin fibers in the intact pig bladder [7]. Furthermore, in [8], the authors report that the fiber distribution varies by location and across the thickness of the bladder wall, changing from mostly longitudinally oriented at the luminal side to mostly

transversely oriented close to the serosa. This is also supported by our fiber orientation analysis (**Figure 2.10c**, APPENDIX) where we analyzed a limited number of pig and human bladder histological images. The analysis shows that the bulk of fibers are oriented in the longitudinal direction in a plane close to the lamina propria (i.e., at the luminal side of the tissue). In our analysis, c^{am} , a parameter associated with elastin fibers and low-stress muscle response, assumes a high value in the transverse direction for the first pull, suggesting a high contribution of elastin and muscle in the transverse as compared to the longitudinal direction. In the second and third pull, however, the decrease in difference of c^{am} between directions is accompanied by a conserved or increase difference in c_1 and c_2 , which could be due to a preferential orientation of fibers at the outermost side of the tissue (as suggested by [8]) or to a fiber realignment mechanism. Another possibility relates to the coiling mechanism described in model M1 – the collagen fibers oriented in the longitudinal direction could be more coiled, yet more numerous, than in the transverse direction. Thus, the supraphysiologic loading seen in other studies, as opposed to the physiologically relevant loading applied in this study, could yield higher stiffness in the longitudinal direction. Lastly, testing conditions play a large role in these results. It has been shown that choice of reference configuration when defining the stress-stretch relationship can change the observed tissue anisotropy in rat bladders [14].

Several studies have reported differences in longitudinal and transverse directions in intact bladder tissue. In rodents, the longitudinal direction has been shown to be stiffer in preconditioned or tared conditions [9,10] but not under *in vitro* non-preloaded conditions [32]. In pig, only marginal differences have been found favoring either a softer longitudinal response with preload [11] or with supraphysiologic pulls [12] in contrast to a stiffer longitudinal response with preconditioning and loading under biaxial conditions [8]. In decellularized extracellular matrix, it

has been shown that the longitudinal direction is stiffer after preconditioning [13], at very high strains [7], and under reference state-conscious biaxial testing conditions [14]. However, the decellularization process may affect mechanical properties [47] by altering the amorphous elements described in our model. Interestingly, human bladders undergoing cystogram have appeared to be stiffer in the transverse direction [15], in agreement with clinical observations where the longitudinal direction experiences the greatest deformation. The experimental method described here attempts to provide a near-physiologic reference state during uniaxial testing, and may reflect an un-tared state in bladder, and thus recapitulate studies where the transverse direction appears stiffer.

2.4.5. Limitations

One limitation of the study is the type of testing performed (uniaxial tensile testing). While biaxial testing has been employed often to characterize other soft tissues, that cannot be said for most bladder studies. For this reason, performing uniaxial tests in both longitudinal and transverse directions allowed us to explore the 2D kinematic space, while providing the best possible comparison to prior studies, especially those that have explored constitutive modeling in pig bladder [12]. To choose the protocol that offered the largest opportunity for comparison with prior literature was also particularly important given the scarcity of human tissue. Furthermore, uniaxial compression, which provides a biaxial tensile deformation state in the transverse plane, was predicted accurately by our model using parameters informed by uniaxial experiments supporting the efficacy of the experiments and modeling performed in this study (**Figure 2.9**).

Assumptions were made in the implementation of M1 that limit the validity of the estimated fiber recruitment distributions, which in turn could affect the value of the material parameters within M2 (see *Section 2.3.1* for details). Specifically, values for λ_{toe} evaluated from

pigs were used for M2 parameter estimation in both pigs and humans; this could have an effect on the parameter values as well as on the statistical differences that were observed. We contend, however, that the differences we see in some parameters confirm our observations are not a forgone conclusion (support this is approach is not circular). Similarly, oxybutynin treated λ_{toe} values were used for untreated samples, and longitudinal λ_{toe} values were used for transverse samples, which could also affect the results. Of course, relatively small sample size used here for modeling have been reported in other respected studies but still presents issues with regard to our statistical analysis. Unfortunately, obtaining more human tissue was logistically impossible.

In the model presented here, smooth muscle cells are considered to be contributing to both the isotropic description, which dominates the low-stress response, as well as the orthotropic description, which dominates the high-stress response. Because of this, the assumption of W^f to be zero in compression (i.e., $\lambda^f < 1$) may not be accurate. This assumption has been made in several relevant models in literature when describing a collagen fiber network [105–108]. On one hand, we acknowledge that this constitutive approach is continuum in nature (i.e., as opposed to microstructural) and the parameters estimated must be considered descriptive of the tissue behavior at a continuum level, more than a precise characterization of the fiber's network. Therefore, this model does not have the capability of separating the contribution of collagen fibers from other fiber-like constituents, such as smooth muscle cells, that engage in the same orthotropic fashion. As muscle fibers contain and connect with collagen, teasing out this relationship would yield useful insights into the mechanical behavior of bladder tissue. On the other hand, it seems unlikely that a symmetric strain energy function is accurate in describing the behavior of any kind of fiber-like constituent when compressed. A prior study in arterial mechanics has shown how the contribution of the fiber-like constituents (both collagen and smooth muscle cells) in compression

can be represented by the same strain energy function W^f , but with parameters much lower in value (i.e., a reduction of 98% for the parameter c_1 and 72% for the parameter c_2 when in compression) [108]. Unfortunately, bladder tissue has not been as widely characterized as arterial tissue, so we do not have enough information to make a similar evaluation and for this reason we decided to assume no contribution of the fibers in compression. However, we acknowledge that in bladder tissue there is likely some orthotropic contribution from smooth muscle cell bundles when compressed, which could influence the value of Lagrange multiplier and that is not captured by the neo-Hookean component. For these reasons, the assumption of $W^f = 0$ in compression, while reasonable, represents a limitation of the model.

2.5 Acknowledgements

We would like to thank the generous individuals who donated their bodies to science which made this research possible, as well as Gift of Life Michigan for coordinating to procure the tissue. For the porcine bladders, we thank the generous and timely tissue sharing from Bartlett Lab in General Surgery at University of Michigan and the Michigan Center for Integrated Research in Critical Care. This work was funded in part with help from the American Urological Association Care Foundation (Russell Scott Jr. Urology Research Fund).

APPENDIX

Histological analysis

Mechanically tested and untested tissue specimens were fixed in 10% formalin (Fisher Scientific) and stored at 4°C. Specimens were dehydrated, embedded in paraffin, cut transversely (**Figure 2.10a**) into 5µm sections with a microtome, and stained with Verhoff Van Gieson stain (PolySciences, Warrington, PA). In Verhoff Van Gieson stain, elastin and cell nuclei are dark blue/black, collagen is red/magenta, and other tissue elements are light brown/yellow. In order to analyze specimen-wide orientation, we first captured sub-images of tissue at 400x magnification. We then compiled sub-images (up to 50 per specimen) into a single full resolution image (300dpi) using Photoshop (Adobe Systems, Mountain View, CA). Using the compiled image, four regions that traversed more than two sub-images were selected for analysis that 1) did not have muscle, 2) were central in the specimen to avoid processing artifacts, and 3) did not include blood vessels or absent space (**Figure 2.10b**). One specimen was analyzed per condition (humans and pigs) except in the human untreated specimen where three specimens were analyzed and averaged. Regions were analyzed for fiber orientation using OrientationJ (ImageJ plugin), tiling edge artifacts removed at 0 and 90 degrees, and normalized to total fiber measurements (**Figure 2.10c**).

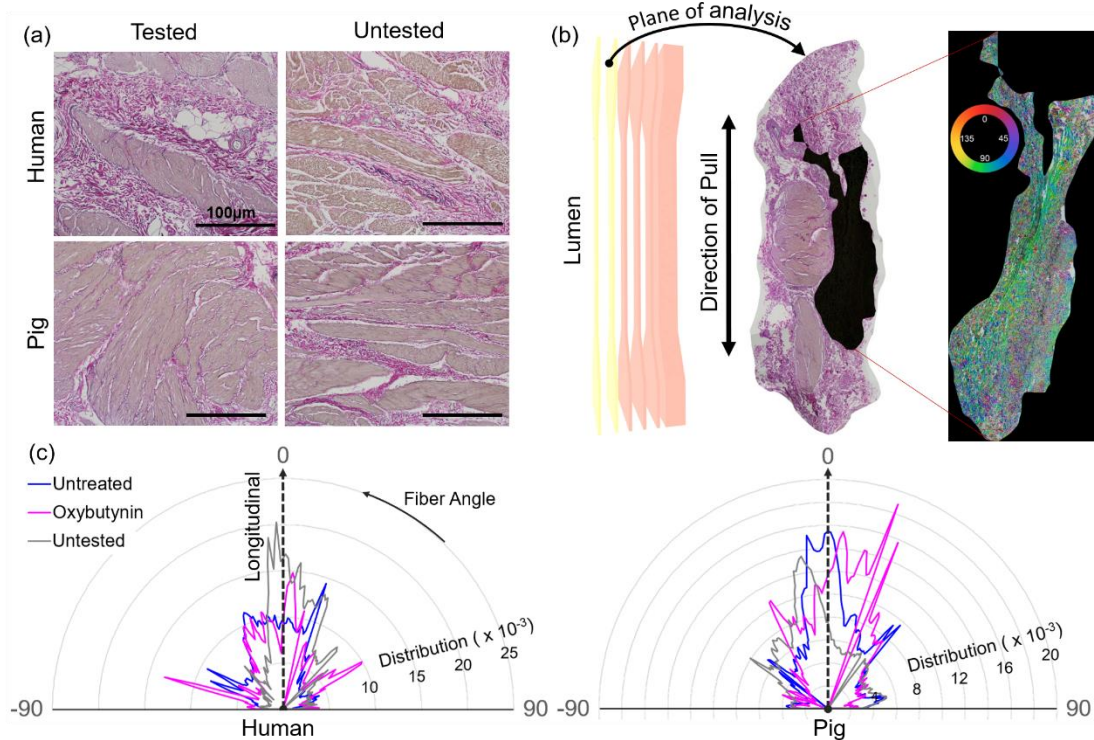


Figure 2.10 *Fiber orientation assessment*. a) Photomicrographs of Verhoff Van Gieson (VVG) stained regions human and pig, tested and untreated specimens at 400x (scale bar 100 μm). In VVG stain, elastin and cell nuclei are dark blue/black, collagen is red/magenta, and other tissue elements are light brown/yellow. b) Bladder specimens were sectioned at 5 μm along the axis of pull to maximize fiber orientation analysis. Fibrous regions were selected within specimens (shaded, center) and fiber orientation determined within selections (right, n=4 selections per specimen). Hue corresponds to the fiber angle (right, inset). c) Fiber orientation distributions (averaged over section) relative to the pulled direction in longitudinal pig and human specimens.

CHAPTER 3 - EFFECTS OF SWELLING ON THE VISCOELASTIC BEHAVIOR OF THE PORCINE URINARY BLADDER WALL

The results in this chapter are presented in [112].

3.1. Overview

Several pathological conditions that affect the mechanical characteristics of soft tissues, including the bladder, are associated with increased inflammatory response [113–115]. Inflammation has been associated with altered mechanical properties in several tissues, including mouse pancreatic islets [116], rat myocardium [117], mouse brain [118], and cartilaginous cells and tissues [119]. Moreover, tissue swelling, whether inflammatory or osmotically induced, can have profound impact on tissue mechanical response. For example, osmotically induced swelling has been shown to alter mechanical properties in human adipose tissue [120], as well as bovine intervertebral disks [121] and aorta [122]. The dynamic mechanical response of elastin from porcine thoracic aorta [123] and bovine ligamentum nuchae [124] have also been shown to change based on hydration level. Several studies have uncovered how the mechanical properties of soft tissues can be dependent on the level of hydration, such as in the human stratum corneum [125], human osteoarthritic cartilage [126], rat intervertebral disks [127], and avian keratin [128]. Not only *in vitro*, but also *in vivo* studies have highlighted a similar dependency. Dittmann et al. found that the mechanical properties of *in vivo* human spleen, pancreas, and liver can change after consumption of 1 liter of water [129]. Additionally, theoretical modeling of inflated spheres and fiber-reinforced tubes subjected to swelling show altered mechanical response [130–132]. Yet, to date no study has evaluated the effect of tissue hydration/swelling on the mechanical properties of the bladder. This could play a crucial role in defining the viscoelastic behavior of the organ wall due to the known

involvement of inflammation response in several urological pathological conditions [113–115] and the wide range of urine osmolarities [133]. In a healthy mammalian bladder, the organ wall is protected from urologic constituents by the urothelium [134,135]. However, acute injury or inflammation can lead to changes in permeability of the urothelium [135]. It has been shown that spinal cord injury in rats leads to increased urothelial permeability shortly after injury [136], and bacteria and positively charged proteins (i.e., from eosinophils or sperm) can increase permeability in the urothelium and lead to cell swelling and cell lysis [134,137]. Osmotic gradients have been shown to decrease tissue electrical resistance and increase mucosal permeability in toad bladders [138,139]. Finally, while the quasi-static mechanical characteristics of the bladder have been shown to differ between orientations [7–15] and anatomical locations [7,8], no study has evaluated differences in viscoelastic behavior based on anatomical location in the bladder.

In this study, we tested porcine bladder to identify if anatomical locations and osmotic swelling play a role in the tissue's viscoelastic characteristics. We investigated this relationship using a series of stress-relaxation experiments as well as a modified Maxwell-Wiechert model to aid in the interpretation of the experimental data. Our results highlight how tissue located near the neck of the bladder seems to present significantly different viscoelastic characteristics than the body of the organ. This supports what was previously observed and is a valuable contribution to the understanding of the location-specific properties of the bladder. We also tested the effect of osmotic swelling, revealing that the bladder's viscoelastic behavior is mostly independent of solution osmolarity in hypoosmotic solutions, but the use of a hyperosmotic solution can significantly affect its behavior. This is significant, since several urinary tract pathologies can disrupt the urothelial barrier causing increased urothelial permeability, thus subjecting the bladder wall to non-physiologic osmotic challenge. This could have implication in determining changes in

cellular stress states during acute inflammation and/or increased urothelium permeability, which may be a contributing factor in driving tissue remodeling (such as fibrosis).

3.2. Methods

3.2.1. Tissue procurement

Porcine bladders were obtained at time of slaughter from a local slaughterhouse, and transported to the lab in airtight bags in an insulated container. Bladders were stored in the airtight bags in a refrigerator at 2°C until tissue preparation for the experiments was performed

3.2.2. Experimental protocols

3.2.2.1. Tissue swelling

Bladder tissue was soaked in a modified Krebs-Henseleit buffer solution (Sigma-Aldrich, calcium-free) of varying osmolarity to induce tissue swelling. The values of osmolarity tested were 100, 300, 600, and 900 mOsm/L. The isosmotic solution (300 mOsm/L) consisted of 2.0 g/L D-Glucose, 0.141 g/L Magnesium Sulfate [Anhydrous], 0.16 g/L Potassium Phosphate Monobasic, 0.35 g/L Potassium Chloride, 6.9 g/L Sodium Chloride, and 2.1 g/L Sodium Bicarbonate. Other osmolarities were created by simply increasing or decreasing the concentration of the aforementioned contents. All solutions were adjusted to pH 7.4 with 1M hydrochloric acid. The specific osmolarity levels tested in the study were chosen for the following reasons. Human plasma has a natural osmolarity near 300 mOsm/L [140], making 300 mOsm/L a reasonable value to use to mimic physiological conditions of the healthy bladder wall. To induce swelling, we chose 100 mOsm/L which represents the low end of urine osmolarity [133]. Additionally, a pilot study showed that 100 mOsm/L is the most hypo-osmotic solution with no evidence of cell lysis. Since urine can

have osmolarities ranging from 100-1200 mOsm/L [133], we also included 600 and 900 mOsm/L solutions as examples of hyperosmotic solutions.

Tissue preparation for the swelling experiment was performed within 6 hours of animal slaughter. Bladders (n=5) were cut along the lateral edge and flattened (see **Figure 3.1** for images of a representative flattened bladder). A 9 mm diameter circular punch was used to create cylindrical samples from the bladder wall. Five samples were taken from each of the five anatomical locations of interest (dorsal, ventral, lateral, lower body, and trigone). **Figure 3.1a** depicts all samples taken from a representative bladder for the swelling study.

All samples were soaked for 18 hours in 5 mL of modified Krebs-Henseleit buffer solution with an osmolarity of 300 mOsm/L at 2°C. Samples were removed, dabbed on delicate task wipers (Kimtech Science) to remove extraneous solution, then weighed (Acculab AL-64) and imaged (Dual Pixel 12MP OIS, F1.7). **Figure 3.2a-b** shows representative top and side view images of samples for the swelling experiment. Samples were then switched from the initial 300 mOsm/L solution to a new solution (5 mL) with an osmolarity of 100, 300, 600, or 900 mOsm/L, for 18 hours (i.e., one sample per location per solution for each bladder). Samples were again removed, dabbed on delicate task wipers to remove extraneous solution, then weighed and imaged.

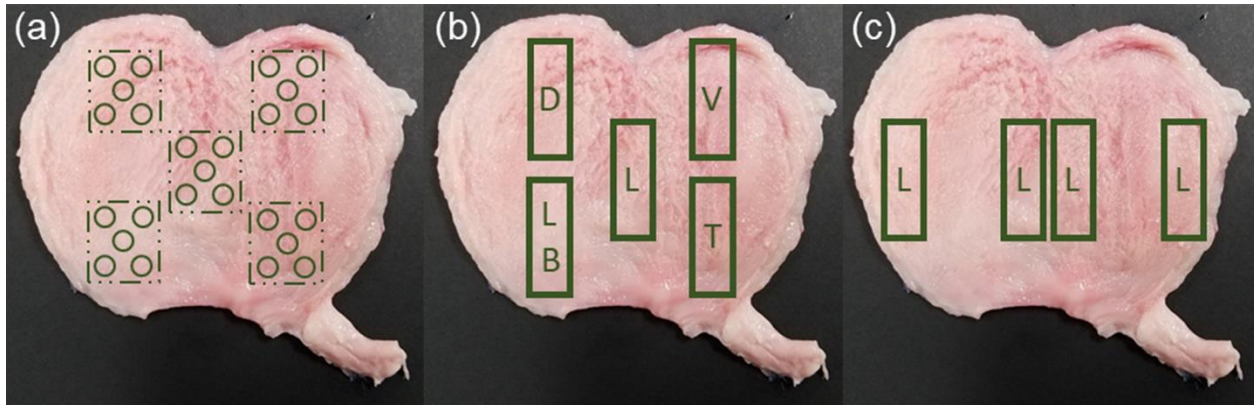


Figure 3.1 Representative bladder after being dissected and flattened. Schematic representations of the locations and number of samples taken from each bladder for (a) the swelling study (9mm diameter punch samples), (b) the anatomical location and (c) the variable-solution osmolarity stress-relaxation experiments. The rectangular punch measured 10mm \times 30mm for the samples shown in both (b) and (c).

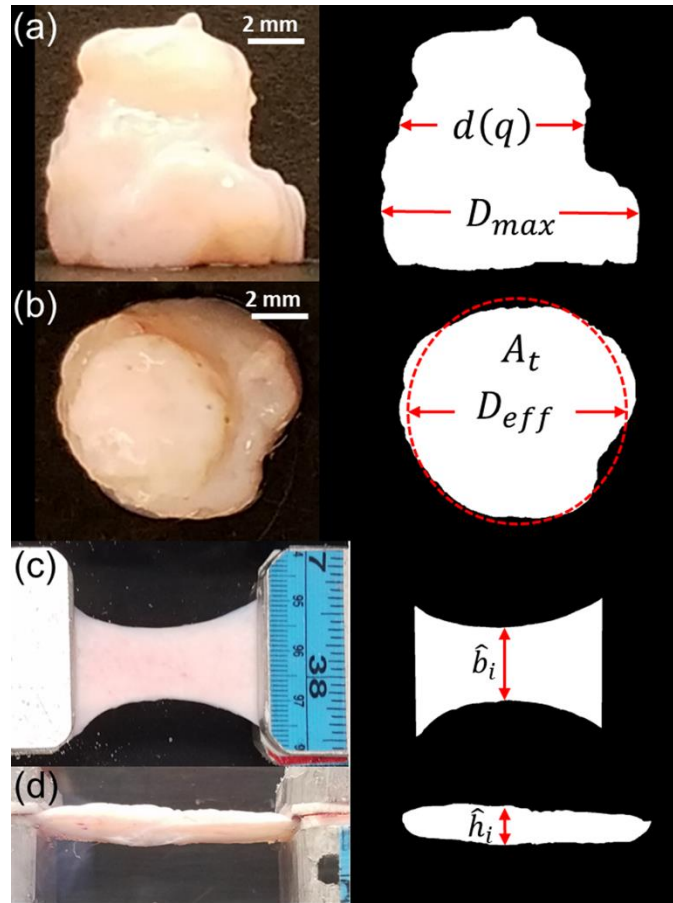


Figure 3.2 Side view (a) and top view (b) of representative 9mm diameter punch sample for the swelling experiment, before (left) and after (right) manual thresholding. Top view (c) and side view (d) of representative 10mm \times 30mm rectangular punch sample for the stress-relaxation experiments, before (left) and after (right) manual thresholding. Binary images (left column) show a schematic of all relevant geometric definitions for the evaluation of volume and cross-sectional area, see Equations (3.1)-(3.3).

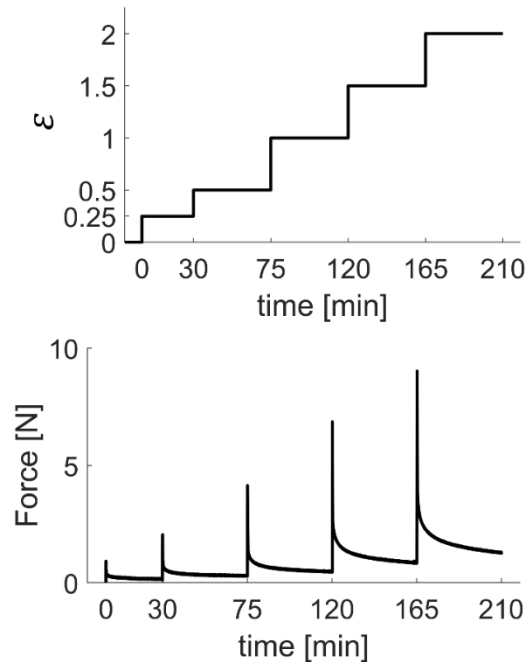
3.2.2.2. Stress-relaxation

Tissue preparation for the stress-relaxation experiment was performed 1-6 hours after animal slaughter. Bladders (n=6) were cut along the lateral edge and flattened. A 10mm × 30mm rectangular punch was used to create rectangular samples from the bladder wall in the longitudinal (apex-to-base) direction. Stress-relaxation tests were split into two separate experiments (i.e., to identify location-specific behaviors and the effect of osmolarity separately). Three bladders were used for each experiment. For the location experiment, one sample was taken from each of the five anatomical locations, as shown in **Figure 3.1b**. For the osmolarity experiment, four samples were taken from the lateral location, as shown in **Figure 3.1c**, to eliminate the effect of location.

Punched samples were placed in air-tight bags and refrigerated at 2°C until undergoing a swelling procedure. For the swelling procedure, samples were submerged in 10 mL of modified Krebs-Henseleit buffer solution for 18 hours at 2°C. For the location-specific experiment, all samples were soaked in solution with an osmolarity of 300 mOsm/L. For the variable-osmolarity experiment, samples were soaked in solutions of either 100, 300, 600, or 900 mOsm/L. The swelling procedure was started 2-36 hours after slaughter and the start times of the procedure were randomized for each bladder.

Directly after the swelling procedure, uniaxial stress-relaxation tests were performed on a custom uniaxial tensile testing machine with samples fully submerged in room temperature modified Krebs-Henseleit buffer solution with the specific testing osmolarity. Samples were mounted to the uniaxial testing machine using clamps with sand-paper grips. Force was measured with a 10lb capacity load cell (Honeywell, Model 31 Mid Range Precision Miniature Load Cell) at a sampling frequency of 200 Hz. A 0.05 N preload was added to the samples by incrementally distending the samples to a load of 0.05 N for 10-15 minutes until a steady state 0.05 N load was

reached. Stress-relaxation steps were performed with a displacement rate of 50 mm/s. While large deformations in tissue mechanics are generally defined in terms of stretch, deformations in this study are defined in terms of engineering strain (i.e., $\hat{\epsilon}_i = [l_i - l_0]/l_0$) to remain consistent with common structural viscoelastic model nomenclature [11,56,59–61,64,66–68,141]. The sample's lengths were defined during testing as distance between clamps after preloading (l_0) and after each loading step (l_i). Multi-step stress-relaxation was performed for loadings corresponding to strains $\hat{\epsilon}_i = [0.25, 0.5, 1.0, 1.5, 2.0]$. Relaxation times were 30 minutes for the first step, and 45 minutes for all subsequent steps, leading to step-loading timings of $\hat{t}_i = [0, 30, 75, 120, 165]$ minutes. **Figure 3.3** shows strain and force history for a representative test. Immediately after preloading and each loading step, top and side-view images of the samples were taken (Dual Pixel 12MP OIS, F1.7) to estimate sample cross-sectional area. No evidence of sample slipping was found in any



test.

Figure 3.3 Stress-relaxation protocol for a representative sample. Applied strain (top) and recorded force (bottom) data, as a function of test time. This protocol was employed in all stress-relaxation experiments (i.e., anatomical location and variable solution osmolarity).

3.2.3. Data analysis

3.2.3.1. Tissue swelling

Two metrics were used to quantify tissue swelling: relative change in sample mass and relative change in sample volume. These metrics are defined as follows,

$$\bar{m} = m_2/m_1, \quad (3.1a)$$

$$\bar{V} = V_2/V_1, \quad (3.1b)$$

where \bar{m} and \bar{V} are relative mass and volume, m_1 and V_1 are mass and volume measured when removed from the first solution (300 mOsm/L for all samples), and m_2 and V_2 are the final mass and volume measured when removed from the testing solution (100-900 mOsm/L). The values for mass are taken directly from the scale measurements, while volume must be calculated using top and side-view images of samples. Manual thresholding was used to convert images to binary (see **Figure 3.2a-b**). To estimate the volume, V , of the samples, the following equations were implemented,

$$V = \sum_{q=1}^n \frac{\pi}{4\delta} \left[d(q) \frac{D_{eff}}{D_{max}} \right]^2, \quad (3.2a)$$

$$D_{eff} = 2 \sqrt{\frac{A_t}{\pi}}, \quad (3.2b)$$

where q represents the pixels' row of interest in the side-view image, n is the total number of pixels' rows in the side-view image for each sample, δ the side-view image scale in pixels/mm, $d(q)$ is the sample diameter (white pixels) for the q -th row in the side-view binary image, D_{max} is the horizontal distance between the right-most and left-most white pixels in the side-view image, and D_{eff} is the effective sample diameter calculated using the total sample area from the top-view image A_t . See **Figure 3.2a-b** for a schematic of the parameters used in Equations (3.1) and (3.2).

3.2.3.2. Stress-relaxation

Note that here, and moving forward, every variable represented with a hat and a subscript i (i.e., $\hat{*}_i$) is a variable that assumes a constant value, different for each i -th loading step, while every variable represented without a hat is considered to be varying with time (i.e., its value is a function of time t and could change within the duration of each i -th loading step), except material parameters which are characteristic of the tissue independent of time and of loading step (i.e., c_a , c_b , c , and η_j).

For the stress-relaxation experiments, the stress σ as a function of time t is calculated as follows,

$$\sigma(t) = F(t)/\hat{A}_i, \quad (3.3a)$$

$$\hat{A}_i = \hat{b}_i \hat{h}_i, \quad (3.3b)$$

where F is the force (function of time t) and \hat{A}_i is the cross-sectional area of the sample at the i -th loading step, calculated using the top and side-view images. **Figure 3.2c-d** shows a sample's top and side-view images before and after converting to binary via manual thresholding, where \hat{b}_i is defined as the minimum sample width and \hat{h}_i is defined as the thickness of the sample at the location of \hat{b}_i .

The number of data points for considered for modeling for each loading step was reduced to 200 using a custom logarithmic-like spacing. Two metrics were used to characterize the stress-relaxation behavior, namely, peak stress ($\hat{\sigma}_i^p$) and relaxed stress ($\hat{\sigma}_i^r$). Peak stress was defined as the maximum stress achieved after each loading step (i.e., the first point of the stress-relaxation curve). To find the relaxed stresses, we averaged the value of stress from the last two time points for each step. Due to the optimized spacing, the final two time points spanned 103.8 seconds for all loading steps, except the first for which the spanned 63 seconds.

3.2.4 Modeling

3.2.4.1 Modified Maxwell-Wiechert model

Previous studies have used hyperelastic [9,13,75,76,14,15,69–74] and viscoelastic [11,12,64–68,142,21,56,57,59–63] models to describe the mechanical behavior of the bladder in various species. For this study we employed a modified Maxwell-Wiechert model with three Maxwell elements (see the schematic in **Figure 3.4**). Several studies have used variations of the Maxwell-Wiechert model for describing the viscoelastic behavior of the bladder [11,56,60,63,64,66–68]. Nonlinear spring elements were included in the model to capture the nonlinear mechanical behavior of the bladder, similar to Mastrigt & Nagtegaal [60]. Specifically, the standalone spring has a stiffness, \hat{k}_i^0 , that increases exponentially with strain,

$$\hat{k}_i^0 = c_a e^{c_b \hat{\varepsilon}_i}, \quad (3.4)$$

where c_a and c_b are the spring material parameters with units of stress and dimensionless, respectively. The stress response, $\hat{\sigma}_i^0$, of the standalone spring is,

$$\hat{\sigma}_i^0 = \hat{k}_i^0 \hat{\varepsilon}_i. \quad (3.5)$$

Additionally, the Maxwell element springs have stiffness $k_{ij}(t)$ that increases linearly with strain of the spring, $\varepsilon_{ij}^s(t)$,

$$k_{ij}(t) = c_j \varepsilon_{ij}^s(t), \quad (3.6)$$

where c_j is material parameter with units of stress for the j -th spring. To decrease the number of parameters estimated in this study, $c_j = c$ is constrained to be equal for all three modified Maxwell elements. All dashpots in this model are standard dampers for which the stress is proportional to rate of strain. The stress response, $\sigma_{ij}(t)$, for the j -th modified Maxwell element at the i -th loading step (identified by the strain level $\hat{\varepsilon}_i$ applied at time t_i) can be evaluated as

$$\sigma_{ij}(t) = k_{ij}(t) \varepsilon_{ij}^s(t), \quad \text{for } \hat{t}_i \leq t < \hat{t}_{i+1}, \quad (3.7a)$$

$$\varepsilon_{ij}^s(t) = \frac{\eta_j \hat{\varepsilon}_{ij}^s}{\eta_j + \hat{\varepsilon}_{ij}^s c [t - \hat{t}_i]}, \quad (3.7b)$$

$$\hat{\varepsilon}_{ij}^s = [\hat{\varepsilon}_i - \hat{\varepsilon}_{i-1}] + \varepsilon_{(i-1)j}^s(t) \Big|_{t=\hat{t}_i}, \quad (3.7c)$$

where η_j represents the dashpot constants with units of [stress·time]. Initial conditions (for $i = 0$) are needed to specify the relaxation function defined in Equations (3.7), and are defined as $\hat{\varepsilon}_0 = 0$ and $\varepsilon_{0j}^s(\hat{t}_1) = 0$. The stress-time response of the whole system is

$$\sigma_i(t) = \hat{\sigma}_i^0 + \sum_{j=1}^3 \sigma_{ij}(t). \quad (3.8)$$

For a standard Maxwell element, the time constant for relaxation after step-loading can be found by extending a tangent line from the relaxation function at $t = 0$ to the intercepting point on the time-axis for the given Maxwell element. Following this method, pseudo time-constants τ_{ij} for the modified Maxwell elements in this model are defined as

$$\tau_{ij} = \frac{\eta_j}{2c\hat{\varepsilon}_{ij}^s}. \quad (3.9)$$

Because of the strain dependent stiffness of the spring in the modified Maxwell elements, the pseudo time-constants are strain dependent, unlike standard Maxwell elements. For purposes of parameter comparison, $\hat{\varepsilon}_{ij}^s$ was set as a constant with a value of 0.5, rationalized by the fact that the most common jump in strain between steps is 0.5. This assumption simplifies the time-constants to $\tau_{ij} \cong \bar{\tau}_j = \eta_j/c$. This decision only affects the calculated time-constants used for statistical analysis, and is not associated with the mathematical description of the model or the parameter estimation process.

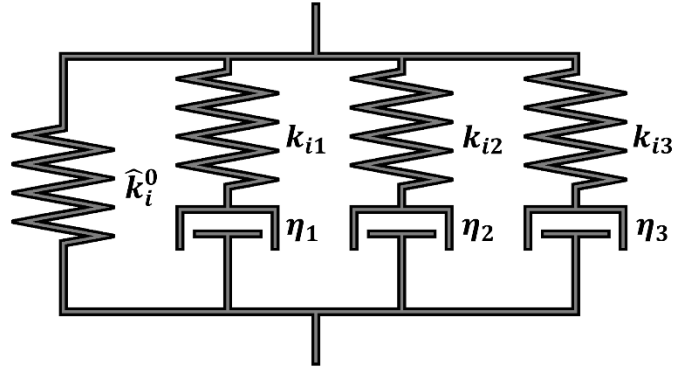


Figure 3.4 Schematic of the modified Maxwell-Wiechert model. The standalone spring's stiffness increases exponentially with strain (\hat{k}_i^0), while the springs in the three Maxwell elements have stiffnesses that increase linearly with strain (k_{ij}). The dashpots are standard linear dampers (η_j).

3.2.4.2 Parameter estimation

The purely elastic behavior of the tissue can be approximately identified by considering $\hat{\sigma}_i^r$ vs $\hat{\epsilon}_i$. This was assumed to correspond to the model undergoing deformation at a strain-rate sufficiently low that viscous effects from the dashpots were negligible. In this scenario, only the standalone exponential spring dictates the stress-strain response. The exponential spring parameters (c_a and c_b) were estimated by minimizing the sum of squared error (SSE) between the relaxed model response and the relaxed stress-strain behavior of the data. Then, the remaining parameters (c and η_j) were estimated by minimizing SSE between the total multi-step model output and the stress-relaxation data. Loading steps were considered instantaneous during parameter estimation. This method separates the parameter estimation into multiple steps, thus lowering uncertainty by decreasing the number of parameters estimated simultaneously. All parameter estimation was performed using *fminsearch* in MATLAB.

3.2.5 Statistical analysis

All statistical testing consisted of 2-way or 3-way ANOVAs (depending on the number of sources of variation), followed by Tukey-Kramer multiple comparisons tests for all pairwise multiple

comparison procedures. For swelling experimental data, the two metrics of tissue swelling, \bar{m} and \bar{V} , were the dependent variables. Sources of variation included animal, anatomical location, and solution osmolarity. For stress-relaxation experimental data, the two metrics for stress-relaxation $\hat{\sigma}_i^p$ and $\hat{\sigma}_i^r$ were the dependent variables. For the location-specific stress-relaxation experiment, sources of variation included animal, anatomical location, and strain level. For the variable-osmolarity stress-relaxation experiment, sources of variation included animal, solution osmolarity, and strain level. For the modeling, the estimated model parameters were the dependent variable. Sources of variation included animal and location for the location-specific parameters, and animal and solution osmolarity for the variable-osmolarity parameters.

3.3. Results

3.3.1. Tissue swelling

Figure 3.5 shows the swelling of bladder tissue at different anatomical location for different osmolarity values, presented as mean and standard deviation of relative mass and relative volume. First, both relative mass and volume decrease with increasing osmolarity ($p < 0.01$ for both parameters). Pairwise comparisons showed differences between all groups ($p < 1E-6$ for \bar{m} , $p < 0.006$ for \bar{V}) except between 600 and 900 mOsm/L. When looking at trends in locations, it appears that swelling at lower osmolarities (100 and 300 mOsm/L) is similar between locations, but at higher osmolarities (600 and 900 mOsm/L) swelling in locations close to the neck of the bladder (lower-body and trigone) appears to not be affected as much as the other locations, particularly when looking at \bar{m} . Statistical analysis shows that dorsal samples have significantly lower relative mass than lower body ($p=0.003$) and trigone ($p=0.001$) samples. Some differences

are seen between relative mass values for different bladders ($p < 0.05$, 2 of 10 comparisons), but no differences in relative volume.

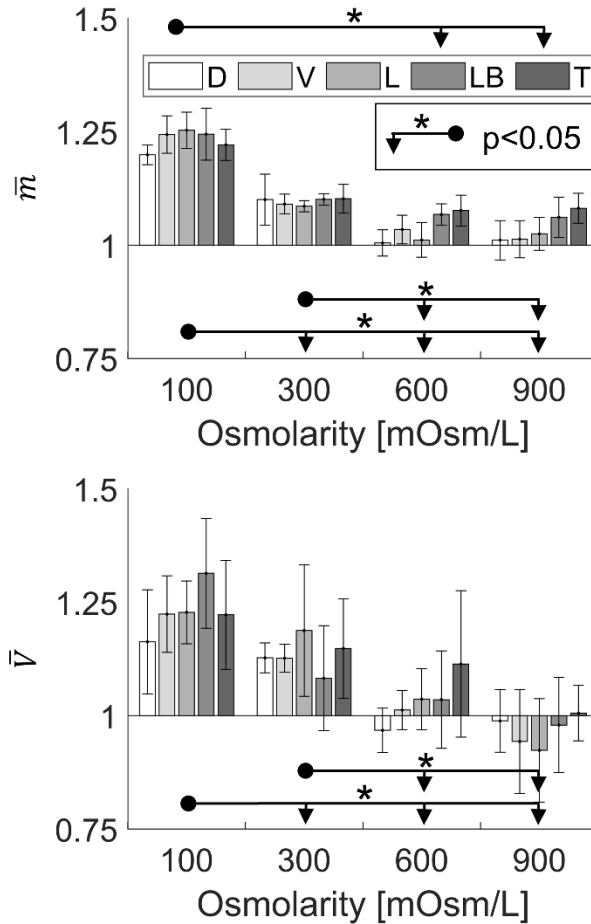


Figure 3.5 Relative mass (\bar{m} , top) and relative volume (\bar{V} , bottom) for the different solution osmolarities and anatomical locations, namely dorsal (D), ventral (V), lateral (L), lower body (LB), and trigone (T). Each bar represents the mean and standard deviation from 5 bladders. For 100 mOsm/L, all samples have a $\bar{m} > 1$ and almost all samples (24 of 25, 96%) have $\bar{V} > 1$. For 300 mOsm/L, all samples have $\bar{m} > 1$, D and V samples all have $\bar{V} > 1$, but some L (1 of 5), LB (2 of 5), and T (1 of 5) samples have $\bar{V} < 1$. For 600 mOsm/L some D (2 of 5) and L (1 of 5) samples have $\bar{m} < 1$ and about half of all samples show $\bar{V} < 1$ (13 of 25, 52%). For 900 mOsm/L some D (2 of 5), V (2 of 5), and L (1 of 5) samples have $\bar{m} < 1$ and over half of all samples show $\bar{V} < 1$ (16 of 25, 64%).

3.3.2. Stress relaxation experimental data

Figure 3.3 shows plots of applied strain and recorded force history for a representative stress-relaxation experiment. **Figure 3.6** shows stress-relaxation data (reduced to 200 points per step)

from a representative sample with time represented relative to the start of each step. Both linear and logarithmic timescales are shown for the same data. In **Figure 3.6** it can be appreciated that stresses are greater at higher values of strain, as expected.

Figure 3.7 (top) shows peak and relaxed stresses for all anatomical locations at each loading step. It is evident that both peak and relaxed stresses increase with level of applied strain, as expected. Additionally, lower body and trigone regions appear to have higher peak and relaxed stresses than dorsal, ventral, and lateral regions. Statistical analysis shows both peak stress ($p < 0.0002$) and relaxed stress ($p = 0.0002$) differs with location. Pairwise differences based on location are the same for peak and relaxed stresses, i.e. trigone stresses are significantly higher than dorsal ($p < 0.0003$), ventral ($p < 0.05$), and lateral ($p < 0.02$), and lower body stresses are significantly higher than dorsal ($p < 0.02$). No differences are found with respect to different bladders.

Figure 3.7 (bottom) shows peak and relaxed stresses for different solution osmolarities at each loading step. Qualitatively, stresses appear to increase with increasing osmolarity, except when comparing 100 vs 300 mOsm/L. Statistical analysis shows both peak stress ($p < 1E-6$) and relaxed stress ($p = 2E-7$) differ with osmolarity. Pairwise comparisons show 900 mOsm/L samples have significantly higher peak and relaxed stresses than 100 ($p < 0.001$), 300 ($p < 7E-6$), and 600 ($p < 0.008$) mOsm/L samples. Unlike the location-based experiment, differences are seen between bladders ($p < 1E-6$ for $\hat{\sigma}_i^p$, $p < 0.0002$ for $\hat{\sigma}_i^r$) for the variable-osmolarity experiment.

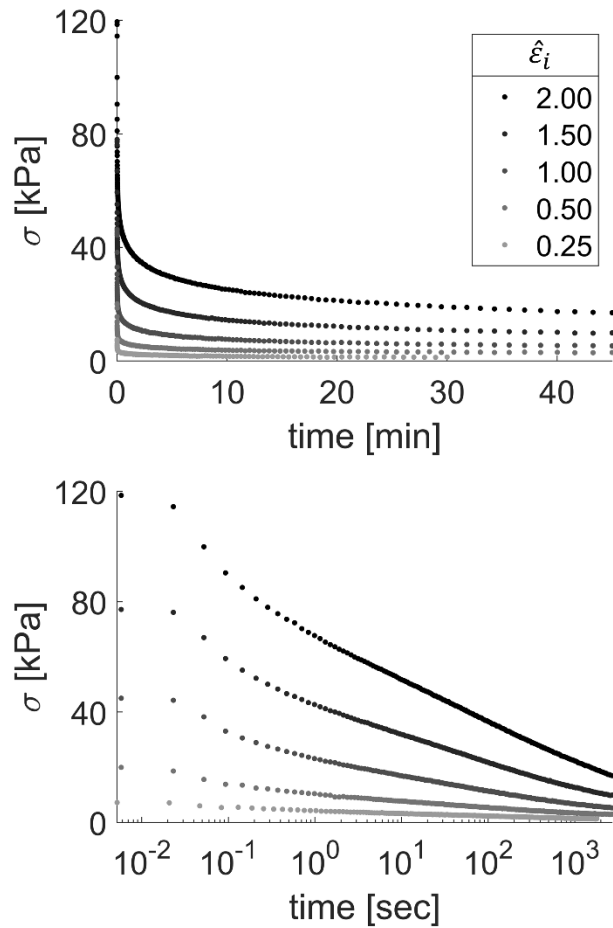


Figure 3.6 Stress-relaxation curves as a function of time relative to the start of each loading step for a representative sample. The same data is shown for a linear timescale (top) and logarithmic timescale (bottom). The number of data points in each curve is 200 and have been identified by using a customized logarithmic-like spacing. A grey-scale color gradient has been employed to represent the different values of applied strain, from the lightest representing the smallest strain in the protocol ($\hat{\varepsilon}_1 = 0.25$) to the darkest representing the largest strain in the protocol ($\hat{\varepsilon}_5 = 2.0$).

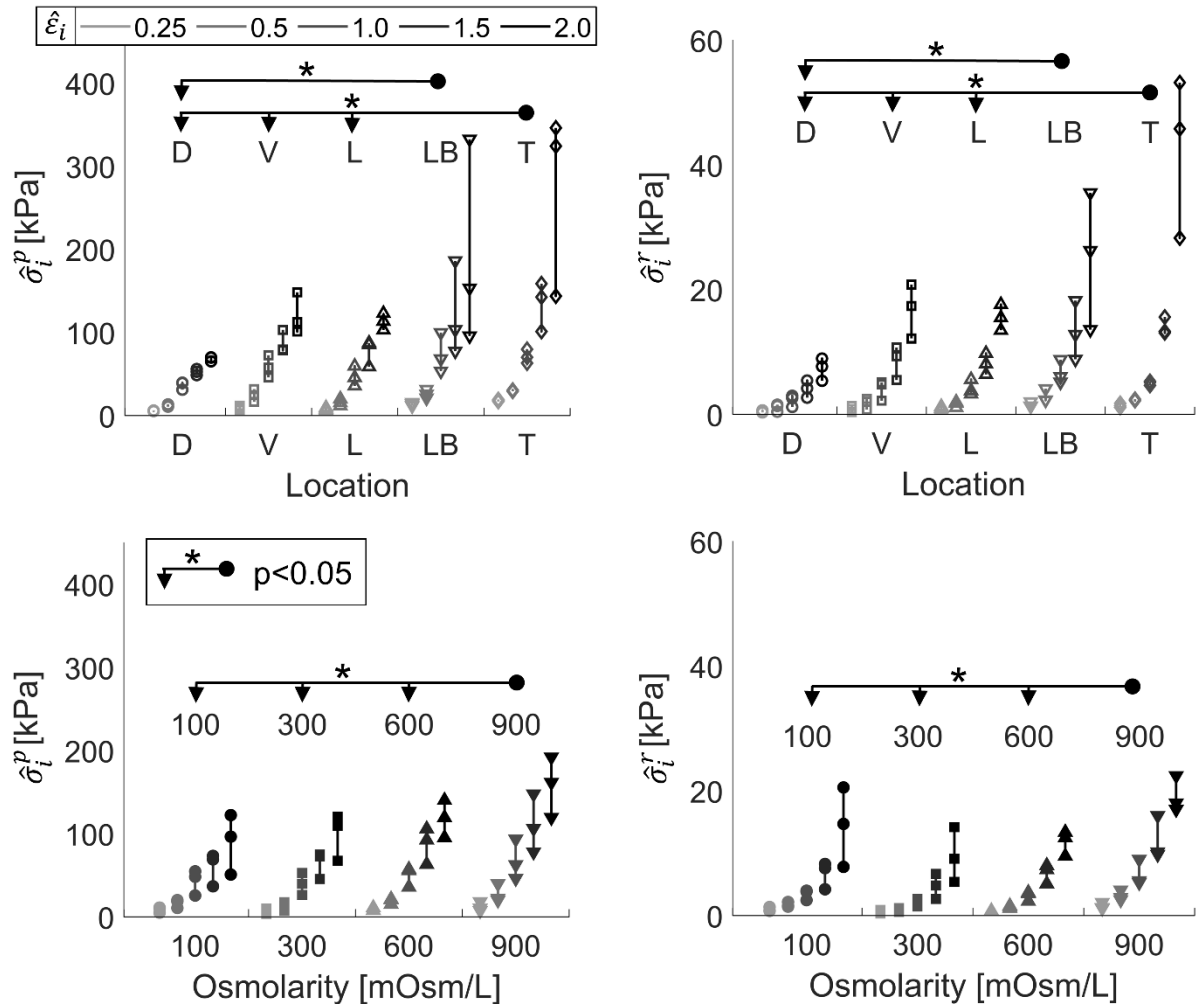


Figure 3.7 Stress-relaxation results for all samples showing peak stresses ($\hat{\sigma}_i^p$, left) and relaxed stresses ($\hat{\sigma}_i^r$, right) for different anatomical locations (top) and osmolarities (bottom). Open symbols are used to identify the anatomical location experiments and closed symbols to identify the varying solution osmolarity experiments. A grey-scale color gradient has been employed to represent the different values of applied strain, from the lightest representing the smallest strain in the protocol ($\hat{\epsilon}_1 = 0.25$) to the darkest representing the largest strain in the protocol ($\hat{\epsilon}_5 = 2.0$). An asterisk represents a statistically significant difference ($p < 0.05$) and the relevant comparison is represented by an arrow.

3.3.3. Modeling results

Figure 3.8 shows comparisons for all material parameters and groups from the location-specific experiment. When looking at the elastic parameters (i.e., exponential spring), c_a is significantly higher in lateral samples when compared to trigone ($p < 0.05$), and c_b is significantly higher in trigone compared to all other locations ($p < 0.05$). The only significant differences found in the

viscoelastic parameters (i.e., parameters associated with the modified Maxwell elements), are that $\bar{\tau}_3$ is higher in the trigone region when compared to both the dorsal and lower body regions ($p < 0.05$). No differences are seen between bladders for any model parameters in the location experiment.

Figure 3.9 shows plots of parameter estimates for all parameters and groups from the variable-osmolarity experiment. The exponential spring material parameter c_a is significantly higher for samples tested in 900 mOsm/L solution compared to all other osmolarities ($p < 0.05$). When considering the viscoelastic parameters, both η_3 and $\bar{\tau}_3$ have significantly higher values for 900 mOsm/L compared to all other osmolarities ($p < 0.01$). Additionally, c and η_1 are significantly higher in samples tested in a 900 compared to 300 mOsm/L. No differences are seen between bladders for any model parameters in the osmolarity experiment.

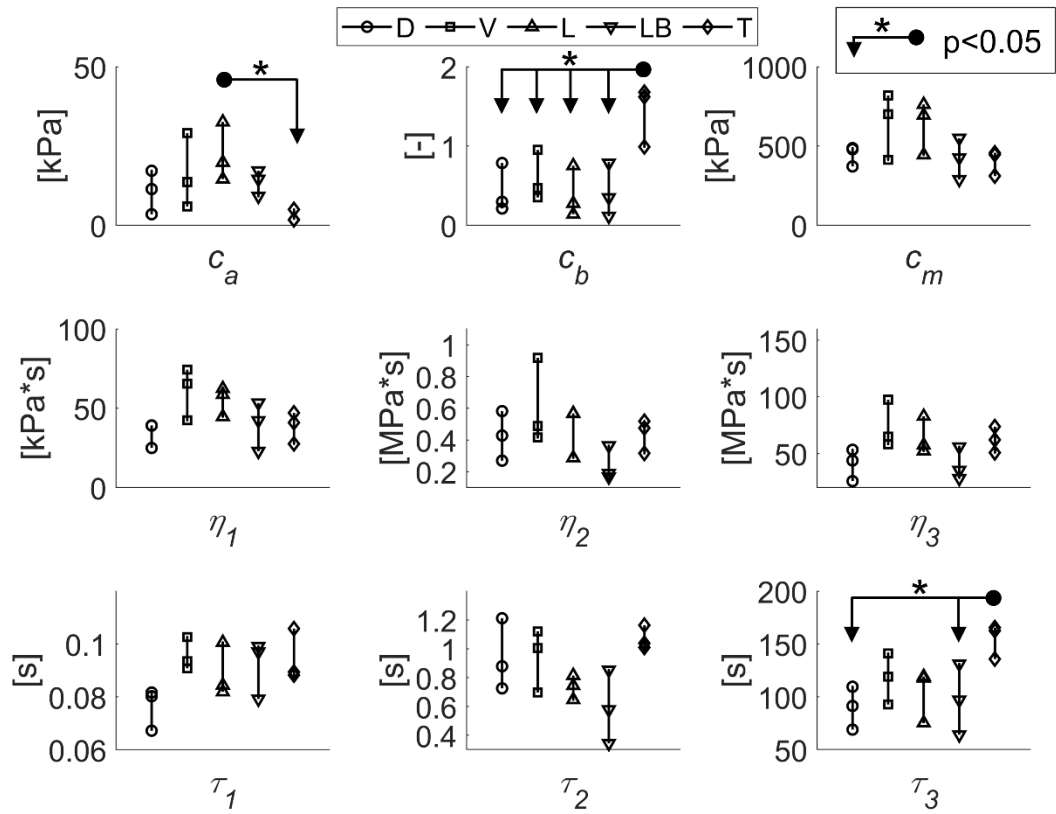


Figure 3.8 Estimated values of the parameters for the modified Maxwell-Wiechert model when considering the anatomic location experiment. Open symbols are used to identify the different anatomical locations (as specified in the legend). An asterisk represents a statistically significant difference ($p < 0.05$) and the relevant comparison is represented by an arrow.

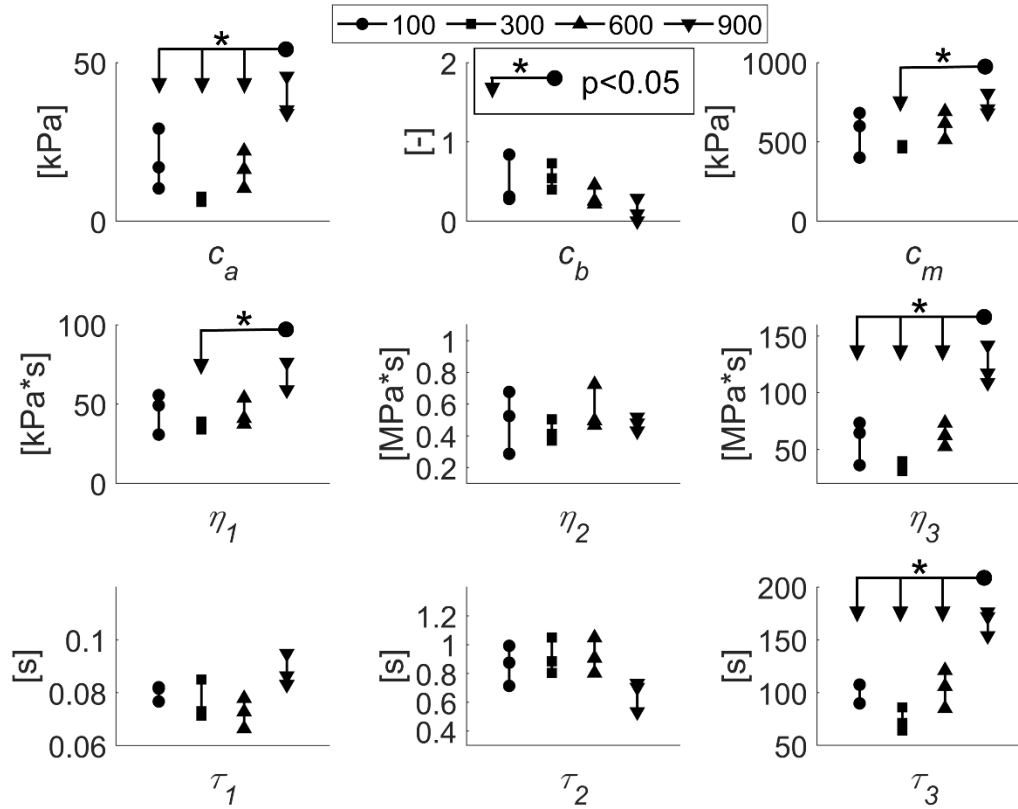


Figure 3.9 Estimated values of the parameters for the modified Maxwell-Wiechert model when considering the variable solution osmolarity experiment. Closed symbols are used to identify the different solution osmolarities (as specified in the legend). An asterisk represents a statistically significant difference ($p < 0.05$) and the relevant comparison is represented by an arrow.

3.4. Discussion

3.4.1. Tissue swelling

The results shown in **Figure 3.5** suggest that subjecting the bladder to changing levels of urine and/or serum osmolarity could result in altered bladder wall thickness and geometry. It is generally accepted that the urothelium protects the bladder wall from the osmotic challenge of urine [134,135]. However, several diseases and dysfunctions of the bladder are associated with changes in urothelium permeability [134–137]. This study suggests that, in cases of compromised urothelium, urine osmolarity could lead to varying levels of tissue hydration and, consequently, changes in bladder wall thickness and geometry. Differences in location-based swelling suggest

that the regions close to the neck of the bladder (lower body and trigone) are less affected by the presence of increased osmolarity, when compared to the regions located close to the dome (particularly the dorsal region).

3.4.2. Stress-relaxation

A prior study reported on the uniaxial (apex-to-base direction) stress-relaxation behavior of porcine bladder strips taken from the lateral location [16]. The results presented in [16] show comparable values of relaxed stresses, but significantly lower values of peak stresses, when compared to our study. The discrepancy between peak stresses is likely due to differences in experimental protocol. Jokandan and colleagues in [16] used a protocol significantly different than the one employed here, specifically in the loading conditions (strain levels, displacement rate, relaxation times, time submerged in isosmotic solution prior to testing, preconditioning), as well as in the sample geometry definition (cross-sectional area measurement, sample lengths). Furthermore, while the samples in our study were tested submerged in solution, in [16] the authors employed intermittent misting to ensure hydration of the samples. The possible effect of these protocol discrepancies on the values of peak stress for this tissue highlights the need for more consistent tissue testing protocols between different studies. This would minimize the amount of variability in recorded tissue behavior and increase the capability of comparison across studies. Further illustrating this point, Mastrigt & Nagtegaal performed stress-relaxation tests on pig bladder strips at different strain rates and found that viscoelastic parameters depend on rate of step-wise loading [60].

When comparing peak and relaxed stresses (**Figure 3.7**), we found that the lower body and trigone regions showed significantly higher values than all other anatomical regions, particularly at high levels of strain. This finding suggests that the porcine bladder is stiffer closer to the neck

of the bladder. This supports previous work that has shown little location-based difference in porcine bladder stiffness at low levels of strain, but stiffer behavior in the lower body and trigone regions at high levels of strain [7,8]. Some significant differences are also seen for peak and relaxed stresses between solution osmolarities. Stresses generally increase with increasing osmolarity. Specifically, samples tested in a 900 mOsm/L solution showed significantly higher stresses than all other conditions. Knowing that urothelium permeability can increase in pathological conditions [134–137] and that 900mOsm/L is within the range of physiologic urine osmolarity [133], these results suggest that high urine osmolarity in some pathological conditions may contribute to increased stresses felt by cells in the bladder wall, and consequently act as a contributing factor in driving remodeling.

3.4.3. Modeling

The model presented in this study provided a better description of the experimental data when compared to a conventional Maxwell-Wiechert model (preliminary study, model predictions not shown). First, the introduction of an exponential standalone spring allows an adequate description of the tissue's elastic response, which has been shown to be exponential-like [12]. Second, a preliminary analysis showed that a prohibitively large number of Maxwell elements were necessary to achieve a reasonable description of the tissue's viscoelastic behavior. That is because a single Maxwell element results in an exponential relaxation, and if a single element is used to describe the behavior of this tissue only a small portion of the curve is represented adequately. Increasing the number of Maxwell elements would improve the description, but also result in an increase in the number of model parameters, resulting in higher uncertainty and lower confidence in the estimation. The model presented here aims to improve the description of the observed behavior by modifying the shape of the model relaxation curve, rather than increase the number of

elements. By making the spring stiffness strain-dependent, we enable the model to capture both the increased stiffness at high strains, which leads to faster relaxation in the short-term response, as well as decreased stiffness at low strains, which leads to slower relaxation in the long-term response. This modification of the standard Maxwell description led to an accurate description of tissue behavior without increasing the number of elements and parameter estimate uncertainty. A measure of accuracy of the description is the normalized root mean squared error (NRMSE), for the modeled presented here the NRMSE averaged between all samples is 0.0222 for the exponential spring estimation step and 0.0377 for the entire stress-relaxation curve (**Figure 3.10**, in the APPENDIX, shows experimental data and model description for a representative sample).

Our analysis revealed differences in c_b for the trigone region compared to all other regions of the bladder, suggesting that the trigone region sees rapid increase in stress at high levels of strain (**Figure 3.8**). These results, once again, support what has been previously shown in the porcine bladder [7,8]. Few differences are seen in the viscoelastic parameters for the location-specific experiment, suggesting that most regions of the bladder show similar time-dependent behaviors. Differences in the largest time constant ($\bar{\tau}_3$) are observed, however, when comparing the trigone region to dorsal and lower body regions. This would imply a difference in the long-time viscoelastic response of the trigone region. This difference could be a significant factor when attempting to evaluate elastic behavior with conventional repeated, low-strain rate tensile tests, and should be acknowledged and considered when developing a testing protocol.

No differences are seen between the material parameters estimated for samples tested in solutions of osmolarity 100, 300, and 600 mOsm/L. Knowing that tissue swelling is significantly dependent on solution osmolarity (as shown in **Figure 3.5**), the absence of differences between these parameters suggests that the bladder wall mechanics is somewhat independent of the changes

in swelling within this range of osmolarities. However, samples tested in a 900 mOsm/L solution show significantly greater values of c_a , η_3 , and $\bar{\tau}_3$ when compared to all other testing solutions (**Figure 3.9**). This is especially significant because the long-time response of the tissue, which is the most physiologically relevant in the bladder because of the timescale of normal micturition, depends heavily on η_3 and $\bar{\tau}_3$. The increase in stress associated with higher long-time parameter values suggests, in agreement with the conclusions from the experimental data, that pathologically high urine osmolarity together with decreased efficacy of urothelial barrier may contribute to increased stresses felt by cells in the bladder wall, and consequently act as a contributing factor in driving remodeling.

3.4.4. Limitations

The swelling and mechanical test protocols employed here have some limitations. Relative masses and volumes for the 300 mOsm/L samples are greater than 1, as shown in **Figure 3.5**. This could suggest that the time considered for acclimation for the swelling test (18 hours) is not long enough for the samples to reach swelling equilibrium. Additionally, swelling was performed at 2 °C, as opposed to room temperature or *in vivo* body temperature. This was a necessary limitation, in the effort to minimize the effect of tissue degradation and to limit the amount of time needed to complete all swelling and stress-relaxation testing for a single bladder. Furthermore, a somewhat large amount of uncertainty can be seen in the volume estimation for the swelling experiment when compared to the mass data (see **Figure 3.5**). This is because the volume estimation was made using only a top and side-view image for every sample. To improve the accuracy of the volume estimation, images from more angles are needed. Moreover, the stress-relaxation tests in this study were performed without preconditioning. Hardware limitations prevented preconditioning from being performed at a displacement rate lower than the rate used for step-straining (50 mm/s).

Therefore, it was deemed more reasonable to not precondition the tissue. Furthermore, a prior study has shown that muscle and fiber reorganization and reorientation occurs during bladder filling that is revolved back to a reference state during contraction [86]. Thus, it is unclear whether the *in vivo* passive mechanical response is more closely correlated with preconditioned or non-preconditioned *in vitro* tissue response. Finally, the variable-osmolarity stress-relaxation experiment showed some inter-animal variability when analyzing the experimentally measured peak and relaxed stresses, this difference however was not observed in the modeling parameters.

The stress relaxation model generally provided a good description of the mechanical data, but falls short in some regards. The multi-step parameter estimation process restricts the relaxed stress of the model to be represented by the final stress values of the data in each straining step. This assumes that the final stress values in the data represent the fully relaxed stress of the tissue, which may not be the case for some samples. This could introduce error into parameter estimates. However, preliminary analysis showed that an unrestricted parameter estimation procedure (single step) resulted in higher uncertainty in parameter estimates. Similarly, the choice of c being equal for all modified Maxwell elements is a limiting assumption that was necessary to obtain parameter estimates that converged to unique values. Additionally, the model was unable to accurately capture the strain dependence of the stresses near the peaks. It is unclear whether this is a limitation of the model or of the data collection near the peaks. It has been shown that short-time response data directly after rapid straining is subject to elevated measurement error [21,143].

3.5 Conclusions

In this study we found that the uniaxial viscoelastic behavior of the urinary bladder significantly depends on both anatomical location and solution osmolarity. This information is crucial to inform the development of both new therapeutics as well as aid in the future design of tissue engineered

biomaterials. Moreover, these results will be useful in aiding the design of testing protocols for future studies. Yet, there are still unanswered questions that should be explored in the future. For example, it has been shown before that the quasi-static mechanical characteristics of the bladder are anisotropic. Therefore, performing biaxial stress-relaxation tests will increase our understanding of how viscoelastic behavior change with tissue directionality in the bladder wall. Moreover, the difference in mechanical behavior due to osmotic loading may be related to a change in collagen fibers network organization associated with hydration, which has not been explored in this work. A study that correlates microscopy with stress-relaxation could shed light on this correlation.

APPENDIX

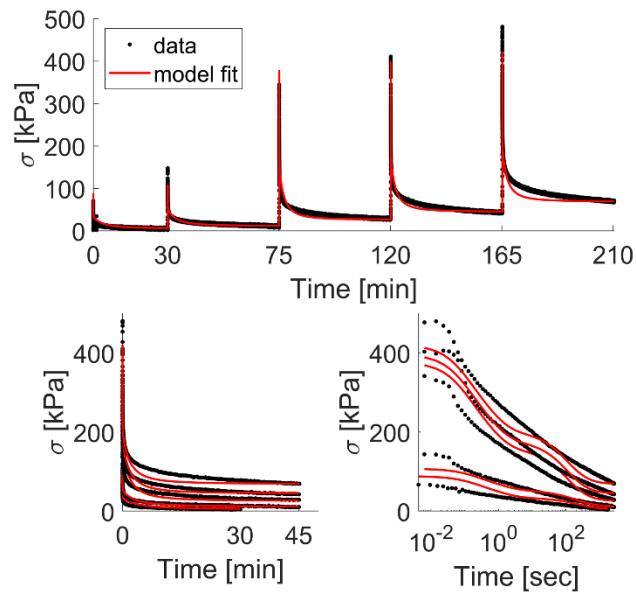


Figure 3.10 Model description for a representative dataset. All plots show the same experimental data (solid circles) and model description (solid line), each with a different timescale representation. The top represented the consecutive loading steps as a function of testing time. The bottom figures represent the loading steps as a function of time relative to the start of each loading step shown for a linear timescale (left) and logarithmic timescale (right). The normalized root mean squared error (NRMSE) averaged between all samples is 0.0222 for the exponential spring parameter estimation step and 0.0377 for the entire stress-relaxation curve.

CHAPTER 4 - CHANGES IN MORPHOLOGY AND COMPLIANCE IN THE LONG-TERM SPINAL CORD INJURED RAT BLADDER EXTRACELLULAR MATRIX

4.1. Overview

SCI has been shown to alter muscle stiffness [144] and overall thigh tissue stiffness [145] in humans. Bladder wall morphology and mechanical properties have been shown to change in as a result of a SCI. This has been shown in the past in a rat bladder model of SCI [14,21,30,31]. In the healthy rat bladder, smooth muscle cells have been shown to be oriented predominantly in the longitudinal direction, in contrast to the SCI rat bladder which shows SMCs oriented both longitudinally and circumferentially [22]. SCI rat bladders have also shown decreased collagen content and increased elastin content compared to controls [21]. In addition, compliance of the rat bladder wall has been shown to increase 10 and 14 days post-injury [30], increase 3 and 6 weeks post-injury, but return close to normal levels of compliance 10 weeks post-injury [31]. Finally, viscoelastic response of SCI rat bladders have been shown to differ from controls [21,62]. There is evidence of *de novo* elastin fibers in the SCI rat bladder, which are posited to play a role in crimping the collagen fiber network, thus changing the recruitment of collagen fibers during tissue deformation, and increasing compliance [14].

The objectives of this study are to quantify the enduring changes in morphology and mechanical properties of the rat bladder after SCI. To date, the longest evaluation of mechanical properties in the SCI rat bladder post-injury previously published is 10 weeks [31]. In this study, we evaluate mechanical properties of the SCI rat bladder extracellular matrix (ECM) 16 weeks post-injury. Through imaging, histological analysis, tensile testing, and constitutive modeling, we are able to see increase in bladder circumference, elastin content, and distensibility. These results suggest increased bladder capacity and compliance in long-term spinal cord injury. Constitutive

modeling suggests that increased distensibility is facilitated by an increase in fiber waviness that alters the distribution of fiber recruitment during loading. This is supported by the highly coiled structure of collagen fibers in the remodeled extracellular matrix of short-term spinal cord injured rat bladders. These study in an important step in understanding the remodeling of the spinal cord injured bladder, which has implications for future treatment and care in long-term spinal cord injury.

4.2. Methods

4.2.1. Animal groups and tissue preparation

In this study, groups included SCI paraplegic (P, n=8), healthy age-matched controls (C, n=6), and sham surgery controls (S, n=7), all male Sprague-Dawley rats. 8-week old rats underwent SCI surgery to induce paraplegia (n=8), as described in [146]. Rats were anesthetized and the spinal cord was transected between T2–3 using a microknife (10316- 14, Fine Science Tools) and Vannas spring scissors (15000-08, Fine Science Tools). After surgery, animal bladders were voided manually every four hours for 7-10 days, at which point partial ability to void independently was gained and bladders were voided four times per day to empty residual urine volume to prevent risk of infection. Animals were sacrificed 16 weeks post-injury. Healthy controls were age matched. Sham surgery controls underwent the same surgical procedure, but the spinal cord was left intact. After sacrifice, the bladders were excised and 2 circumferential rings were cut from each bladder. Samples fixed for ring histology (See section 2.3.1. *Ring histology*) were fixed fresh, while all others were frozen in tissue embedding medium at -80°C.

Since the objective of this study is to identify differences due to SCI in bladder ECM, we performed a decellularization protocol on the tissue to eliminate the mechanical contribution of

the SMCs. Prior to all testing procedures (excluding ring histology), bladder rings were thawed for 1 hour at room temperature, then decellularized following a protocol similar to what has previously been used for whole hearts [147] and bladders [14,62] from rats, which showed no adverse effects on ECM integrity. Briefly, rings were submerged in 5 mL of heparinized saline solution for 15 minutes, 5 mL of 1% sodium-dodecyl sulfate solution for 48 hours, 5 mL of deionized water for 15 minutes, and finally 5 mL of 1% Triton X-100 solution for 30 minutes.

4.2.2. Geometry estimation

Top-view images of rings were taken (Dual Pixel 12MP OIS – F1.7) before and after decellularization. NeuronJ [148], a plugin for ImageJ, was used to trace the inner and outer edges of the rings. Then, inner and outer tracing lengths were averaged to estimate effective ring circumference for each sample.

4.2.3. Histology

Bladder rings from 16-week paraplegic and control animals were processed for histological analysis. Samples were submerged in 10% formalin solution for 96 hours, and stored in 30% ethanol. Samples were embedded in paraffin, sectioned and stained by the Michigan State University Investigative Histopathology Lab. Samples were stained with picrosirius red (PSR) and Verhoeff-Van Gieson (VVG). Samples were imaged with an Olympus BX41 microscope using Nikon DXM1200 software.

In addition, samples from a subset of rats, which underwent the same SCI procedure but died unexpectedly 1 week after the procedure (n=2), were used for planar histology. After isolating bladder rings as described above, the tissue was decellularized, cut, laid flat, pinned to wax blocks, submerged in 10% formalin solution for 96 hours, then stored in 30% ethanol. Samples were embedded in paraffin, sectioned and stained by the Michigan State University Investigative

Histopathology Lab. Sectioning was performed normal to the radial direction. Two sections were taken from each sample, one as close to the inner surface as possible (lamina propria region), and one from the center of the wall thickness (detrusor region). Samples were stained with VVG. Imaging was performed with a Nikon Eclipse TI2-E. Automated axis movement and stitching was used to produce whole-sample images for the lamina propria and detrusor layers for each sample. Control rats ages 16 weeks (n=3) and 12 weeks (n=1) were also analyzed in the same fashion for comparison.

OrientationJ (ImageJ plugin) was used to analyze fiber orientation in the planar histological images. To remove artifacts from pinning and sample edges, two cropped sections were chosen from each image, which represented the largest regions devoid of sample edges or pinning. OrientationJ calculates local orientation and isotropic properties (coherency and energy) for every pixel in an image [84]. By default, OrientationJ creates a weighted histogram using coherency values to weight the orientation at each pixel. Coherency weighting gives high weight to areas of absent muscle cells (removed during decellularization) as well as highly collagenous areas, whereas weighting based on energy or pixel intensity only gives high weight to highly collagenous areas. For each group, local directions were weighted both with coherency, and the product of energy and pixel intensity. This allows orientation distributions to represent a combination of muscle and collagen fiber directions (coherency weighting), as well as only collagen fiber directions (energy×intensity weighting).

4.2.4. Mechanical testing

Uniaxial ring testing was performed on decellularized bladder rings. Samples were mounted to a custom uniaxial tensile testing machine via polyester thread loops. Force was measured with a 250-gram capacity load cell (Futek, LSB 200, 250 g, JR S-Beam Load Cell). Stretch was

continuously recorded throughout the tests with a charge-coupled device (CCD) camera (Basler, piA1000-60gm). Samples were submerged in modified Krebs-Henseleit buffer solution (Sigma-Aldrich, without calcium chloride) throughout testing. Prior to preconditioning, a 2-gram preload was applied and maintained for 10 minutes. Prior to each subsequent loading-unloading protocol, a 2-gram preload was reapplied and maintained for 1 minute. After each preload, front-view images (Basler, piA1000-60gm) and side view images (Dual Pixel 12MP OIS – F1.7) were taken. Samples were, first, preconditioned for 10 cycles of loading-unloading to a maximum stretch of 1.1, then we performed three cyclical testing protocols, each consisting of 5 cycles of loading-unloading to maximum stretches of 1.2, 1.3, and 1.4, respectively. Both preconditioning and testing cycles were performed at a rate of 0.01 s^{-1} . Reference configuration for stretch was sample length following applied preload. Mechanical tests were stopped if samples ruptured. All data analysis related to the mechanical testing, including model parameter estimation, was performed on the final loading cycle from the first loading set to surpass 120 kPa. Stress, σ , as a function of stretch, λ , was defined as follows,

$$\sigma(\lambda) = F(\lambda)/A_i(\lambda), \quad (4.1)$$

where F is the measured force, and A_i is the cross-sectional area calculated for the relevant loading step, given by,

$$A_i(\lambda) = A_i^0/\lambda, \quad (4.2)$$

where A_i^0 is the initial cross-sectional area, calculated from front and side-view images taken prior to the relevant loading protocol. Images were converted to binary images using manual thresholding. Sample width and thickness were defined as the median sample width and thickness from the binary front and side-view images. Initial cross-sectional area, A_i^0 , was calculated as the product of median width and thickness.

Opening angle experiments were also performed on decellularized bladder rings. Rings were placed in petri dishes and submerged in modified Krebs-Henseleit buffer solution. The bladder wall was cut, and images were taken at 0, 3, 6, 9, 12, 15, 30, 45, 60, 75, and 90 minutes post-cutting. After converting images to binary via manual thresholding, an ellipse was fit to every image. Opening angle was defined as the minimum angle formed by the two points at the opening, and a third point along the fitted ellipse.

4.2.4. Constitutive modeling

Two constitutive models were used to describe the uniaxial mechanical data. First, a structural fiber recruitment model was used to gain insight into potential microstructural differences responsible for changes in mechanical behavior. Second, an exponential model was used to provide a classical continuum mechanics description of the mechanical properties.

4.2.5.1. Fiber recruitment model

In this study, a structural unidirectional fiber recruitment model was used to describe the mechanical response of the bladder tissue. **Figure 4.1** shows a conceptual depiction of the fiber recruitment model, where springs in the model are linear, and representative of collagen fibers in the bladder tissue. As the tissue is stretched, springs engage and increase the stiffness of the response. When the number of springs is large, it is assumed that the percentage of engaged springs follows a scaled cumulative beta distribution, similar to [149]. The stress-stretch response of the model is defined by the following differential equation,

$$\frac{\partial \sigma}{\partial \lambda} = (E_1 - E_0)\psi_{cdf}(\lambda^*; \alpha, \beta) + E_0 \quad (4.3a)$$

$$\lambda^* = \frac{\lambda - 1}{\lambda_{max} - 1}, \quad (4.3b)$$

where E_0 and E_1 are the initial and final slope of the stress-stretch curve, respectively, and ψ_{cdf} is the beta distribution, which is a function of shape parameters α and β , and the normalized stretch λ^* is defined as a function of λ_{max} , the maximum stretch achieved during the test. The mean and variance of the beta distribution, λ_m^* and $[\lambda_{sd}^*]^2$ are defined as

$$\lambda_m^* = \frac{\alpha}{\alpha + \beta} = \frac{\lambda_m - 1}{\lambda_{max} - 1} \quad (4.4)$$

$$[\lambda_{sd}^*]^2 = \frac{\alpha\beta}{(\alpha + \beta)^2(\alpha + \beta + 1)} = \left[\frac{\lambda_{sd}}{\lambda_{max} - 1} \right]^2, \quad (4.5)$$

where λ_m and λ_{sd} are the mean and standard deviation of recruitment stretch, as seen in [101,149].

Parameter estimation was performed in several steps (see **Figure 4.2**). We estimated the initial slope, E_0 , as the slope of the line with the highest R^2 value when fitting a line to the first n points of the stress-stretch curve, where n was varied from 5 points to the total number of points on the curve, similar to [9]. E_1 was estimated in the same way, but using the final n points of the stress-stretch curve. Next, we defined λ_m as the stretch at the intersection of the initial and final slope lines. Using Equation (4.4), α was defined as a function of λ_m^* and β . Using the entire stress-stretch curve, we estimated β (*nlinfit*, MATLAB) by minimizing the sum of squared error (SSE) between the data and the stress-stretch relationship from Equation (4.3a), which was solved numerically using the *ode45* function in MATLAB.

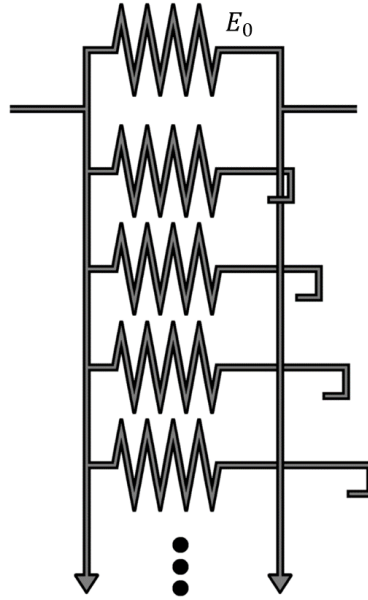


Figure 4.1 Visual representation of the fiber recruitment model. As deformation is applied, springs engage, increasing the stiffness of the response.

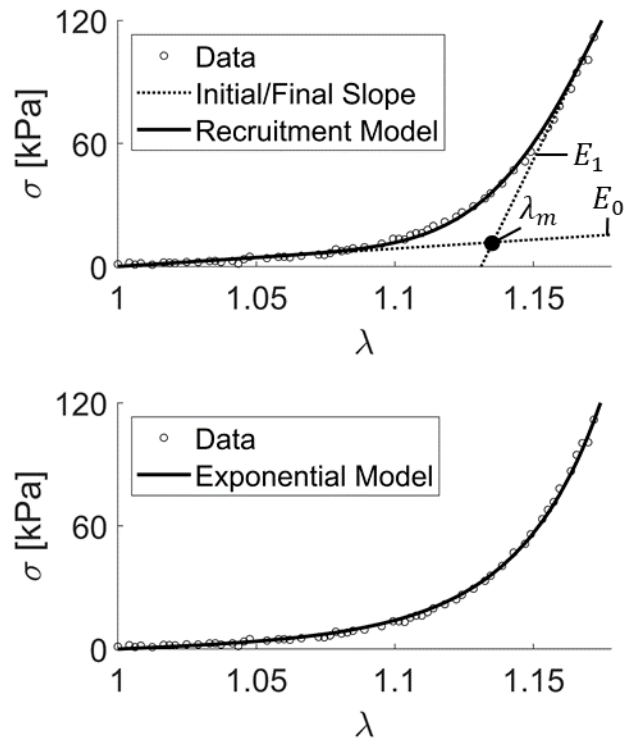


Figure 4.2 Representative stress-stretch data with model fit from the fiber-recruitment model (top) and exponential continuum model (bottom). For the fiber-recruitment model, E_0 is initial slope, E_1 is final slope, and λ_m is the mean recruitment stretch defined by the intersection of the initial and final slope lines.

4.2.5.2. Exponential model

In this study, we employ a constitutive model similar to what has been previously published [150–152]. Uniaxial deformation is described by the deformation gradient tensor, $F = \text{diag}(\lambda_1, \lambda_2, \lambda_3)$, where λ_1 , λ_2 , and λ_3 are the principal stretch directions, defined as $\lambda_1 = \lambda$, and $\lambda_2 = \lambda_3 = 1/\sqrt{\lambda}$. The strain energy function for this model is defined as

$$W(\mathbf{C}) = \frac{c_1}{2} (e^{c_2(\text{tr}(\mathbf{C})-3)} - 1) \quad (4.6)$$

where $\mathbf{C} = \mathbf{F}^T \mathbf{F}$ is the right Cauchy-Green deformation tensor, and c_1 and c_2 are scale and shape parameters, respectively, with units of stress and dimensionless. Cauchy stress, \mathbf{t} , is calculated as

$$\mathbf{t} = -p + 2\mathbf{F} \frac{\partial W(\mathbf{C})}{\partial \mathbf{C}} \mathbf{F}^T \quad (4.7)$$

where p is a Lagrange multiplier to enforce incompressibility. We performed parameter estimation in a single step (using the function *nlinfit* in MATLAB) by minimizing the SSE between the stress-stretch experimental data and the Cauchy stress defined in Equation (4.7).

4.2.6. Statistical analysis

We performed statistical analysis to assess significance between groups for ring circumference, stretch values at various levels of stress, stretch at 100kPa stress (comparable to axial stretch in [31]), parameter values for both models, and opening angle. The source of variation for all ANOVAs performed was injury (control, sham, paraplegic). For the mechanical data, each curve was reduced to 12 points, corresponding to the level of stretch for given values of stress, σ_j . Repeated measure ANOVAs were performed for ring circumferences, stretch values at σ_j , and opening angles, where the within-subject variables were thawed vs decellularized, stress level (σ_j), and time, respectively. 1-way ANOVAs were performed for stretch at 100kPa stress, and parameter values for both models. Post-hoc analysis consisted of Tukey-Kramer multiple

comparisons tests for all pairwise multiple comparison procedures. Due to lack of significance between control and sham groups for mechanical data and model parameters, control and sham groups were combined, and additional repeated measure ANOVAs and 1-way ANOVAs were performed for stretch at σ_j , stretch at 100kPa stress, and parameter values for both models.

4.3. Results

4.3.1. Ring circumference

Figure 4.3 shows mean \pm standard deviation of effective ring circumference of each group before and after decellularization. Ring circumference increased statistically through the decellularization process ($p < 0.05$). Both sham and paraplegic groups appear to have larger ring circumference than control samples, also confirmed by statistical analysis ($p < 0.05$).

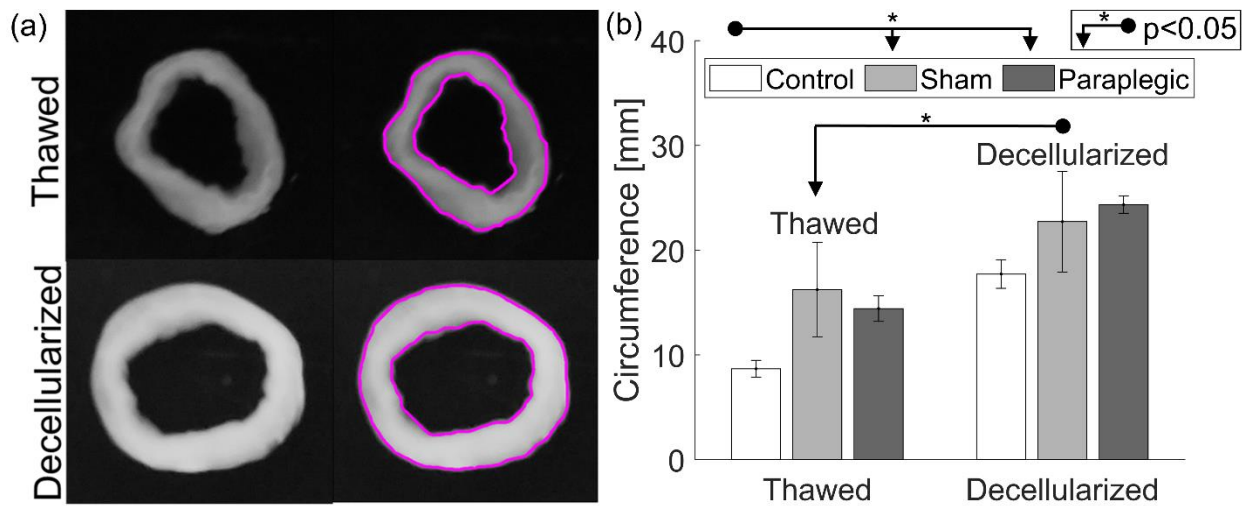


Figure 4.3 (a) Ring images before and after decellularization and traced edges, and (b) mean \pm standard deviation for ring circumference before and after decellularization for control, sham, and paraplegic groups.

4.3.2. Histology

Figure 4.4 shows PSR and VVG stained images of different layers from control and paraplegic bladders (plane normal to the longitudinal axis). Qualitatively, paraplegic bladders tended to have

more visible elastin fibers than controls. **Figure 4.5** shows some particular regions of interest from paraplegic histological samples, where high collagen density and abnormal amounts of elastin can be seen.

Figure 4.6 shows planar images (normal to the radial direction) from decellularized control and 1-week paraplegic bladders. The morphology of the collagen fibers varies from lamina propria to detrusor in controls, and varies from controls to paraplegic bladders. **Figure 4.7** shows mean orientation distributions from control and 1-week paraplegic bladders in different layers, with local orientations weighted by either coherency or the product of energy and pixel intensity. Coherency weighting gives similar weight to collagenous areas and muscular areas with lower amounts of collagen. Weighting by energy and pixel intensity decreased the weight of muscular areas and increases the weight of collagenous regions. It should be emphasized that by “muscular areas” we are referring to regions that contained smooth muscle cells prior to decellularization, which can be seen in the detrusor region images of **Figure 4.6**.

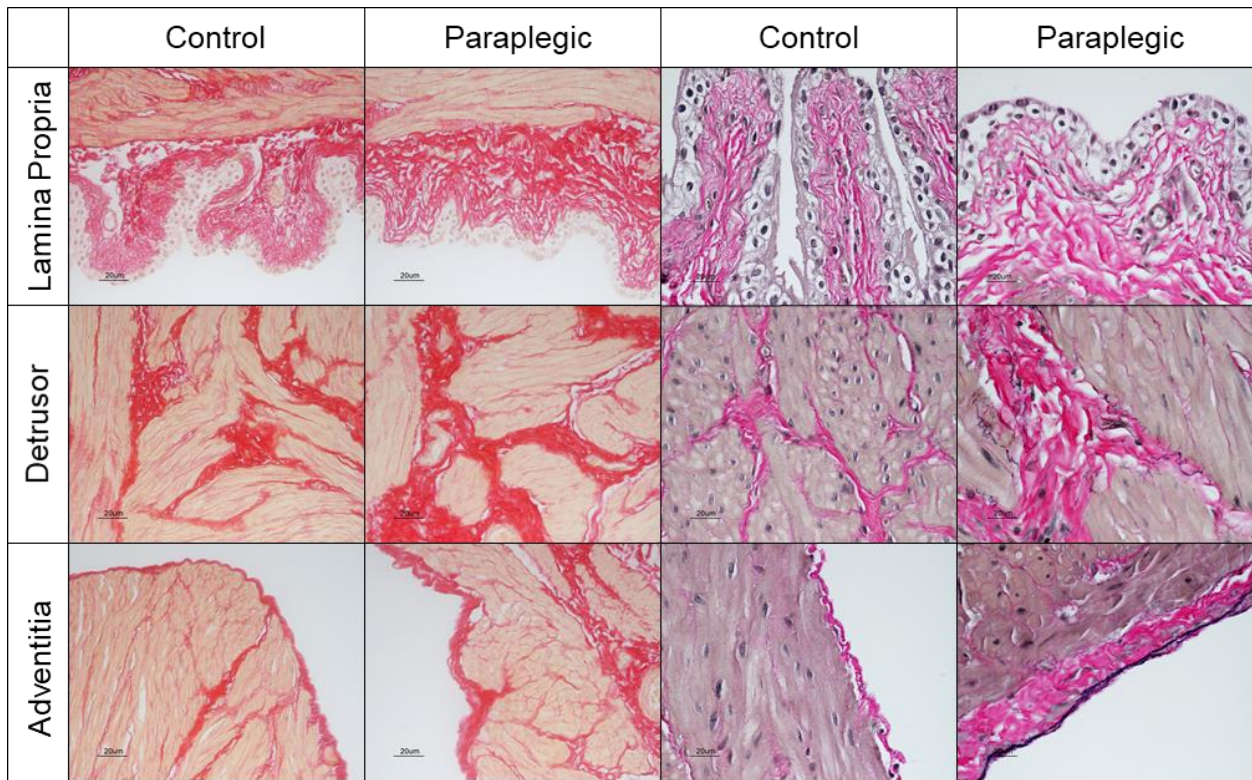


Figure 4.4 PSR (left two columns) and VVG (right two columns) stained bladders in the plane normal to the longitudinal direction from control (left) and paraplegic (right) rats in the lamina propria (top), detrusor (middle), and adventitia (bottom)

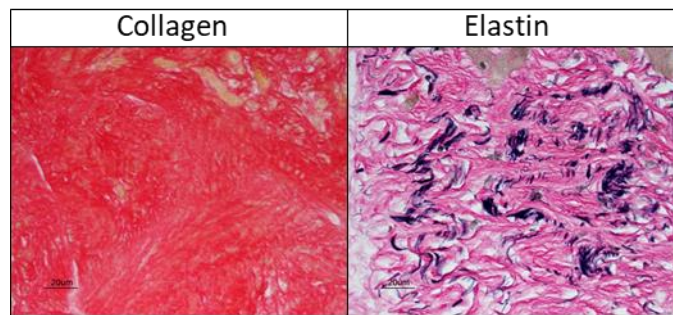


Figure 4.5 Regions of interest from a 16-week paraplegic rat bladder showing an area of high collagen density (PSR, left) and high amounts of elastin (VVG, right)

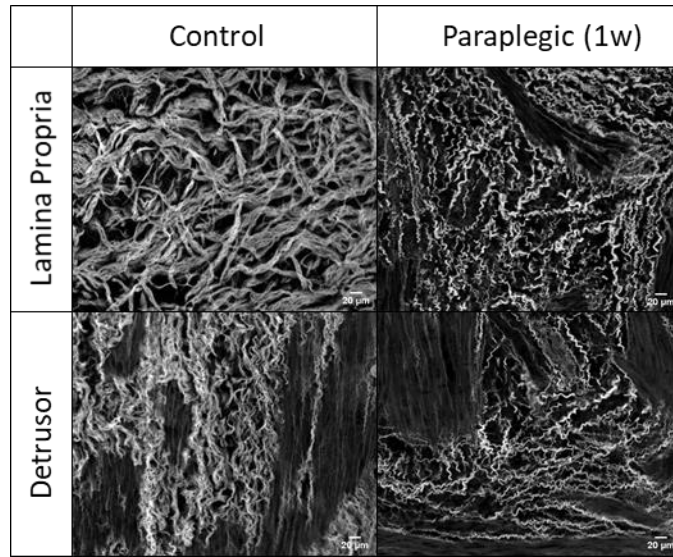


Figure 4.6 Planar images from control (left) and 1-week paraplegic (right) rat bladders in the lamina propria (top) and detrusor (bottom)

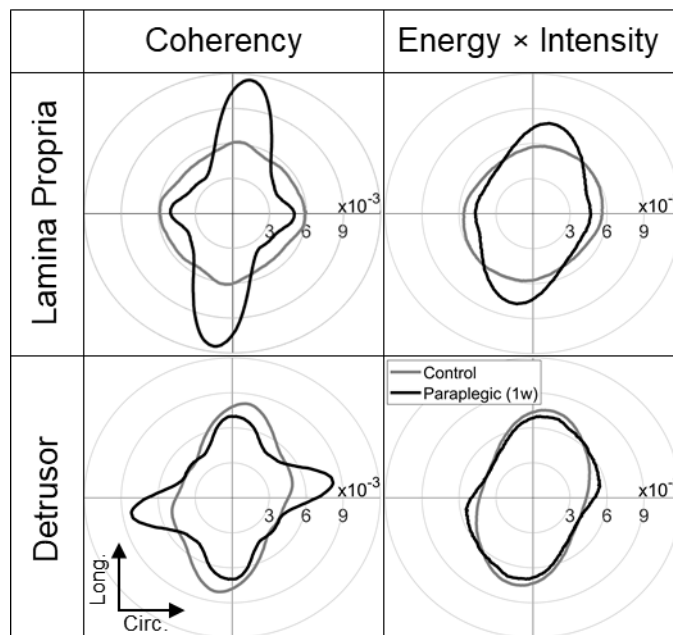


Figure 4.7 Mean fiber orientation distributions for control and 1-week paraplegic rat bladders in the lamina propria (top) and detrusor (bottom) with different local fiber angle weighting. Coherency weighting (left) give high weight to formerly muscular regions as well as collagenous regions. Weighting by the product of energy and intensity (right) gives lower weighting to previously muscular areas, while keeping high weighting in collagenous regions.

4.3.3. Mechanical testing

Figure 4.8 shows stress-stretch curves for each group averaged by stretch at different levels of stress. It can be appreciated that control and sham bladders have nearly identical average stress-stretch curves, confirmed by statistical analysis ($p=0.95$). Paraplegic mechanical data is significantly rightward shifted compared to sham ($p<0.05$) and compared to control and sham grouped together ($p<0.01$). **Figure 4.9** shows mean \pm standard deviation of stretch values at a stress of 100 kPa. This metric is similar to previous measures of compliance in the SCI rat bladder [31]. At 100 kPa, paraplegic bladders show significantly higher stretch than sham samples ($p<0.05$) and sham combined with control ($p<0.01$). Finally, **Figure 4.10** shows mean \pm standard deviation of opening angle at different time points post-cut for control and paraplegic groups. No statistically significant differences between groups were observed ($p=0.34$), yet the opening angle assumed values larger than zero in decellularized rat bladder rings.

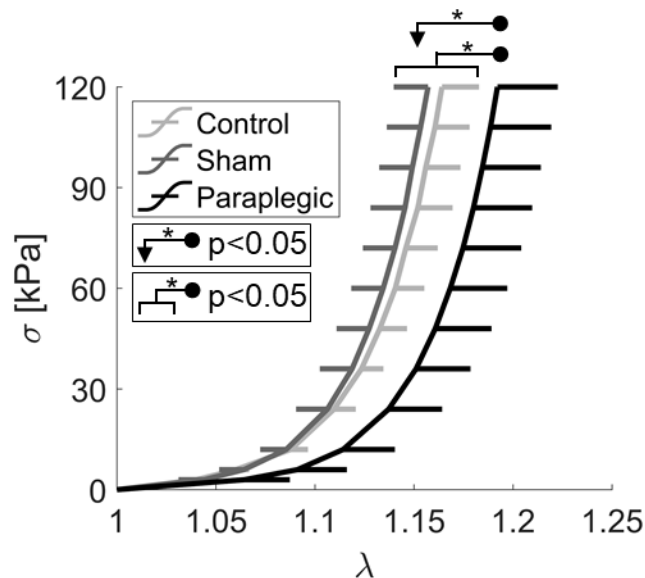


Figure 4.8 Stress-stretch curves (mean \pm standard deviation) from control, sham, and paraplegic groups. Stretch values at different levels of stress are significantly higher in the paraplegic group when compared to the sham group (arrow) and the sham and control groups combined (bracket).

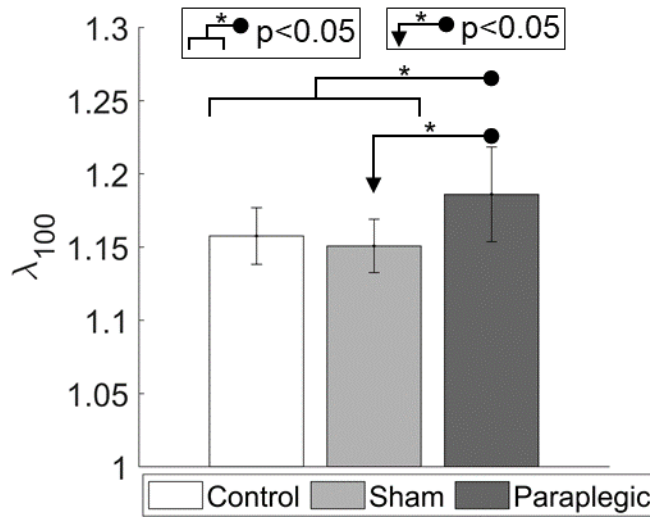


Figure 4.9 Mean \pm standard deviation of stretch values at 100 kPa stress for control, sham, and paraplegic groups. The paraplegic group shows significantly higher stretch than the sham group (arrow) and the sham and control groups combined (bracket).

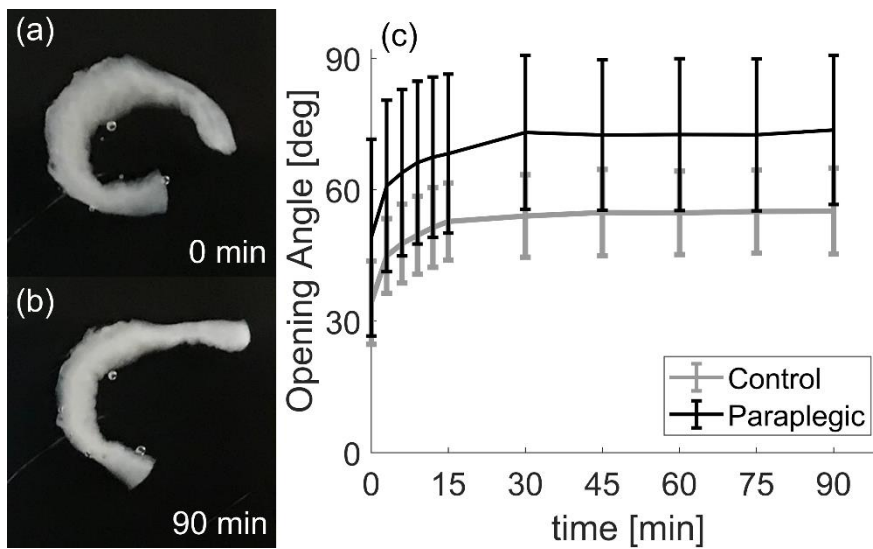


Figure 4.10 Opening angle images at (a) 0 minutes and (b) 90 minutes post-cut, and (c) mean \pm standard deviation of opening angle vs time from control and paraplegic groups

4.3.4. Constitutive modeling

Figure 4.2 shows a representative set of mechanical data with the model fit from both the fiber recruitment model and the exponential continuum model. The normalized root mean squared error (NRMSE) averaged between all samples is 0.014 for the fiber recruitment model, and 0.017 for the exponential continuum model.

Figure 4.11 shows mean \pm standard deviation of parameter values for both models. No differences were seen between control and sham groups for any parameters. When comparing all groups, paraplegic samples show significantly higher mean recruitment stretch, λ_m , than the sham group ($p < 0.05$). When combining the control and sham groups, paraplegic samples show higher mean and standard deviation of recruitment stretch, and lower initial slope when compared to the control+sham group. For the exponential continuum model, no differences are seen when comparing all groups, but c_2 is significantly lower in paraplegic compared the control+sham group.

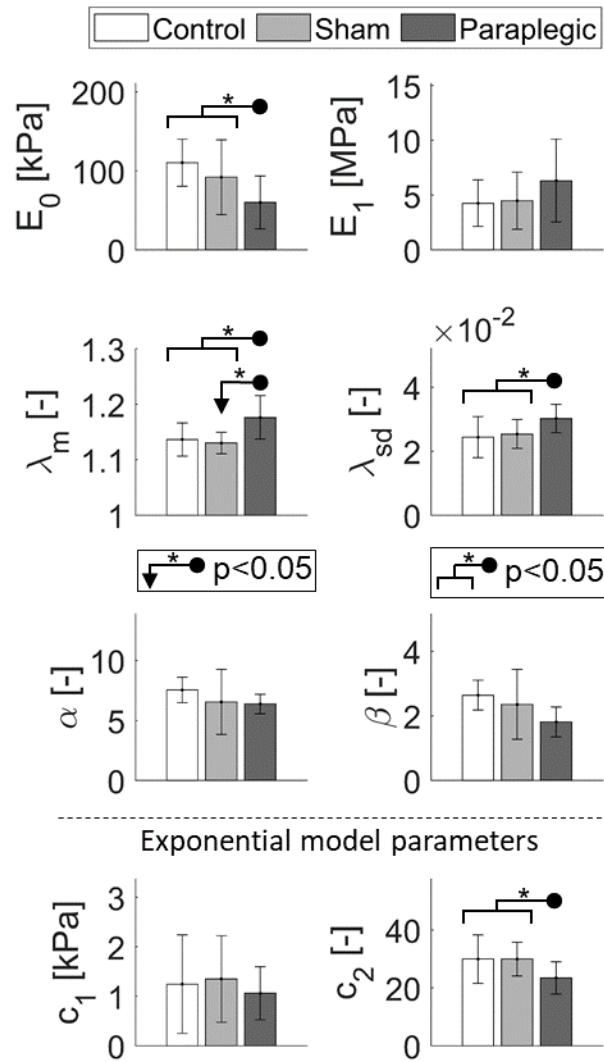


Figure 4.11 Mean \pm standard deviation parameter values for the fiber-recruitment model (E_0 , E_1 , λ_m , λ_{sd} , α , β), and exponential continuum model (c_1 , c_2)

4.4. Discussion

This study focuses on understanding the changes in ECM microstructure and mechanical characteristics in the bladder of an animal model of SCI, 16 weeks post-injury. We found that the mechanical behavior of the bladder's ECM in paraplegic animals is more distensible when compared to both control and sham animals. We have quantified this using two different metrics. First, when looking at the stress-stretch curves (**Figure 4.8**) the significant rightward shift observed between the tissue from sham and control groups and the SCI group suggests higher distensibility. Second, we calculated the stretch corresponding to a stress of 100 kPa (**Figure 4.9**), a measure of compliance used in prior work [31], which exhibited significantly higher values in samples from the SCI group as compared to sham and the combined sham and control group. Previous work showed that compliance is highest in bladder tissue 3-6 weeks post-injury in a rat model of SCI, and returns close to control levels of compliance at 10 weeks [31]. In [31], the authors speculated that this trend could lead to a hypocompliant bladder at a later time point, which would recapitulate what is observed in some individuals affected by SCI [153]. Our results show, however, that this is not the case after 16 weeks. Our work suggests that rather than fully returning to healthy levels of compliance or becoming less compliant than controls, the bladder of SCI rats 16 weeks post-injury remains at slightly elevated levels of compliance.

It is commonly accepted that collagen fiber recruitment is an important phenomenon in defining the mechanics of highly dynamic tissues such as the bladder. The wavy configuration of collagen fibers that is seen in many tissues allows tissue to deform with little resistance at low stresses, behavior observed in healthy bladders during low-pressure filling [9]. When collagen fibers begin to straighten, they engage and significantly contribute to increase the stiffness of the tissue overall. This correlation between microstructure and tissue behavior has been studied in

various tissues including rat tail tendon [77], rabbit achilles tendons [78,79], human skin [80], human vena cava [81], pig coronary adventitia [82], rabbit carotid arteries [83,84], pig thoracic aortas [85], and fetal bovine bladder [86]. In addition, changes in the microstructural organization of the collagen network, for example due to disease, could significantly impact the global mechanical behavior of the tissue. Cheng and colleagues were able, in a recent work, to measure collagen fiber waviness in the rat bladder at different amounts of strain. They reported experimentally that distensibility was decreased in samples that showed premature recruitment (i.e., earlier engagement) of fibers on the outer wall of the bladder, which seemed to be correlated with aging [9]. It is intuitive to expect that a delayed engagement in collagen fibers will result in increased distensibility of the bladder ECM network as a whole.

When direct measurement of fiber engagement during stretching is not available, several studies in the past have employed structural constitutive modeling to indirectly estimate the characteristics of the fibers network. Fiber recruitment models, first described by Viidik [78], specifically correlate fiber waviness and engagement and the mechanical behavior of tissue. Lanir developed the structural theory for fiber recruitment and orientation distributions for fibrous tissues [87,88] and later incorporated fiber recruitment in a growth and remodeling model [89]. Fiber recruitment models have been used in the past to describe rat carotid arteries [90] and right ventricular myocardium [149], rabbit skin [92], rabbit carotid arteries [83,91], sheep digital tendon [93,94], and SCI rat bladder [14]. Continuum models with exponential strain energy functions are also commonly used to describe the mechanical behavior of highly deformable tissues (i.e., bladders in pigs [69], dogs [71], and rats [9]).

In this study we have employed two constitutive models, one structural and one continuum, to quantify the changes in the ECM mechanical behavior in the bladder wall that are associated

with a SCI. Both the exponential continuum model and the structural fiber-recruitment model provided good descriptions of the bladder mechanical response (**Figure 4.2**). When comparing paraplegic to grouped control and sham, we observed a significant difference in the exponential continuum model parameter c_2 (**Figure 4.11**, bottom). This difference suggests a slower “ramp-up” of the stress-stretch curve in paraplegic samples. This behavior seems to be also supported by a decrease in initial slope E_0 in samples from paraplegic animals, suggesting a lower amount of initially recruited fibers. A possible explanation for this observed behavior was first proposed in [14]. Briefly, the authors suggested that the intertwining of collagen and *de novo* deposited elastin could lead to crimping of the collagen fibers, thus increasing compliance of the tissue [14]. In our study we observed an increase in recruitment distribution parameters λ_m and λ_{sd} in paraplegic bladders, while final slope E_1 was unchanged. These findings support the hypothesis that the increase in distensibility observed in bladder ECM from SCI animals as compared to controls and shams is not necessarily a result of changing fiber stiffness or quantity, but rather a change in configuration of the remodeled fiber network. The lack of differences in the distribution shape parameters α and β further suggest that the recruitment distribution does not change shape, but scales rightward, thus increasing λ_m and λ_{sd} without affecting the shape of the distribution.

To further investigate this hypothesis, we performed several imaging analyses on the bladder tissue collected from paraplegic and control animals. On the one hand, we observed no significant fibrosis, nor significant morphological differences in the collagen network between control or paraplegic bladders overall (**Figure 4.4**). Additionally, preliminary image analysis showed no differences in collagen or cellular area fractions between groups (data not shown). On the other hand, **Figure 4.4** highlights some qualitative differences between groups: bladders from paraplegic animals seemed to have higher amounts of visible elastin fibers throughout the tissue.

Furthermore, we have observed qualitative examples of highly localized remodeling. For example, **Figure 4.5** on the left shows an area of significant localized collagen remodeling in the detrusor of a SCI animal, and on the right shows a highly localized increase in elastin content in the tissue of a paraplegic animal. This finding is also in agreement with previous work showing that SCI leads to creation of *de novo* elastin fibers in rat bladders 3-4 weeks post- injury [14], and an increase in elastin/collagen ratio at 1.5, 3, 6, and 10 weeks post injury compared to controls [31].

Our analysis of planar histological sections (**Figure 4.6**) shows that in controls, collagen fibers in the lamina propria region appear thicker and more randomly oriented, whereas fibers between smooth muscle bundles appear thinner and wavier with orientations generally aligned with the direction of the muscle. It should be reiterated that these images are from decellularized samples, and areas referred to as muscle are regions where muscles were present prior to decellularization. In the 1-week paraplegic bladders, the collagen morphology appears starkly different from controls. Fibers generally appeared the same between the lamina propria and detrusor regions in the 1-week paraplegic samples. When comparing the detrusor region of controls and 1-week paraplegic, paraplegic fibers appear highly coiled, but with overall lower density of fibers than controls. Orientation analysis (**Figure 4.7**) reveals additional information in terms of remodeling of the ECM. When weighting by coherency, which is heavily impacted by orientations of previously muscular regions, the lamina propria shows mostly isotropic orientation in controls, but pronounced longitudinal orientation in 1-week paraplegic. When weighting by the product of energy and pixel intensity, which highlights collagenous regions and lessens the impact of previously muscular regions, the lamina propria shows even more isotropic distribution in controls, and a less pronounced but still preferential direction in the longitudinal direction for 1-week paraplegic. When looking in the detrusor region, controls show preferential orientation in

the longitudinal direction for both weightings. However, 1-week paraplegic samples show a high degree of bi-directional orientation with coherency weighting, but similar longitudinal preferential orientation to controls when weighting by the product of energy and pixel intensity. These results suggest that healthy rat bladders have randomly oriented collagen fibers in the lamina propria, a longitudinal preferential orientation of smooth muscle bundles in the detrusor, as well as intramuscular collagen fibers oriented similarly. Additionally, these results suggest that SCI in the short-term causes remodeling that leads to longitudinal preferential orientation of collagen fibers, and a bimodal distribution of smooth muscle bundles in the longitudinal and circumferential directions. These results are largely in agreement with previously published smooth muscle orientation distributions in healthy and SCI rat bladders [22].

We also observed some changes in the gross geometry of the bladder, both associated with surgery as well as with tissue treatment (i.e., decellularization). **Figure 4.3** suggests that long-term SCI leads to significant remodeling that results in an increase in bladder capacity compared to controls. We also observed an unexpected significant increase in bladder diameter between sham and control animals. A possible explanation for this is that the sham surgery may induce high levels of stress or anxiety in the animals, leading to bladder dysfunction. It has been shown previously that social stress can lead to altered micturition patterns and bladder capacity in mice which could lead to bladder remodeling [154]. The bladder circumference also increases significantly after the decellularization process. As smooth muscle is intertwined with collagen fibers [86], it is expected that removing smooth muscle cells would alter the zero-load reference state of the bladder ECM. Moreover, choice of reference configuration can significantly affect evaluated mechanical properties of soft tissues [14]. This highlights the importance of considering the impact of reference configuration on reported mechanical properties. This is especially vital in

the field of tissue engineering, where it is desired for tissue engineering scaffolds to replicate mechanical functions of the native tissue ECM [155]. When designing scaffolds, it is important to consider whether to match mechanical properties based on pre or post decellularization reference configuration.

Finally, we report for the first time the existence of a residual stress distribution with the bladder wall. The opening angle tests we performed (**Figure 4.10**) show that both control and paraplegic bladder ECM have a positive value of opening angle 90 minutes after the cut. These results also show that the opening angle increases with time after the cut, but is significantly different than 0 even at the time of cut for all sample. At the same time, preliminary tests of control intact tissue showed no opening angle (data not shown). This suggests that the rat bladder ECM may have a residual stress distribution which can be appreciated after decellularization.

4.5 Limitations

A potential limitation of the comparisons between this study and previously published studies on SCI rat bladders is that differences in surgical protocol (i.e., location of transection) and post-operative care protocol (i.e., frequency of manual bladder voiding) between studies could be confounding factors.

Bladder samples for mechanical testing were frozen prior to decellularization and testing. Testing tissue fresh is preferred, but not always logistically possible. Several studies have evaluated the effect of freezing tissue using similar protocols to this study and found little impact on mechanical response [156]. Similarly, we found no evidence of compromised extracellular matrix components after decellularization, supported by previous studies that have used similar decellularization methods [14,62,147]. Because we are using our parameter estimates comparatively within the

study on samples subjected to identical protocols, any small alterations in ECM integrity would be universal, likely mitigating the effect on the significant differences observed.

Uniaxial testing was performed in this study, whereas biaxial testing would have allowed closer comparison of mechanical data from previously published studies on the SCI rat bladder [30,31], and allow for anisotropic behavior to be evaluated. Because of the drastic differences observed in fiber morphology and orientation in short-term SCI in this study, it is necessary to perform similar evaluations on long-term SCI tissue in the future, along with biaxial mechanical characterization. Additionally, some of the residual stress measured through opening angles could be due to swelling of the ECM during decellularization, as osmotic swelling has been shown to increase opening angles in other tissues [157].

While we were able to see a qualitative increase in elastin content with long-term SCI, it would be beneficial to quantify this in future studies to compare to previously reported increases in elastin/collagen ratio in the SCI rat bladder [30,31]. The 1-week paraplegic bladder samples used for planar histology were from rats that died unexpectedly. Because the cause of death is unknown, it is not clear whether the bladders represent normal 1-week SCI rat bladders. Independently of this fact, the results shown highlight the extreme remodeling capabilities of the bladder in pathological conditions.

4.6 Conclusions

In this study we found that SCI rat bladder ECM 16 weeks post-injury is more compliant than healthy bladder ECM. This represents the longest time post-injury the mechanical behavior of the SCI rat bladder has been evaluated, to date. We have shown the extreme remodeling capabilities of the bladder in these pathological conditions. Constitutive modeling suggests that the increase in

compliance could be related to a change in recruitment distribution of collagen fibers during loading, potentially facilitated by crimping of the ECM resulting from increased elastin fiber content, as previously postulated [14]. These findings are important in terms of understanding the remodeling of the SCI bladder, which has implications for future treatment and care in long-term SCI.

APPENDIX

Table 4.1 Parameter estimates for the fiber recruitment and exponential continuum models for all samples

	E_0 [kPa]	E_1 [kPa]	λ_m	λ_{sd}	α	β	c_1 [kPa]	c_2
Control	149.4	6785.3	1.121	0.021	7.24	2.31	0.99	39.8
	66.1	2381.9	1.123	0.023	6.88	2.62	0.75	30.7
	111.1	2513.9	1.117	0.021	7.57	2.75	0.80	33.3
	126.7	4176.0	1.127	0.021	9.57	3.51	0.99	31.9
	87.0	2751.7	1.135	0.023	7.48	2.36	0.69	29.5
	122.3	6954.0	1.196	0.037	6.53	2.31	3.27	14.5
Sham	111.9	2911.5	1.122	0.026	4.88	1.74	1.39	27.3
	33.5	3982.9	1.135	0.029	4.47	1.39	0.90	29.8
	55.1	2078.6	1.134	0.022	9.93	4.11	0.68	26.7
	179.5	5192.8	1.108	0.025	3.72	1.19	1.72	36.3
	79.0	9973.8	1.167	0.033	6.22	2.28	3.12	20.0
	106.3	3611.1	1.130	0.019	10.66	3.47	0.62	34.5
	78.5	3675.6	1.113	0.023	5.98	2.31	1.02	35.1
Paraplegic	19.8	4113.5	1.224	0.035	7.02	1.66	0.53	17.3
	21.7	9030.0	1.228	0.035	5.60	1.01	0.63	19.6
	46.8	4477.2	1.187	0.034	5.84	1.64	0.98	19.5
	58.4	4337.4	1.130	0.026	5.86	2.05	1.01	31.0
	51.9	8640.9	1.185	0.033	7.37	2.52	2.17	18.6
	73.9	3010.8	1.130	0.024	6.48	2.21	0.77	30.5
	115.9	13752.4	1.186	0.029	7.48	1.89	1.50	23.5
	93.1	3251.2	1.140	0.026	5.46	1.52	0.90	27.3

CHAPTER 5 - CONCLUSIONS AND FUTURE WORK

5.1 Conclusions

The work presented in this dissertation highlights some key aspects of bladder mechanics. We first compared the mechanical characteristics of human and pig bladders and found the differences appear to stem more from amorphous matrix and low-stress SMC behavior, with little difference between high-stress orthotropic behavior. This supports the use of the pig bladder ECM in tissue engineering of the human bladder, and more generally the use of the pig bladder as a model of the human bladder in the field of tissue mechanics. Thus, we decided to use porcine bladder tissue to investigate how swelling due to inflammatory response or urothelial dysfunction can affect bladder mechanics. This is important considering it is commonly accepted that altered stress states in biological tissue generally lead to remodeling. We have shown that osmotic swelling is a factor that can alter the stress state of the bladder, and may be a contributing factor in driving remodeling. This highlights the importance of maintaining healthy and functioning urothelium. Finally, while our results support the use of porcine tissue as a model for the human bladder, this may not be possible for every study. For example, when studying enduring effects of spinal cord injury (SCI) on bladder functionality, the use of a large animal model may be not feasible due to the expense and the time requirements. For this reason, we have employed a small animal (rat) model of SCI to show that long-term SCI leads to significant remodeling of the bladder wall that leads to increased capacity and compliance. We have shown that the bladder remodels not only the amount of collagen, but also the morphology of the individual fibers and the direction of collagen fibers and SMC bundles.

5.2 Future work

There is still much to learn about the mechanics of the bladder. An important step in relating *in vitro* mechanical data to *in vivo* cytometric data is a better understanding of the effect of muscle contractions on the configuration of the ECM. Knowing that fiber realignment occurs during bladder filling [158], and that contraction occurs after every filling cycle in a healthy bladder, it is possible that contraction plays a role in resetting the ECM configuration to its original state. *In vitro* mechanical testing of bladder tissue is generally performed with multiple loading and unloading cycle without contraction. Future work should address this question to determine whether preconditioned passive properties are comparable to post-contraction loading.

While several studies have addressed the effect of SCI on the mechanics of the rat bladder, there are still gaps in this area of research. First, the viscoelastic behavior of the SCI rat bladder has been assessed in the short-term, but changes in viscoelastic behavior in long-term SCI has yet to be determined. Additionally, voiding via manual compression is generally used in post-operative care for SCI rats. Clinically, different voiding techniques (i.e., manual compression, indwelling catheter, clean intermittent catheterization) lead to different outcomes in terms of bladder health and function [159]. It would be beneficial to investigate the effect of different voiding techniques in SCI rats and evaluate how the bladder remodels in response to these different techniques. This would have clinical relevance as it could highlight reasons for differences in outcomes based on voiding technique.

Finally, no study has investigated the role of location-specific behavior or swelling on bladder biomechanics in a pathological condition, such as SCI. A study that investigates location-specific and swelling effects in SCI using a large animal model of SCI is needed.

BIBLIOGRAPHY

BIBLIOGRAPHY

- [1] R. Cortivo, F. Pagano, G. Passerini, G. Abatangelo, I. Castellani, Elastin and Collagen in the Normal and Obstructed Urinary Bladder, *Br. J. Urol.* 53 (1981) 134–137.
<https://doi.org/10.1111/j.1464-410X.1981.tb03151.x>.
- [2] J.G. Susset, D. Servot-Viguiier, F. Lamy, P. Madernas, R. Black, Collagen in 155 human bladders., *Invest. Urol.* 16 (1978) 204–6. <http://www.ncbi.nlm.nih.gov/pubmed/711413>.
- [3] K.F. Swaiman, W.E. Bradley, Quantitation of collagen in the wall of the human urinary bladder., *J. Appl. Physiol.* 22 (1967) 122–124.
<https://doi.org/10.1152/jappl.1967.22.1.122>.
- [4] K.J. Aitken, D.J. Bägli, The bladder extracellular matrix. Part I: Architecture, development and disease, *Nat. Rev. Urol.* 6 (2009) 596–611.
<https://doi.org/10.1038/nrurol.2009.201>.
- [5] J. Jung, H.K. Ahn, Y. Huh, Clinical and Functional Anatomy of the Urethral Sphincter, *Int. Neurourol. J.* 16 (2012) 102. <https://doi.org/10.5213/INJ.2012.16.3.102>.
- [6] S. Roccabianca, T.R. Bush, Understanding the mechanics of the bladder through experiments and theoretical models: Where we started and where we are heading, *Technology.* 04 (2016) 30–41. <https://doi.org/10.1142/s2339547816400082>.
- [7] S. Korossis, F. Bolland, J. Southgate, E. Ingham, J. Fisher, Regional biomechanical and histological characterisation of the passive porcine urinary bladder: Implications for augmentation and tissue engineering strategies, *Biomaterials.* 30 (2009) 266–275.
<https://doi.org/10.1016/J.BIOMATERIALS.2008.09.034>.
- [8] E. Morales-Orcajo, T. Siebert, M. Böl, Location-dependent correlation between tissue structure and the mechanical behaviour of the urinary bladder, *Acta Biomater.* 75 (2018) 263–278. <https://doi.org/10.1016/j.actbio.2018.05.014>.
- [9] F. Cheng, L.A. Birder, F.A. Kullmann, J. Hornsby, P.N. Watton, S. Watkins, M. Thompson, A.M. Robertson, Layer-dependent role of collagen recruitment during loading of the rat bladder wall, *Biomech. Model. Mechanobiol.* 17 (2018) 403–417.
<https://doi.org/10.1007/s10237-017-0968-5>.
- [10] J. Chen, B.A. Drzewiecki, W.D. Merryman, J.C. Pope, Murine bladder wall biomechanics following partial bladder obstruction, *J. Biomech.* 46 (2013) 2752–2755.
<https://doi.org/10.1016/j.jbiomech.2013.07.022>.
- [11] R. van Mastrigt, B.L.R.A. Coolsaet, W.A. van Duyl, Passive properties of the urinary bladder in the collection phase, *Med. Biol. Eng. Comput.* 16 (1978) 471–482.
<https://doi.org/10.1007/BF02457796>.

- [12] A.N. Natali, A.L. Audenino, W. Artibani, C.G. Fontanella, E.L. Carniel, E.M. Zanetti, Bladder tissue biomechanical behavior: Experimental tests and constitutive formulation, *J. Biomech.* 48 (2015) 3088–3096. <https://doi.org/10.1016/j.jbiomech.2015.07.021>.
- [13] T.W. Gilbert, S. Wognum, E.M. Joyce, D.O. Freytes, M.S. Sacks, S.F. Badylak, Collagen fiber alignment and biaxial mechanical behavior of porcine urinary bladder derived extracellular matrix, *Biomaterials.* 29 (2008) 4775–4782. <https://doi.org/10.1016/j.biomaterials.2008.08.022>.
- [14] S. Wognum, D.E. Schmidt, M.S. Sacks, On the Mechanical Role of De Novo Synthesized Elastin in the Urinary Bladder Wall, *J. Biomech. Eng.* 131 (2009) 101018. <https://doi.org/10.1115/1.4000182>.
- [15] A.S. Nagle, A.P. Klausner, J. Varghese, R.J. Bernardo, A.F. Colhoun, R.W. Barbee, L.R. Carucci, J.E. Speich, Quantification of bladder wall biomechanics during urodynamics: A methodologic investigation using ultrasound, *J. Biomech.* 61 (2017) 232–241. <https://doi.org/10.1016/j.jbiomech.2017.07.028>.
- [16] M.S. Jokandan, F. Ajallouelian, M. Edinger, P.R. Stubbe, S. Baldursdottir, I.S. Chronakis, Bladder wall biomechanics: A comprehensive study on fresh porcine urinary bladder, *J. Mech. Behav. Biomed. Mater.* 79 (2018) 92–103. <https://doi.org/10.1016/J.JMBBM.2017.11.034>.
- [17] E.A. Gormley, Urologic complications of the neurogenic bladder, *Urol. Clin. North Am.* 37 (2010) 601–607. <https://doi.org/10.1016/j.ucl.2010.07.002>.
- [18] I. Goldstein, M.B. Siroky, D.S. Sax, R.J. Krane, Neurourologic Abnormalities in Multiple Sclerosis, *J. Urol.* 128 (1982) 541–545. [https://doi.org/10.1016/S0022-5347\(17\)53037-2](https://doi.org/10.1016/S0022-5347(17)53037-2).
- [19] A. Manack, S.P. Motsko, C. Haag-Molkenteller, R.R. Dmochowski, E.L. Goehring, B.-A. Nguyen-Khoa, J.K. Jones, Epidemiology and healthcare utilization of neurogenic bladder patients in a us claims database, *NeuroUrol. Urodyn.* 30 (2011) 395–401. <https://doi.org/10.1002/nau.21003>.
- [20] G. Samson, D.D. Cardenas, Neurogenic Bladder in Spinal Cord Injury, *Phys. Med. Rehabil. Clin. N. Am.* 18 (2007) 255–274. <https://doi.org/10.1016/j.pmr.2007.03.005>.
- [21] J. Nagatomi, D.C. Gloeckner, M.B. Chancellor, W.C. deGroat, M.S. Sacks, Changes in the Biaxial Viscoelastic Response of the Urinary Bladder Following Spinal Cord Injury, *Ann. Biomed. Eng.* 32 (2004) 1409–1419. <https://doi.org/10.1114/B:ABME.0000042228.89106.48>.
- [22] J. Nagatomi, K.K. Toosi, J.S. Grashow, M.B. Chancellor, M.S. Sacks, Quantification of bladder smooth muscle orientation in normal and spinal cord injured rats, *Ann. Biomed. Eng.* 33 (2005) 1078–1089. <https://doi.org/10.1007/s10439-005-5776-x>.
- [23] E.L. Whitcomb, C.W. Nager, Urodynamics : When Is Testing Clinically Useful ?, *Female Patient (Parsippany).* 34 (2009) 43–48.

<https://www.researchgate.net/publication/265067490>.

- [24] J.J. Wyndaele, The normal pattern of perception of bladder filling during cystometry studied in 38 young healthy volunteers, *J. Urol.* 160 (1998) 479–481. [https://doi.org/10.1016/S0022-5347\(01\)62929-X](https://doi.org/10.1016/S0022-5347(01)62929-X).
- [25] B. Klevmark, Natural pressure-volume curves and conventional cystometry, in: *Scand. J. Urol. Nephrol. Suppl.*, Taylor & Francis, 1999: pp. 1–4. <https://doi.org/10.1080/003655999750169358>.
- [26] B. Klevmark, Motility of the Urinary Bladder in Cats during Filling at Physiological Rates: I. Intravesical Pressure Patterns Studied by a New Methods of Cystometry, *Acta Physiol. Scand.* 90 (1974) 565–577. <https://doi.org/10.1111/j.1748-1716.1974.tb05621.x>.
- [27] C.C. Wang, J. Nagatomi, K.K. Toosi, N. Yoshimura, J.H. Hsieh, M.B. Chancellor, M.S. Sacks, Diabetes-induced Alternations in Biomechanical Properties of Urinary Bladder Wall in Rats, *Urology.* 73 (2009) 911–915. <https://doi.org/10.1016/J.UROLOGY.2008.11.026>.
- [28] T. Watanabe, S. Omata, J.Z. Lee, C.E. Constantinou, Comparative analysis of bladder wall compliance based on cystometry and biosensor measurements during the micturition cycle of the rat, *Neurourol. Urodyn.* 16 (1997) 567–581. [https://doi.org/10.1002/\(SICI\)1520-6777\(1997\)16:6<567::AID-NAU7>3.0.CO;2-C](https://doi.org/10.1002/(SICI)1520-6777(1997)16:6<567::AID-NAU7>3.0.CO;2-C).
- [29] A.E. Finkbeiner, P.D. O'Donnell, Responses of detrusor smooth muscle to stretch and relaxation: In vitro study, *Urology.* 36 (1990) 193–198. [https://doi.org/10.1016/0090-4295\(90\)80228-F](https://doi.org/10.1016/0090-4295(90)80228-F).
- [30] D.C. Gloeckner, M.S. Sacks, M.O. Fraser, G.T. Somogyi, W.C. de Groat, M.B. Chancellor, Passive Biaxial Mechanical Properties of the Rat Bladder Wall After Spinal Cord Injury, *J. Urol.* 167 (2002) 2247–2252. [https://doi.org/10.1016/S0022-5347\(05\)65137-3](https://doi.org/10.1016/S0022-5347(05)65137-3).
- [31] K.K. Toosi, J. Nagatomi, M.B. Chancellor, M.S. Sacks, The Effects of Long-Term Spinal Cord Injury on Mechanical Properties of the Rat Urinary Bladder, *Ann. Biomed. Eng.* 36 (2008) 1470–1480. <https://doi.org/10.1007/s10439-008-9525-9>.
- [32] A. Parekh, A.D. Cigan, S. Wognum, R.L. Heise, M.B. Chancellor, M.S. Sacks, Ex vivo deformations of the urinary bladder wall during whole bladder filling: Contributions of extracellular matrix and smooth muscle, *J. Biomech.* 43 (2010) 1708–1716. <https://doi.org/10.1016/j.jbiomech.2010.02.034>.
- [33] B. Eika, R.M. Levin, P.A. Longhurst, Collagen and bladder function in streptozotocin-diabetic rats: Effects of insulin and aminoguanidine, *J. Urol.* 148 (1992) 167–172. [https://doi.org/10.1016/S0022-5347\(17\)36546-1](https://doi.org/10.1016/S0022-5347(17)36546-1).
- [34] A. Mattiasson, K.E. Andersson, C. Sjogren, Supersensitivity to carbachol in the parasympathetically decentralized feline urinary bladder, *J. Urol.* 131 (1984) 562–565.

[https://doi.org/10.1016/S0022-5347\(17\)50504-2](https://doi.org/10.1016/S0022-5347(17)50504-2).

- [35] G.M. Ghoniem, C.H. Regnier, P. Biancani, L. Johnson, J.G. Susset, Effect of vesical outlet obstruction on detrusor contractility and passive properties in rabbits, *J. Urol.* 135 (1986) 1284–1289. [https://doi.org/10.1016/S0022-5347\(17\)46075-7](https://doi.org/10.1016/S0022-5347(17)46075-7).
- [36] R. M. Levin, Patrick Horan, Shih-Ping, Metabolic Aspects of Urinary Bladder Filling, *Scand. J. Urol. Nephrol.* 33 (1999) 59–66. <https://doi.org/10.1080/003655999750042169>.
- [37] S.C. Barnes, D.E.T. Shepherd, D.M. Espino, R.T. Bryan, Frequency dependent viscoelastic properties of porcine bladder, *J. Mech. Behav. Biomed. Mater.* 42 (2015) 168–176. <https://doi.org/10.1016/j.jmbbm.2014.11.017>.
- [38] L. Baskin, D. Meaney, A. Landsman, S.A. Zderic, E. Macarak, Bovine bladder compliance increases with normal fetal development, in: *J. Urol.*, 1994: pp. 692–695. [https://doi.org/10.1016/s0022-5347\(17\)32682-4](https://doi.org/10.1016/s0022-5347(17)32682-4).
- [39] G.E. Dean, R.S. Cargill, E. Macarak, H.M. Snyder, J.W. Duckett, R. Levin, Active and passive compliance of the fetal bovine bladder, *J. Urol.* 158 (1997) 1094–1099. [https://doi.org/10.1016/S0022-5347\(01\)64396-9](https://doi.org/10.1016/S0022-5347(01)64396-9).
- [40] D.J. Griffiths, R. van Mastrigt, W.A. van Duyl, B.L.R.A. Coolsaet, Active mechanical properties of the smooth muscle of the urinary bladder, *Med. Biol. Eng. Comput.* 17 (1979) 281–290. <https://doi.org/10.1007/BF02443812>.
- [41] D.E. Coplen, E.J. Macarak, R.M. Levin, Developmental Changes in Normal Fetal Bovine Whole Bladder Physiology, *J. Urol.* 151 (1994) 1391–1395. [https://doi.org/10.1016/S0022-5347\(17\)35266-7](https://doi.org/10.1016/S0022-5347(17)35266-7).
- [42] D.O. Freytes, R.S. Tullius, S.F. Badylak, Effect of storage upon material properties of lyophilized porcine extracellular matrix derived from the urinary bladder, *J. Biomed. Mater. Res. Part B Appl. Biomater.* 78B (2006) 327–333. <https://doi.org/10.1002/jbm.b.30491>.
- [43] D.O. Freytes, R.S. Tullius, J.E. Valentin, A.M. Stewart-Akers, S.F. Badylak, Hydrated versus lyophilized forms of porcine extracellular matrix derived from the urinary bladder, *J. Biomed. Mater. Res. Part A.* 87A (2008) 862–872. <https://doi.org/10.1002/jbm.a.31821>.
- [44] D.O. Freytes, R.M. Stoner, S.F. Badylak, Uniaxial and biaxial properties of terminally sterilized porcine urinary bladder matrix scaffolds, *J. Biomed. Mater. Res. Part B Appl. Biomater.* 84B (2008) 408–414. <https://doi.org/10.1002/jbm.b.30885>.
- [45] D.J. Rosario, G.C. Reilly, E.A. Salah, M. Glover, A.J. Bullock, S. MacNeil, Decellularization and sterilization of porcine urinary bladder matrix for tissue engineering in the lower urinary tract, *Regen. Med.* 3 (2008) 145–156. <https://doi.org/10.2217/17460751.3.2.145>.
- [46] F. Bolland, S. Korossis, S.-P. Wilshaw, E. Ingham, J. Fisher, J.N. Kearney, J. Southgate,

- Development and characterisation of a full-thickness acellular porcine bladder matrix for tissue engineering, *Biomaterials*. 28 (2007) 1061–1070.
<https://doi.org/10.1016/J.BIOMATERIALS.2006.10.005>.
- [47] W.A. Farhat, J. Chen, J. Haig, R. Antoon, J. Litman, C. Sherman, K. Derwin, H. Yeger, Porcine bladder acellular matrix (ACM): protein expression, mechanical properties, *Biomed. Mater.* 3 (2008) 025015. <https://doi.org/10.1088/1748-6041/3/2/025015>.
- [48] S.E. Dahms, H.J. Piechota, R. Dahiya, T.F. Lue, E.A. Tanagho, Composition and biomechanical properties of the bladder acellular matrix graft: Comparative analysis in rat, pig and human, *Br. J. Urol.* 82 (1998) 411–419. <https://doi.org/10.1046/j.1464-410X.1998.00748.x>.
- [49] L. Liu, D. Li, Y. Wang, H. Xu, L. Ge, Z. Liang, Evaluation of the biocompatibility and mechanical properties of xenogeneic (porcine) extracellular matrix (ECM) scaffold for pelvic reconstruction, *Int. Urogynecol. J.* 22 (2011) 221–227.
<https://doi.org/10.1007/s00192-010-1288-9>.
- [50] A.L. Brown, W. Farhat, P.A. Merguerian, G.J. Wilson, A.E. Houry, K.A. Woodhouse, 22 week assessment of bladder acellular matrix as a bladder augmentation material in a porcine model, *Biomaterials*. 23 (2002) 2179–2190. [https://doi.org/10.1016/S0142-9612\(01\)00350-7](https://doi.org/10.1016/S0142-9612(01)00350-7).
- [51] F. Oberpenning, J. Meng, J.J. Yoo, A. Atala, De novo reconstitution of a functional mammalian urinary bladder by tissue engineering, *Nat. Biotechnol.* 17 (1999) 149–155.
<https://doi.org/10.1038/6146>.
- [52] C. Rubod, M. Brieu, M. Cosson, G. Rivaux, J.C. Clay, L. De Landsheere, B. Gabriel, Biomechanical properties of human pelvic organs, *Urology*. 79 (2012) 968.e17-968.e22.
<https://doi.org/10.1016/j.urology.2011.11.010>.
- [53] P. Chantereau, M. Brieu, M. Kammal, J. Farthmann, B. Gabriel, M. Cosson, Mechanical properties of pelvic soft tissue of young women and impact of aging, *Int. Urogynecol. J.* 25 (2014) 1547–1553. <https://doi.org/10.1007/s00192-014-2439-1>.
- [54] D.H. Ewalt, P.S. Howard, B. Blyth, H.M. Snyder, J.W. Duckett, R.M. Levin, E.J. Macarak, Is lamina propria matrix responsible for normal bladder compliance?, in: *J. Urol.*, 1992: pp. 544–549. [https://doi.org/10.1016/s0022-5347\(17\)36650-8](https://doi.org/10.1016/s0022-5347(17)36650-8).
- [55] P.A.L.S. Martins, A.L.S. Filho, A.M.R.M.I. Fonseca, A. Santos, L. Santos, T. Mascarenhas, R.M.N. Jorge, A.J.M. Ferreira, Uniaxial mechanical behavior of the human female bladder, *Int. Urogynecol. J.* 22 (2011) 991–995. <https://doi.org/10.1007/s00192-011-1409-0>.
- [56] B.L.R.A. Coolsaet, W.A. van Duyl, R. van Mastrigt, A. van der Zwart, Visco-Elastic Properties of the Bladder Wall, *Urol. Int.* 30 (1975) 16–26.
<https://doi.org/10.1159/000279953>.

- [57] J.G. Venegas, Viscoelastic properties of the contracting detrusor. I. Theoretical basis., *Am. J. Physiol.* 261 (1991) C355-63. <https://doi.org/10.1152/ajpcell.1991.261.2.C355>.
- [58] J.G. Venegas, J.P. Woll, S.B. Woolfson, E.G. Cravalho, N. Resnick, S. V. Yalla, Viscoelastic properties of the contracting detrusor. II. Experimental approach, <https://doi.org/10.1152/Ajpcell.1991.261.2.C364>. (1991).
<https://doi.org/10.1152/AJPCELL.1991.261.2.C364>.
- [59] J.J. Glerum, R. Van Mastrigt, A.J. Van Koevinge, Mechanical properties of mammalian single smooth muscle cells III. Passive properties of pig detrusor and human a terme uterus cells, *J. Muscle Res. Cell Motil.* 11 (1990) 453–462.
<https://doi.org/10.1007/BF01739765>.
- [60] R. van Mastrigt, J.C. Nagtegaal, Dependence of the viscoelastic response of the urinary bladder wall on strain rate, *Med. Biol. Eng. Comput.* 19 (1981) 291–296.
<https://doi.org/10.1007/BF02442547>.
- [61] R.S. Alexander, Viscoplasticity of smooth muscle of urinary bladder., *Am. J. Physiol.* 224 (1973) 618–22. <https://doi.org/10.1152/ajplegacy.1973.224.3.618>.
- [62] J. Nagatomi, K.K. Toosi, M.B. Chancellor, M.S. Sacks, Contribution of the extracellular matrix to the viscoelastic behavior of the urinary bladder wall, *Biomech. Model. Mechanobiol.* 7 (2008) 395–404. <https://doi.org/10.1007/s10237-007-0095-9>.
- [63] A. Kondo, J.G. Susset, Physical properties of the urinary detrusor muscle: A mechanical model based upon the analysis of stress relaxation curve, *J. Biomech.* 6 (1973) 141–151. [https://doi.org/10.1016/0021-9290\(73\)90083-3](https://doi.org/10.1016/0021-9290(73)90083-3).
- [64] B.L.R.A. Coolsaet, W.A. Van Duyl, R. Van Mastrigt, A. Van der Zwart, Step-wise cystometry of urinary bladder New dynamic procedure to investigate viscoelastic behavior, *Urology.* 2 (1973) 255–257. [https://doi.org/10.1016/0090-4295\(73\)90459-7](https://doi.org/10.1016/0090-4295(73)90459-7).
- [65] R.S. Alexander, Mechanical properties of urinary bladder., *Am. J. Physiol.* 220 (1971) 1413–21. <https://doi.org/10.1152/ajplegacy.1971.220.5.1413>.
- [66] J.G. Susset, C.H. Regnier, Viscoelastic properties of bladder strips: standardization of a technique., *Invest. Urol.* 18 (1981) 445–50.
<http://www.ncbi.nlm.nih.gov/pubmed/7228578>.
- [67] W.A. van Duyl, A model for both the passive and active properties of urinary bladder tissue related to bladder function, *Neurourol. Urodyn.* 4 (1985) 275–283.
<https://doi.org/10.1002/nau.1930040404>.
- [68] R. Van Mastrigt, B.L. Coolsaet, W.A. Van Duyl, First results of stepwise straining of the human urinary bladder and human bladder strips., *Invest. Urol.* 19 (1981) 58–61.
<http://www.ncbi.nlm.nih.gov/pubmed/7251329>.
- [69] R. van Mastrigt, D.J. Griffiths, Contractility of the urinary bladder, *Urol. Int.* 34 (1979)

- 410–420. <https://doi.org/10.1159/000280288>.
- [70] R. Van Mastrigt, Mechanical properties of (urinary bladder) smooth muscle, *J. Muscle Res. Cell Motil.* 23 (2002) 53–57. <https://doi.org/10.1023/A:1019936831366>.
- [71] C.H. Regnier, H. Kolsky, P.D. Richardson, G.M. Ghoniem, J.G. Susset, The elastic behavior of the urinary bladder for large deformations, *J. Biomech.* 16 (1983) 915–922. [https://doi.org/10.1016/0021-9290\(83\)90055-6](https://doi.org/10.1016/0021-9290(83)90055-6).
- [72] M.S. Damaser, S.L. Lehman, Two mathematical models explain the variation in cystometrograms of obstructed urinary bladders, *J. Biomech.* 29 (1996) 1615–1619. [https://doi.org/10.1016/S0021-9290\(96\)80013-3](https://doi.org/10.1016/S0021-9290(96)80013-3).
- [73] H. Watanabe, Ki. Akiyama, T. Saito, F. Oki, A finite deformation theory of intravesical pressure and mural stress of the urinary bladder., *Tohoku J. Exp. Med.* 135 (1981) 301–307. <https://doi.org/10.1620/tjem.135.301>.
- [74] F.G. Habteyes, S.O. Komari, A.S. Nagle, A.P. Klausner, R.L. Heise, P.H. Ratz, J.E. Speich, Modeling the influence of acute changes in bladder elasticity on pressure and wall tension during filling, *J. Mech. Behav. Biomed. Mater.* 71 (2017) 192–200. <https://doi.org/10.1016/j.jmbbm.2017.02.020>.
- [75] I. Korkmaz, B. Rogg, A simple fluid-mechanical model for the prediction of the stress-strain relation of the male urinary bladder, *J. Biomech.* (2007). <https://doi.org/10.1016/j.jbiomech.2006.02.014>.
- [76] M.S. Damaser, S.L. Lehman, The effect of urinary bladder shape on its mechanics during filling, *J. Biomech.* 28 (1995). [https://doi.org/10.1016/0021-9290\(94\)00169-5](https://doi.org/10.1016/0021-9290(94)00169-5).
- [77] B.J. Rigby, N. Hirai, J.D. Spikes, H. Eyring, The mechanical properties of rat tail tendon, *J. Gen. Physiol.* 43 (1959) 265–283. <https://doi.org/10.1085/jgp.43.2.265>.
- [78] A. Viidik, R. Ekholm, Light and electron microscopic studies of collagen fibers under strain, *Z. Anat. Entwicklungsgesch.* 127 (1968) 154–164. <https://doi.org/10.1007/BF00521981>.
- [79] A. Viidik, Simultaneous mechanical and light microscopic studies of collagen fibers, *Z. Anat. Entwicklungsgesch.* 136 (1972) 204–212. <https://doi.org/10.1007/BF00519178>.
- [80] I.A. Brown, A scanning electron microscope study of the effects of uniaxial tension on human skin, *Br. J. Dermatol.* 89 (1973) 383–393. <https://doi.org/10.1111/j.1365-2133.1973.tb02993.x>.
- [81] J. Vesely, L. Horny, H. Chlup, R. Zitny, Collagen Orientation and Waviness within the Vein Wall, *Comput Plast Xi Fundam Appl.* (2011) 720–728.
- [82] H. Chen, Y. Liu, M.N. Slipchenko, X. Zhao, J.-X. Cheng, G.S. Kassab, The Layered Structure of Coronary Adventitia under Mechanical Load, *Biophys. J.* 101 (2011) 2555–

2562. <https://doi.org/10.1016/J.BPJ.2011.10.043>.
- [83] S. Roy, C. Boss, R. Rezakhaniha, N. Stergiopoulos, Experimental characterization of the distribution of collagen fiber recruitment, *J. Biorheol.* 24 (2010) 84–93. <https://doi.org/10.1007/s12573-011-0027-2>.
- [84] R. Rezakhaniha, A. Agianniotis, J.T.C. Schrauwen, A. Griffa, D. Sage, C.V.C. Bouten, F.N. van de Vosse, M. Unser, N. Stergiopoulos, Experimental investigation of collagen waviness and orientation in the arterial adventitia using confocal laser scanning microscopy, *Biomech. Model. Mechanobiol.* 11 (2012) 461–473. <https://doi.org/10.1007/s10237-011-0325-z>.
- [85] S. Zeinali-Davarani, M.-J. Chow, R. Turcotte, Y. Zhang, Characterization of Biaxial Mechanical Behavior of Porcine Aorta under Gradual Elastin Degradation, *Ann. Biomed. Eng.* 41 (2013) 1528–1538. <https://doi.org/10.1007/s10439-012-0733-y>.
- [86] S.L. Chang, P.S. Howard, H.P. Koo, E.J. Macarak, Role of type III collagen in bladder filling, *Neurourol. Urodyn.* 17 (1998) 135–145. [https://doi.org/10.1002/\(SICI\)1520-6777\(1998\)17:2<135::AID-NAU7>3.0.CO;2-E](https://doi.org/10.1002/(SICI)1520-6777(1998)17:2<135::AID-NAU7>3.0.CO;2-E).
- [87] Y. Lanir, A structural theory for the homogeneous biaxial stress-strain relationships in flat collagenous tissues, *J. Biomech.* 12 (1979) 423–436. [https://doi.org/10.1016/0021-9290\(79\)90027-7](https://doi.org/10.1016/0021-9290(79)90027-7).
- [88] Y. Lanir, Constitutive equations for fibrous connective tissues, *J. Biomech.* 16 (1983) 1–12. [https://doi.org/10.1016/0021-9290\(83\)90041-6](https://doi.org/10.1016/0021-9290(83)90041-6).
- [89] Y. Lanir, Mechanistic micro-structural theory of soft tissues growth and remodeling: tissues with unidirectional fibers, *Biomech. Model. Mechanobiol.* 14 (2015) 245–266. <https://doi.org/10.1007/s10237-014-0600-x>.
- [90] M.A. Zulliger, P. Fridez, K. Hayashi, N. Stergiopoulos, A strain energy function for arteries accounting for wall composition and structure, *J. Biomech.* 37 (2004) 989–1000. <https://doi.org/10.1016/j.jbiomech.2003.11.026>.
- [91] M.R. Hill, X. Duan, G.A. Gibson, S. Watkins, A.M. Robertson, A theoretical and non-destructive experimental approach for direct inclusion of measured collagen orientation and recruitment into mechanical models of the artery wall, *J. Biomech.* 45 (2012) 762–771. <https://doi.org/10.1016/J.JBIOMECH.2011.11.016>.
- [92] O. Lokshin, Y. Lanir, Micro and macro rheology of planar tissues, *Biomaterials.* 30 (2009) 3118–3127. <https://doi.org/10.1016/J.BIOMATERIALS.2009.02.039>.
- [93] A. Sverdlik, Y. Lanir, Time-Dependent Mechanical Behavior of Sheep Digital Tendons, Including the Effects of Preconditioning, *J. Biomech. Eng.* 124 (2002) 78–84. <https://doi.org/10.1115/1.1427699>.
- [94] E. Raz, Y. Lanir, Recruitment Viscoelasticity of the Tendon, *J. Biomech. Eng.* 131 (2009)

111008. <https://doi.org/10.1115/1.3212107>.
- [95] T.G. Tuttle, D. Morhardt, A. Poli, J. Park, E. Arruda, S. Roccabianca, Investigation of fiber-driven mechanical behavior of human and porcine bladder tissue tested under identical conditions, *J. Biomech. Eng.* (2021).
- [96] N. Johal, D.N. Wood, A.S. Wagg, P. Cuckow, C.H. Fry, Functional properties and connective tissue content of pediatric human detrusor muscle, *Am. J. Physiol. Physiol.* 307 (2014) F1072–F1079. <https://doi.org/10.1152/ajprenal.00380.2014>.
- [97] R.N. Miftahof, H.G. Nam, *Biomechanics of the human urinary bladder*, Springer-Verlag Berlin Heidelberg, 2013. <https://doi.org/10.1007/978-3-642-36146-3>.
- [98] A.J. Schriefl, T. Schmidt, D. Balzani, G. Sommer, G.A. Holzapfel, Selective enzymatic removal of elastin and collagen from human abdominal aortas: Uniaxial mechanical response and constitutive modeling, *Acta Biomater.* 17 (2015) 125–136. <https://doi.org/10.1016/j.actbio.2015.01.003>.
- [99] J.F. Kachur, J.S. Peterson, J.P. Carter, W.J. Rzeszotarski, R.C. Hanson, L. Noronha-Blob, R and S enantiomers of oxybutynin: pharmacological effects in guinea pig bladder and intestine., *J. Pharmacol. Exp. Ther.* 247 (1988).
- [100] O. Ukimura, Effects of Intravesically Administered Anticholinergics, β -Adrenergic Stimulant and α -Adrenergic Blocker on Bladder Function in Unanesthetized Rats, *Tohoku J. Exp. Med.* 170 (1993) 251–260. <https://doi.org/10.1620/tjem.170.251>.
- [101] M.S. Sacks, Incorporation of experimentally-derived fiber orientation into a structural constitutive model for planar collagenous tissues, *J. Biomech. Eng.* 125 (2003) 280–287. <https://doi.org/10.1115/1.1544508>.
- [102] F.H. Silver, D.L. Christiansen, P.B. Snowhill, Y. Chen, Transition from viscous to elastic-based dependency of mechanical properties of self-assembled type I collagen fibers, *J. Appl. Polym. Sci.* 79 (2001) 134–142. [https://doi.org/10.1002/1097-4628\(20010103\)79:1<134::AID-APP160>3.0.CO;2-E](https://doi.org/10.1002/1097-4628(20010103)79:1<134::AID-APP160>3.0.CO;2-E).
- [103] F.H. Silver, J.W. Freeman, G.P. Seehra, Collagen self-assembly and the development of tendon mechanical properties, *J. Biomech.* 36 (2003) 1529–1553. [https://doi.org/10.1016/S0021-9290\(03\)00135-0](https://doi.org/10.1016/S0021-9290(03)00135-0).
- [104] S. Roccabianca, C.A. Figueroa, G. Tellides, J.D. Humphrey, Quantification of regional differences in aortic stiffness in the aging human, *J. Mech. Behav. Biomed. Mater.* 29 (2014) 618–634. <https://doi.org/10.1016/J.JMBBM.2013.01.026>.
- [105] X.Q. Peng, Z.Y. Guo, B. Moran, An anisotropic hyperelastic constitutive model with fiber-matrix shear interaction for the human annulus fibrosus, in: *J. Appl. Mech. Trans. ASME, American Society of Mechanical Engineers Digital Collection*, 2006: pp. 815–824. <https://doi.org/10.1115/1.2069987>.

- [106] W. Wan, H. Yanagisawa, R.L. Gleason, Biomechanical and microstructural properties of common carotid arteries from fibulin-5 null mice, *Ann. Biomed. Eng.* 38 (2010) 3605–3617. <https://doi.org/10.1007/s10439-010-0114-3>.
- [107] J. Ferruzzi, M.J. Collins, A.T. Yeh, J.D. Humphrey, Mechanical assessment of elastin integrity in fibrillin-1-deficient carotid arteries: implications for Marfan syndrome, *Cardiovasc. Res.* 92 (2011) 287–295. <https://doi.org/10.1093/cvr/cvr195>.
- [108] C. Bellini, J. Ferruzzi, S. Roccabianca, E.S. Di Martino, J.D. Humphrey, A microstructurally motivated model of arterial wall mechanics with mechanobiological implications, *Ann. Biomed. Eng.* 42 (2014) 488–502. <https://doi.org/10.1007/s10439-013-0928-x>.
- [109] M.S. Sacks, Biaxial mechanical evaluation of planar biological materials, *J. Elast.* 61 (2000) 199–246. <https://doi.org/10.1023/A:1010917028671>.
- [110] S. Affas, F.-M. Schäfer, K. Algarrahi, V. Cristofaro, M.P. Sullivan, X. Yang, K. Costa, B. Sack, M. Gharaee-Kermani, J.A. Macoska, G. Gundogdu, C. Seager, C.R. Estrada, J.R. Mauney, Augmentation Cystoplasty of Diseased Porcine Bladders with Bi-Layer Silk Fibroin Grafts, *Tissue Eng. Part A.* 25 (2019) 855–866. <https://doi.org/10.1089/ten.tea.2018.0113>.
- [111] B. Yang, Y. Zhang, L. Zhou, Z. Sun, J. Zheng, Y. Chen, Y. Dai, Development of a porcine bladder acellular matrix with well-preserved extracellular bioactive factors for tissue engineering, *Tissue Eng. - Part C Methods.* 16 (2010) 1201–1211. <https://doi.org/10.1089/ten.tec.2009.0311>.
- [112] T.G. Tuttle, S. Roccabianca, Effects of Swelling and Anatomical Location on The Viscoelastic Behavior of The Porcine Urinary Bladder Wall, *J. Biomed. Mater. Res. Part A.* (2021).
- [113] P. Geppetti, R. Nassini, S. Materazzi, S. Benemei, The concept of neurogenic inflammation, *BJU Int. Suppl.* 101 (2008) 2–6. <https://doi.org/10.1111/j.1464-410X.2008.07493.x>.
- [114] M.C. Dupont, J.M. Spitsbergen, K.B. Kim, J.B. Tuttle, W.D. Steers, Histological and neurotrophic changes triggered by varying models of bladder inflammation, *J. Urol.* 166 (2001) 1111–1118. [https://doi.org/10.1016/S0022-5347\(05\)65931-9](https://doi.org/10.1016/S0022-5347(05)65931-9).
- [115] F.M. Hughes, S.J. Sexton, H. Jin, V. Govada, J.T. Purves, Bladder fibrosis during outlet obstruction is triggered through the NLRP3 inflammasome and the production of IL-1 β , *Am. J. Physiol. Physiol.* 313 (2017) F603–F610. <https://doi.org/10.1152/ajprenal.00128.2017>.
- [116] N. Nagy, A. De La Zerda, G. Kaber, P.Y. Johnson, K.H. Hu, M.J. Kratochvil, K. Yadava, W. Zhao, Y. Cui, G. Navarro, J.P. Annes, T.N. Wight, S.C. Heilshorn, P.L. Bollyky, M.J. Butte, Hyaluronan content governs tissue stiffness in pancreatic islet inflammation, *J. Biol. Chem.* 293 (2018) 567–578. <https://doi.org/10.1074/jbc.RA117.000148>.

- [117] G.C. Meléndez, J.L. McLarty, S.P. Levick, Y. Du, J.S. Janicki, G.L. Brower, Interleukin 6 mediates myocardial fibrosis, concentric hypertrophy, and diastolic dysfunction in rats, *Hypertension*. 56 (2010) 225–231. <https://doi.org/10.1161/HYPERTENSIONAHA.109.148635>.
- [118] J.M. Millward, J. Guo, D. Berndt, J. Braun, I. Sack, C. Infante-Duarte, Tissue structure and inflammatory processes shape viscoelastic properties of the mouse brain, *NMR Biomed*. 28 (2015) 831–839. <https://doi.org/10.1002/nbm.3319>.
- [119] Q.T. Nguyen, T.D. Jacobsen, N.O. Chahine, Effects of Inflammation on Multiscale Biomechanical Properties of Cartilaginous Cells and Tissues, *ACS Biomater. Sci. Eng.* 3 (2017) 2644–2656. <https://doi.org/10.1021/acsbiomaterials.6b00671>.
- [120] N. Alkhouli, J. Mansfield, E. Green, J. Bel, B. Knight, N. Liversedge, J.C. Tham, R. Welbourn, A.C. Shore, K. Kos, C.P. Winlove, The mechanical properties of human adipose tissues and their relationships to the structure and composition of the extracellular matrix, *Am. J. Physiol. - Endocrinol. Metab.* 305 (2013) 1427–1435. <https://doi.org/10.1152/ajpendo.00111.2013>.
- [121] S.E. Bezci, A. Nandy, G.D. O’Connell, Effect of Hydration on Healthy Intervertebral Disk Mechanical Stiffness, *J. Biomech. Eng.* 137 (2015) 101007. <https://doi.org/10.1115/1.4031416>.
- [122] D. Shahmirzadi, H.A. Bruck, A.H. Hsieh, Measurement of Mechanical Properties of Soft Tissues In Vitro Under Controlled Tissue Hydration, *Exp. Mech.* 53 (2013) 405–414. <https://doi.org/10.1007/s11340-012-9644-y>.
- [123] M.A. Lillie, J.M. Gosline, The effects of hydration on the dynamic mechanical properties of elastin, *Biopolymers*. 29 (1990) 1147–1160. <https://doi.org/10.1002/bip.360290805>.
- [124] J.M. Gosline, C.J. French, Dynamic mechanical properties of elastin, *Biopolymers*. 18 (1979) 2091–2103. <https://doi.org/10.1002/bip.1979.360180818>.
- [125] K.S. Wu, W.W. Van Osdol, R.H. Dauskardt, Mechanical properties of human stratum corneum: Effects of temperature, hydration, and chemical treatment, *Biomaterials*. 27 (2006) 785–795. <https://doi.org/10.1016/j.biomaterials.2005.06.019>.
- [126] A. Maroudas, I. Ziv, N. Weisman, M. Venn, Studies of hydration and swelling pressure in normal and osteoarthritic cartilage, *Biorheology*. 22 (1985) 159–169. <https://doi.org/10.3233/BIR-1985-22206>.
- [127] S.M. Han, S.Y. Lee, M.H. Cho, J.K. Lee, Disc hydration measured by magnetic resonance imaging in relation to its compressive stiffness in rat models, in: *Proc. Inst. Mech. Eng. Part H J. Eng. Med.*, SAGE PublicationsSage UK: London, England, 2001: pp. 497–502. <https://doi.org/10.1243/0954411011536091>.
- [128] A.M. Taylor, R.H.C. Bonser, J.W. Farrent, The influence of hydration on the tensile and compressive properties of avian keratinous tissues, in: *J. Mater. Sci.*, Springer, 2004: pp.

939–942. <https://doi.org/10.1023/B:JMISC.0000012925.92504.08>.

- [129] F. Dittmann, H. Tzschätzsch, S. Hirsch, E. Barnhill, J. Braun, I. Sack, J. Guo, Tomoelastography of the abdomen: Tissue mechanical properties of the liver, spleen, kidney, and pancreas from single MR elastography scans at different hydration states, *Magn. Reson. Med.* 78 (2017) 976–983. <https://doi.org/10.1002/mrm.26484>.
- [130] T.J. Pence, H. Tsai, Swelling-Induced Cavitation of Elastic Spheres, *Math. Mech. Solids.* 11 (2006) 527–551. <https://doi.org/10.1177/1081286504046481>.
- [131] H. Demirkoparan, T.J. Pence, Swelling of an internally pressurized nonlinearly elastic tube with fiber reinforcing, *Int. J. Solids Struct.* 44 (2007) 4009–4029. <https://doi.org/10.1016/j.ijsolstr.2006.11.006>.
- [132] V. Zamani, T.J. Pence, Swelling, Inflation, and a Swelling-Burst Instability in Hyperelastic Spherical Shells, *Int. J. Solids Struct.* 125 (2017) 134–149. <https://doi.org/10.1016/j.ijsolstr.2017.07.010>.
- [133] S.M. Shirreffs, R.J. Maughan, Urine osmolality and conductivity as indices of hydration status in athletes in the heat, *Med. Sci. Sport. Exerc.* 30 (1998) 1598–1602. <https://doi.org/10.1097/00005768-199811000-00007>.
- [134] S.A. Lewis, Everything you wanted to know about the bladder epithelium but were afraid to ask, *Am. J. Physiol. Physiol.* 278 (2000) F867–F874. <https://doi.org/10.1152/ajprenal.2000.278.6.F867>.
- [135] L.A. Birder, Role of the urothelium in bladder function, in: *Scand. J. Urol. Nephrol. Suppl.*, Lori Birder, 2004: pp. 48–53. <https://doi.org/10.1080/03008880410015165>.
- [136] G. Apodaca, S. Kiss, W. Ruiz, S. Meyers, M. Zeidel, L. Birder, Disruption of bladder epithelium barrier function after spinal cord injury, *Am. J. Physiol. Physiol.* 284 (2003) F966–F976. <https://doi.org/10.1152/ajprenal.00359.2002>.
- [137] S.A. Lewis, J.R. Berg, T.J. Kleine, Modulation of epithelial permeability by extracellular macromolecules, *Physiol. Rev.* 75 (1995) 561–589. <https://doi.org/10.1152/physrev.1995.75.3.561>.
- [138] J.B. Wade, J.P. Revel, V.A. DiScala, Effect of osmotic gradients on intercellular junctions of the toad bladder., *Am. J. Physiol.* 224 (1973) 407–415. <https://doi.org/10.1152/ajplegacy.1973.224.2.407>.
- [139] D.R. DiBona, M.M. Civan, Pathways for movement of ions and water across toad urinary bladder - I. Anatomic site of transepithelial shunt pathways, *J. Membr. Biol.* 12 (1973) 101–128. <https://doi.org/10.1007/BF01869994>.
- [140] S. Roccabianca, G.A. Ateshian, J.D. Humphrey, Biomechanical roles of medial pooling of glycosaminoglycans in thoracic aortic dissection, *Biomech. Model. Mechanobiol.* 13 (2014) 13–25. <https://doi.org/10.1007/s10237-013-0482-3>.

- [141] B.L.R.A. Coolsaet, W.A. Van Duyl, R. Van Mastrigt, J.W. Schouten, Viscoelastic properties of bladder wall strips, *Invest. Urol.* 12 (1975) 351–356. <https://europepmc.org/article/med/1112665>.
- [142] J.G. Venegas, J.P. Woll, S.B. Woolfson, E.G. Cravalho, N. Resnick, S. V. Yalla, Viscoelastic properties of the contracting detrusor II. Experimental approach, *Am. J. Physiol. - Cell Physiol.* 261 (1991). <https://doi.org/10.1152/ajpcell.1991.261.2.c364>.
- [143] J.R. Funk, G.W. Hall, J.R. Crandall, W.D. Pilkey, Linear and quasi-linear viscoelastic characterization of ankle ligaments, *J. Biomech. Eng.* 122 (2000) 15–22. <https://doi.org/10.1115/1.429623>.
- [144] M.P. Ghatas, M.R. Khan, A.S. Gorgey, Skeletal muscle stiffness as measured by magnetic resonance elastography after chronic spinal cord injury: A cross-sectional pilot study, *Neural Regen. Res.* 16 (2021) 2486–2493. <https://doi.org/10.4103/1673-5374.313060>.
- [145] J. Scott, B. Sheridan, R. Andrus, N. Monday, A. Selby, T.R. Bush, Tissue matters: In-vivo tissue properties of persons with spinal cord injuries to inform clinical models for pressure ulcer prevention, *J. Biomech.* 120 (2021) 110389. <https://doi.org/10.1016/j.jbiomech.2021.110389>.
- [146] S. Sangsiri, H. Xu, R. Fernandes, G.D. Fink, H.L. Lujan, S.E. DiCarlo, J.J. Galligan, Spinal cord injury alters purinergic neurotransmission to mesenteric arteries in rats, *Am. J. Physiol. Heart Circ. Physiol.* 318 (2020) H223–H237. <https://doi.org/10.1152/ajpheart.00525.2019>.
- [147] H.C. Ott, T.S. Matthiesen, S.K. Goh, L.D. Black, S.M. Kren, T.I. Netoff, D.A. Taylor, Perfusion-decellularized matrix: Using nature’s platform to engineer a bioartificial heart, *Nat. Med.* 14 (2008) 213–221. <https://doi.org/10.1038/nm1684>.
- [148] E. Meijering, M. Jacob, J.-C.F. Sarria, P. Steiner, H. Hirling, M. Unser, Design and validation of a tool for neurite tracing and analysis in fluorescence microscopy images, *Cytometry.* 58A (2004) 167–176. <https://doi.org/10.1002/cyto.a.20022>.
- [149] R. Avazmohammadi, M.R. Hill, M.A. Simon, W. Zhang, M.S. Sacks, A novel constitutive model for passive right ventricular myocardium: evidence for myofiber–collagen fiber mechanical coupling, *Biomech. Model. Mechanobiol.* 16 (2017) 561–581. <https://doi.org/10.1007/s10237-016-0837-7>.
- [150] H. Demiray, A note on the elasticity of soft biological tissues, *J. Biomech.* 5 (1972) 309–311. [https://doi.org/10.1016/0021-9290\(72\)90047-4](https://doi.org/10.1016/0021-9290(72)90047-4).
- [151] M.R. Grobbel, L.C. Lee, S.W. Watts, G.D. Fink, S. Roccabianca, Left Ventricular Geometry, Tissue Composition, and Residual Stress in High Fat Diet Dahl-Salt Sensitive Rats, *Exp. Mech.* 61 (2021) 191–201. <https://doi.org/10.1007/s11340-020-00664-8>.
- [152] A. Delfino, N. Stergiopoulos, J.E. Moore, J.J. Meister, Residual strain effects on the stress field in a thick wall finite element model of the human carotid bifurcation, *J. Biomech.* 30

- (1997) 777–786. [https://doi.org/10.1016/S0021-9290\(97\)00025-0](https://doi.org/10.1016/S0021-9290(97)00025-0).
- [153] R.H. Hackler, M.K. Hall, T.A. Zampieri, Bladder Hypocompliance in the Spinal Cord Injury Population, *J. Urol.* 141 (1989) 1390–1393. [https://doi.org/10.1016/S0022-5347\(17\)41319-X](https://doi.org/10.1016/S0022-5347(17)41319-X).
- [154] G.C. Mingin, T.J. Heppner, N.R. Tykocki, C.S. Erickson, M.A. Vizzard, M.T. Nelson, Social stress in mice induces urinary bladder overactivity and increases TRPV1 channel-dependent afferent nerve activity, *Am. J. Physiol. - Regul. Integr. Comp. Physiol.* 309 (2015) R629–R638. <https://doi.org/10.1152/ajpregu.00013.2015>.
- [155] A. Atala, Tissue engineering of human bladder, *Br. Med. Bull.* 97 (2011) 81–104. <https://doi.org/10.1093/bmb/ldr003>.
- [156] J.O. Virues Delgado, S. Delorme, R. El-Ayoubi, R. DiRaddo, S.G. Hatzikiriakos, Effect of freezing on the passive mechanical properties of arterial samples, *J. Biomed. Sci. Eng.* 03 (2010) 645–652. <https://doi.org/10.4236/jbise.2010.37088>.
- [157] Y. Lanir, G. Hayam, M. Abovsky, A.Y. Zlotnick, G. Uretzky, E. Nevo, S.A. Ben-Haim, Effect of myocardial swelling on residual strain in the left ventricle of the rat, *Am. J. Physiol. - Hear. Circ. Physiol.* 270 (1996) 736–1743. <https://doi.org/10.1152/ajpheart.1996.270.5.h1736>.
- [158] S.L. Chang, P.S. Howard, H.P. Koo, E.J. Macarak, Role of type III collagen in bladder filling, *Neurourol. Urodyn.* 17 (1998) 135–145. [https://doi.org/10.1002/\(SICI\)1520-6777\(1998\)17:2<135::AID-NAU7>3.0.CO;2-E](https://doi.org/10.1002/(SICI)1520-6777(1998)17:2<135::AID-NAU7>3.0.CO;2-E).
- [159] A.P. Cameron, L.P. Wallner, M.B. Forchheimer, J.Q. Clemens, R.L. Dunn, G. Rodriguez, D. Chen, J. Horton, D.G. Tate, Medical and psychosocial complications associated with method of bladder management after traumatic spinal cord injury, *Arch. Phys. Med. Rehabil.* 92 (2011) 449–456. <https://doi.org/10.1016/j.apmr.2010.06.028>.